CONTENTS

EXPERIMENTAL ANALYSIS OF NAVIGATIONAL PRECISION FOR DEDICATED GNSS RECEIVERS

Maciej SŁOWIK*, Tomasz MROZEK**

*Bialystok University of Technology, Faculty of Mechanical Engineering,
ul. Wiejska 45C, 15-351 Bialystok, Poland
**Institute of Telecommunications, Faculty of Electronics and Information Technology, Warsaw University of Technology,
ul. Nowowiejska 15/19, 00-665 Warszawa, Poland

maciejslowik@gmail.com, t.mrozek.1@stud.elka.pw.edu.pl

Abstract: In the paper experimental investigations related with analysis of navigational precision of three chosen GNSS receivers are shown. Used receivers allow for measurement of navigational signals in following modes of operations: receiving signals from single-frequency GPS system, dual-frequency GPS/GLONASS system, and receiving signals from GPS constellation with use of differential measurements. In the last mode the base station and mobile receiver were configured for transmitting/receiving differential corrections by pair of industry-grade radio modems. The most important features and configuration of navigational receivers for conducted experiment are presented. Afterward the features of computer program designed especially for simultaneous acquisition, analysis of quality parameters and archiving of navigational signals are shown. The results of conducted investigations are also shown. For each of the receivers quantity and quality parameters such as maximum and minimum numbers of visible satellites and DOP (dilution of precision) parameters achieved during the experiment are given.

Key words: GNSS Receivers, DGPS Measurements, GPS, GLONASS

1. INTRODUCTION

Global navigational satellite systems are nowadays used in different domains such as: communication, localization and tracking of vehicles (Cobano et al., 2010), precision agriculture (Perez-Ruiz et al., 2011) and unmanned aerial vehicles (Słowik, Gosiewski 2012). Also every new smartphone is now equipped in GNSS receiver – and their users use locationbased services (http://www.gsa.europa.eu). Accuracy of GNSS systems is also advancing. The receivers have more and more channels, which are used for increased precision of GNSS measurements by augmentations systems such as SBAS and EGNOS, also time of signal reacquisition is reduced. Nevertheless position measurements read by GNSS receivers are always effected by the errors. This is result of e.g. disturbances of navigational signal path (ionospheric, tropospheric, multipath effect) (Deng-feng et al., 2009). One of proposed solution for increasing quality of GNSS readings is to use the differential measurements. It required two GNSS receivers, configured for differential measurements and communication system which allow exchange the navigational corrections between them (Bakuła et al., 2009). Another solution are receivers which can obtain navigational signals from more than one GNSS system e.g. concurrent use of GPS and GLONASS. This approach was presented in the papers of Defraigne (2011), Kuzin (2007) and Kuter (2010).

In the paper the experimental research of three different type GNSS receivers was conducted. The measurements from receivers mentioned below were compared:
a) GPS receiver,
b) GPS mobile receiver and base station – working in differential mode (RTK-20),
c) GPS/GLONASS receiver.

The authors have shown features of used navigational receivers, described computer application created for simultaneous reading, archiving and analyzing of data. Afterward from obtained data, the quality parameters which characterize received navigational signals and results from experiment as imitation of traveled path were shown. Therefore mentioned parameters are PDOP (Position Dilution of Precision) and HDOP (Horizontal Dilution of Precision) (Specht, 2007).

$$PDOP = \frac{1}{\sigma} \sqrt{\sigma_x{}^2 + \sigma_y{}^2 + \sigma_z{}^2} \ , \tag{1}$$

$$HDOP = \frac{1}{\sigma} \sqrt{\sigma_x{}^2 + \sigma_y{}^2} \ , \tag{2}$$

$$VDOP = \frac{1}{\sigma} \sqrt{\sigma_z{}^2} \ , \tag{3}$$

where: σ – error of navigational parameter, σ_x, σ_y, σ_z – mean square errors of computed position in three directions (x, z, y).

2. EXPERIMENT SETUP

In described experiment the research was conducted on Bialystok University of Technology area. During investigations the three receivers were used at the same time, with the same weather conditions and with the same amount of visible satellites of GNSS systems. This solution was determined to reduce impact of signals propagation errors in the path from satellites to receivers, which will be the case if every of the receivers were investigated separately. For this purpose, special hardware configuration and frame for all of the receivers were made. Furthermore the

base station was configured for differential measurements. The dedicated computer application was written which allow reading data frames in NMEA-0183 format simultaneously from three receivers. These application was used for acquisition of data on the mobile computer (through TTL-USB and USB ports).

2.1. Data Acquisition Software

Due to character of investigations – necessity of concurrent analysis of signals derived from three sources of navigational measurements, no commercially available applications which allow for simultaneously connection of three different types of receivers was found. That is a cause for developing of the dedicated computer application, which enable parallel read and processing of navigational data from three different receivers. The aforementioned program was developed in C# and Visual Studio IDE and enable concurrent backup, processing and signal analysis from three investigated GNSS receivers. That allow for recording navigational position and comparison of properties and quality characteristics of receivers in the same time. Beside measurement the application allow for reading and analysis of saved data. The chosen features of the application:

−   concurrent use of three GNSS receivers, with reading and backup of data frames from GNSS receivers in NMEA-0183 format, their processing and saving as text files;
−   NMEA-0183 data frame decomposition – in graphical form (in the form of charts of chosen characterics), and number representation of obtained measurements of geographical longitude and latitude, amount of currently visible satellites, quality parameters as PDOP, HDOP and VDOP;
−   visualization of path travelled with use of OpenStreetMap online service as arbitrary chosen path in the form of finite set of real numbers which are geographical longitude and latitude.
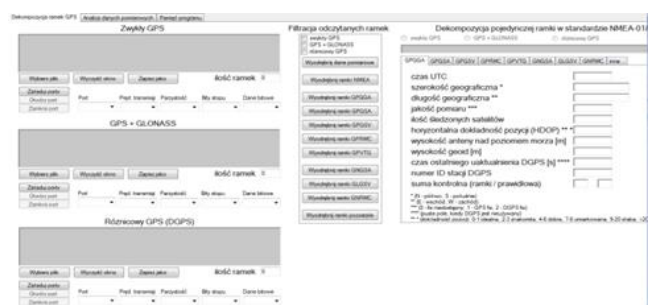

Fig. 1. Control panel of data acquisition and processing application (Mrozek, 2013)

2.2. GNSS Receivers

In the paper three different GNSS receivers were used. All of them was seen as serial devices with different COM numbers, given by operating system.

Main features of GPS Mouse Skytraq SJ-5210 (which contains SiRFStar III chipset) were described in (http://www.skytraq.com). The second receiver shown in Fig. 2. Is described in (https://www.maritex.com.pl). For differential measurements devices described in (http://www.novatel.com), showed below were used:

Fig. 2. On the left GPS Mouse Skytraq SJ-5210, on the right GNSSGMS G9 – picture of the receiver with USB-TTL interface in cover

Fig. 3. On the right - picture of base station Novatel FlexPak G2-V2-L1 with Novatel GPS-701-GG antenna, on the left mobile receiver GNSS Novatel OEMV-1DF mounted on dedicated power board with ANT-35C1GA-TW-N antenna

Receivers described above were connected to mobile computer by USB ports, which enable reading position and others parameters included in data frames of NMEA protocol.

Base station and mobile receiver were configured for receiving differential corrections by radio link (pair of industrial grade radio modems).
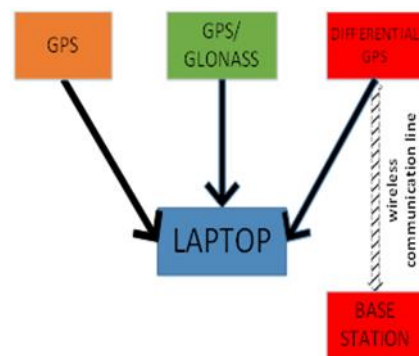
Fig. 4. Diagram of receivers communication during the experiment

3. CONDUCTED EXPERIMENT

As a part of experiment the concurrent reading, processing and saving navigational data from three different GNSS receivers (GPS, GPS+GLONASS and DGPS) during travelling by foot on determined path (Fig. 5). In the point indicated as start and end point of the path (red dot on the blue line near the middle of figure) the DGPS base station with radio modem configured for sending navigational corrections was located. The red arrow denote the direction of movement. The dotted line mean parts of the path in which impact of buildings on quality of measurements were observed. In this places the break of data link with navigational corrections occurred most frequently.

Fig. 5. The path on which the reading, processing and saving of navigational signals from GNSS receivers was made
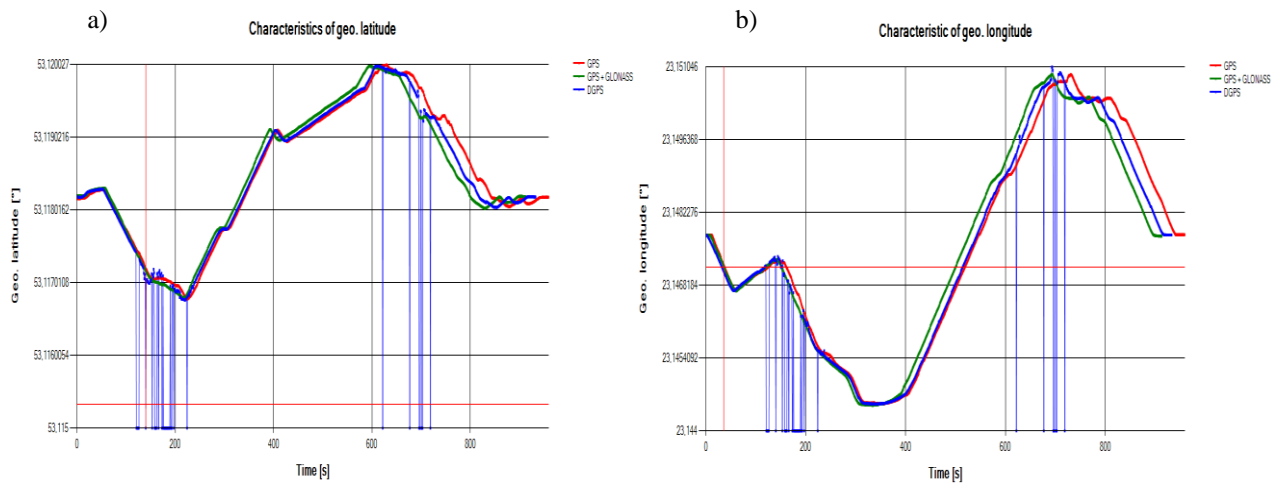
Fig. 6. The characteristic of geographical latitude (a) and longitude (b) changes – vertical lines indicate data frames when the connection between radio modems for DGPS measurements was broken
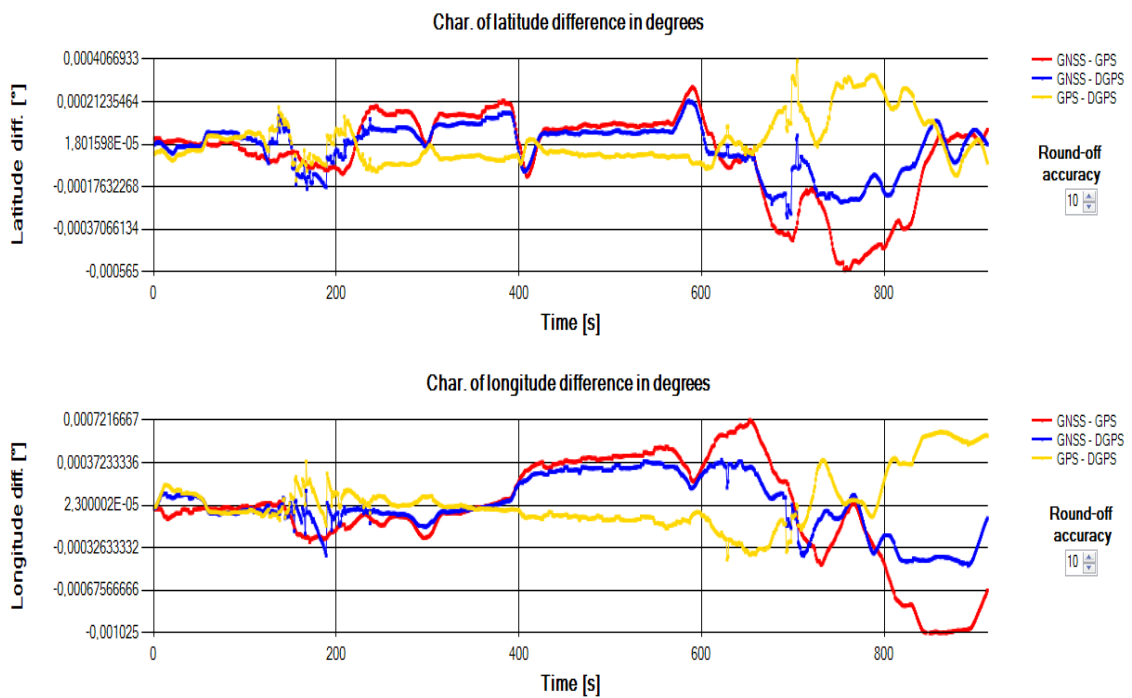
Fig. 7. Characteristic of changes of latitude and longitude in degrees

Maciej Słowik, Tomasz Mrozek
Experimental Analysis of Navigational Precision For Dedicated GNSS Receivers
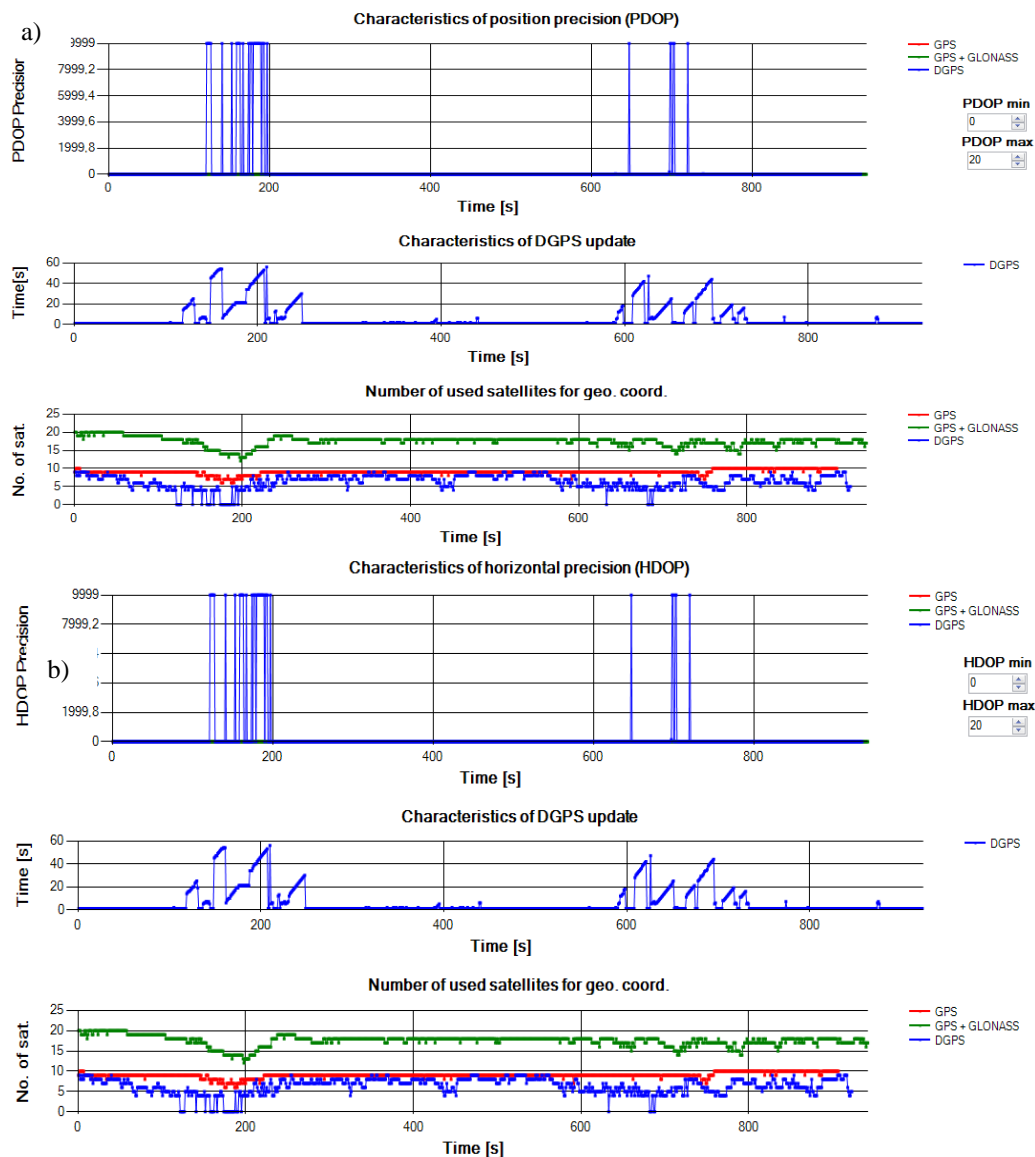
Fig. 8. The PDOP (a) and HDOP (b) characteristic of acquired navigational signals

Fig. 9. Navigational signals received by three GNSS receivers ploted on the experiment map – horizontal lines indicates data frames when communication between radio modems for DGPS measurements was corrupted

4. EXPERIMENT RESULTS

Based on navigational data acquired during the experiment analysis od received signals were made. The most important parameters are described in tables 1-3.

Tab. 1. Number of used satellites

	GPS	GPS+GLONASS	DGPS
min. no of available satellites	6	12	0
max. no of available satellites	10	20	9

In the table above maximum and minimum number of visible satellites are shown. Number 0 for DGPS measurement indicates communication link break between radio modems which were sending navigational corrections from base station to mobile receiver.

Tab. 2. Values of DOP parameters

	GPS	GPS+GLONASS	DGPS
PDOP min	1.7	0.84	1.7
PDOP max	4	1.34	9999
HDOP min	0.9	0.54	0.9
HDOP max	2.1	0.9	9999
VDOP min	1.5	0.64	0
VDOP max	3.3	1.16	121.4

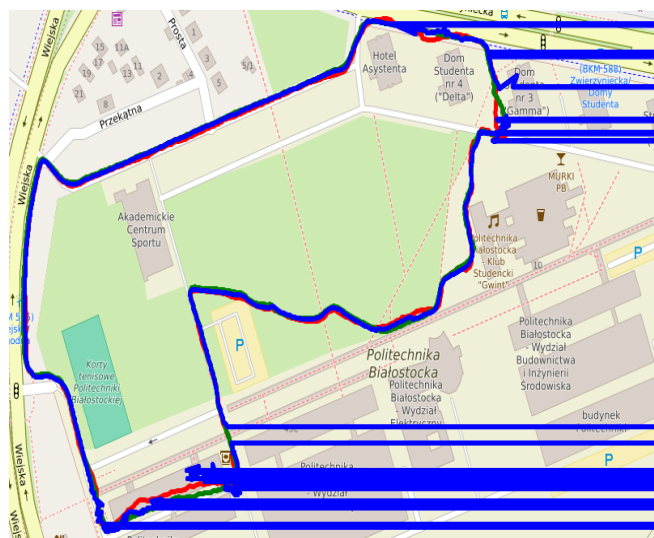Values 9999 and 121.4 from Tab. 2 are unacceptable – they occurred in the moment of communication link break between radio modems of base station and mobile receiver.

Tab. 3. Changes of geographical lattitude and longitude

Changes of geographical latitude			
	GPS	GPS+GLONASS	DGPS
Δx min[°]	-0.000565	-0.0003151317	-0.000147205
Δx max[°]	0.0002783333	0.0002171683	0.0004066933
Changes of geographical longitude			
Δy min[°]	-0.001025	-0.00047172	-0.0004219867
Δy max[°]	0.0007216667	0.00039619	0.0006247

In the Tab. 3 the minimal and maximal scope of changes of geographical latitude and longitude is shown.

5. CONCLUSIONS

In the paper authors prepared and conducted experimental analysis and comparison of work and quality parameters of received navigational data for three different GNSS receivers. For investigations the following devices was chosen: one-frequency GPS, dual frequency GPS+GLONASS and one fre-quency differential GPS. These devices was mounted on dedicated frame for their simultaneous work. Due to lack of available software, the dedicated computer application for acquisition, processing and saving of received data frames was written. The experiment was conducted on Bialystok University of Technology Campus Area, where during the travel by foot the impact of building for quality of measurement was observed. Based on measurement and analysis of quality parameters, the best quality and availability of measurement were provided by dual frequency receiver which use the biggest number of satellites. In the case of DGPS receiver unacceptable values of PDOP and HDOP parameters occurred due to the break of communication link between base station and DGPS mobile receiver connected with entering area with high buildings. These moments were described in table 2 and on Fig. 6 and 9 by vertical and horizontal lines. In future works use of WiFi or circular communication is planned for sending navigational corrections between base station and mobile DGPS receiver.

REFERENCES

1. **Bakuła M., Oszczak, S., Pelc-Mieczkowska, R.** (2009), Performance of RTK Positioning in Forest Conditions: Case Study, *Journal of Surveying Engineering*, 135(3), 125–130.
2. **Cobano J.A., Estremera J., Gonzalez de Santos P.** (2010), Accurate tracking of legged robots on natural terrain, *Autonomous Robots*, 28(2), 231-244.
3. **Defraigne. P, Baire Q.** (2011), Combining GPS and GLONASS for time and frequency transfer, *Advances in Space Research*, 47(2), 265–275.
4. **Deng-Feng R., Yun-Peng L., Zhen-Li M.** (2009), Procedia Earth and Planetary Science, 1(1), 1233–1236.
5. **Kuter N., Kuter S.** (2010), Accuracy comparison between GPS and DGPS: A field study at METU campus, *European Journal of Remote Sensing*, 42, 3-14.
6. **Kuzin S. ,Revnivykh S., Tatevyan S.** (2007), GLONASS as a key element of the Russian Positioning Service, *Advances in Space Research*, 39(10), 1539–1544.
7. **Mrozek T.** (2013), *Object position estimation using mobile satellite of differential navigation methods*, Master's Thesis, Bialystok University of Technology
8. **Perez-Ruiz M., Carballido J., Aguera J., Gil J.A.** (2011), Assessing GNSS correction signals for assisted guidance systems in agricultural vehicles, *Precision Agriculture*, 12(5), 639-652
9. **Słowik M., Gosiewski Z.** (2013), Base Station for Monitoring of Unmanned Aerial Vehicle Flight, *Solid State Phenomena: Mechatronic Systems and Materials IV*, 182-187.
10. **Specht C.** (2007), *GPS System*, Bernadinium, Gdańsk (in Polish).
11. http://www.gsa.europa.eu/system/files/reports/GNSS-Market-Report-2015-issue4_0.pdf (access 12.04.2015)
12. http://www.novatel.com/assets/Documents/Papers/FlexPak-G2.pdf (access 10.05.2015)
13. http://www.novatel.com/assets/Documents/Papers/OEMV-1_Series.pdf (access 10.05.2015)
14. http://www.skytraq.com (access 10.05.2015)
15. https://www.maritex.com.pl/media/uploads/products/wi/GPS-GMS-G9.pdf (access 10.05.2015)

NUMERICAL ANALYSIS OF THE RISK OF NECK INJURIES CAUSED BY IED EXPLOSION UNDER THE VEHICLE IN MILITARY ENVIRONMENTS

Agnieszka MACKIEWICZ*, Grzegorz SŁAWIŃSKI**, Tadeusz NIEZGODA**, Romuald BĘDZIŃSKI*

*Faculty of Mechanical Engineering, Department of Biomedical Engineering, University of Zielona Góra,
ul. Licealna 9, 65-417 Zielona Góra, Poland
**Faculty of Mechanical Engineering, Department of Mechanics and Applied Computer Science, Military University of Technology,
ul. Gen. S. Kaliskiego 2, 00-908 Warszawa, Poland

a.mackiewicz@ibem.uz.zgora.pl, grzegorz.slawinski@wat.edu.pl, tniezgoda@wat.edu.pl, r.bedzinski@ibem.uz.zgora.pl

Abstract: As a result of an explosion under a military vehicle, the risk of threat to life and health of the crew increases. Examination of this event in terms of the security of soldiers comes down to a complex analysis of the mutual interaction of the body of a soldier, seating and structural elements of the vehicle. As a result, shock wave impacts can cause tremor resulting from the construction of the vehicle and acceleration of the passenger's body. This study attempts to analyze the impact of an explosion of an improvised explosive device (IED) under the military vehicle with the risk of cervical spine injuries of soldiers. The analysis was carried out using numerical methods in the LS-DYNA program and was carried out taking into account the variable displacement values and acceleration recorded during the\ explosion. The study used a model of the body of a soldier in the form of a Hybrid III 50th Male Dummy.

Key words: Cervical Spine, Dynamic Overload, Underbody Blast Loadings, Injury Risk Curves, Military Environments

1. INTRODUCTION

Analysis of data from the Military Institute of Medicine base indicates a large percentage of cervical spine injuries occurring in Polish soldiers serving in Afghanistan in the period from June 2010 to April 2014. In 91 incidents, 312 of soldiers were injured (18 dead), of which 69 incidents were caused by an explosion of improvised explosive devices (IEDs). In 44 explosions the shock wave effected soldiers moving in the Rosomak type wheeled Armored Personnel Carriers (APCs). More than one third of all injuries resulted from bruises, twisted, fractures and structural injuries of the spine. Fig. 1 illustrates the incidence of dysfunction at different levels of the spine.
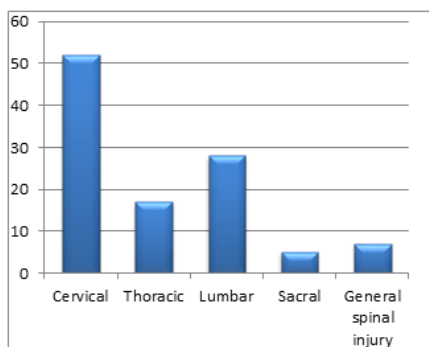

Fig. 1. The proportion of spinal dysfunction (Wojtkowski et al., 2014; Brzozowski et al., 2014)

The largest number of injuries occur in segments of the cervical spine, lumbar and thoracic (Wojtkowski et al., 2014,

Brzozowski et al., 2014). Military vehicles are exposed to the impact of a strong shock wave created by the explosion of explosive devices under the wheels, the hull or the side of the vehicle as well as sudden changes resulting in uncontrolled movement of unsecured items from inside the vehicle (Yang et al., 2013). The authors of various studies indicate that the high amplitude of shock waves caused by an explosion results in the effects of local and global construction of the vehicle. In the initial shock wave phase, acceleration increases until it contacts the bottom of the body followed by a contact, wave reflection and retransfer of the structure of the vehicle, wherein depending on the structure, elastic and plastic deformation is formed. High amplitude and short duration pulse impact acceleration cause the transfer of heavy loads by foot and pelvis to other body parts of soldiers, which takes about 50 milliseconds after detonation. The global effect is related to the energy absorbed by the vehicle emitted by the shock wave. Depending on the weight, the vehicle absorbs some of the energy - between 10 and 20 ms, and the transporter begins to float, reaching a maximum peak height between 100 and 300 ms. The impact of the explosion on the vehicle and the crew is shown in Fig. 2. During this incident the soldiers are mostly at risk of injury (Sławiński et al., 2013, Ramasamy et al., 2011, Heider et al., 2010, Krzystała et al., 2011a). Fig. 3 shows a snapshot of the AMV Rosomak after IED explosion under the hull of the vehicle (Slawinski's own resources, Afghanistan, 2012).

Seat belts are standard equipment of the seats in the AMV Rosomak, but the need for rapid entry and exit from the vehicle during a mission often means that soldiers ignore this protection. The aim of the study was to analyze the impact of the use of seat belts to the risk of cervical spine injuries to the driver and passengers of the military vehicle as a result of an explosion caused by overrunning onto an explosive device.
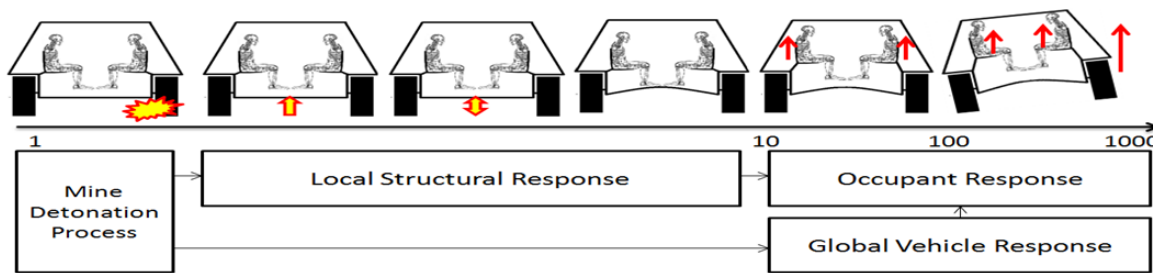
Fig. 2. The sequence of events during the detonation of an IED (Developed in accordance with HFM-090/TG-25, 2007, Krzystała et al., 2011b)

Fig. 3. AMV Rosomak after IED explosion (Slawinski's own resources, Afghanistan, 2012)

2. METHOD

The study attempts to assess the risk of cervical spine injuries of the driver and soldiers in the range of the AMV Rosomak armored amphibious assault vehicle caused by explosive mine under the right front wheel. The study was based on a dynamic numerical analysis in the LS-DYNA program using the explicit integration method to solve fast changing time problems. In the first step of research a simplified geometry of the AMV Rosomak vehicle was prepared (Fig. 4) having the correct distribution of seats, in the range of assault designed for soldiers-passengers (P2, P3, P4, P5) and in the driver's compartment (P1). The geometric model was digitized using four-node solid elements. In order to take into account the weight of the vehicle, a concentrated mass of main components: turret - 2900 kg, drive unit 2200 kg and 8 of the wheels with a suspension of 270 kg per wheel was used in the model (Operating Instructions, description and use Rosomak 2005). The thickness of the painted steel sheet construction increased from 7 to 11mm. In order to obtain realistic weight of the AMV Rosomak of 22000kg, the density of the material was increased. In the model, the mass centre occurs as zero-dimensional single-node elements. Absorption conditions were simulated to support the hull on a system of springs (three per wheel) with non-linear and asymmetrical characteristics.

The input data related to the movement of the vehicle needed to analyze body movements of soldiers in operating conditions were chosen based on the guidelines given by Nilakantan (2009). The output of the simulation obtained an explosion at the right front wheel, registering records of displacement measurement points in the time of 300 ms. Building on a set of data provided by the Nilakantan et al (2009), forcing the vehicle was described as an impulse floor speed - 10.7 m / s. The chart of the command floor speed induced by the explosion of the load is shown in Fig. 5 (Nilakantan et al., 2009).
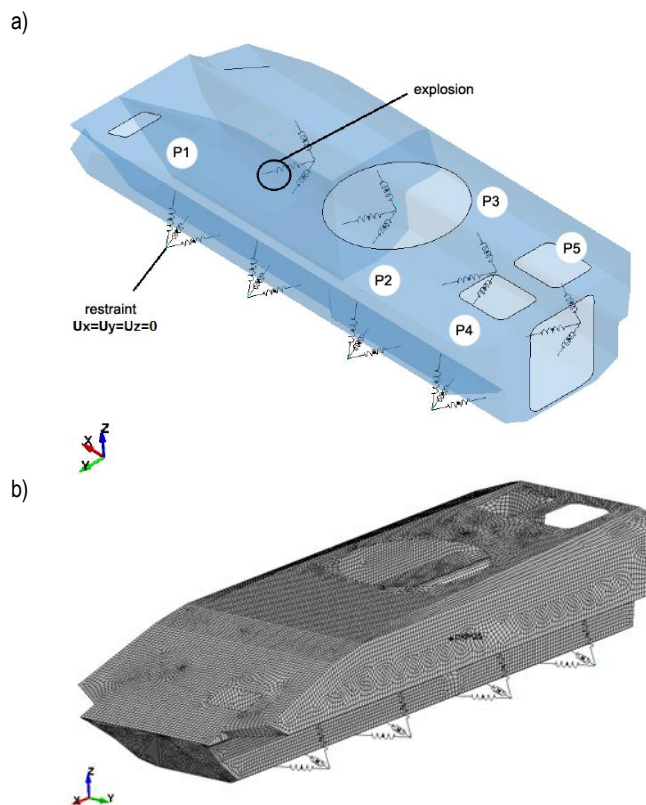
a)

b)

Fig. 4. Model of the AMV Rosomak: a) the distribution of passengers-soldiers in a three-dimensional coordinate system (x- the direction of travel, y – perpendicular direction to the direction of travel, z – vertical direction), b) digitized model
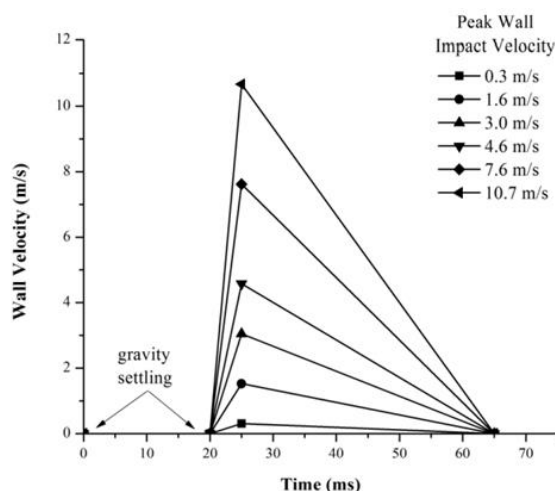

Fig. 5. Expected speed of the vehicle floor under the impulse of detonation (Nilakantan et al., 2009)

DE GRUYTER OPEN

Agnieszka Mackiewicz, Grzegorz Sławiński, Tadeusz Niezgoda, Romuald Będziński
Numerical Analysis of the Risk of Neck Injuries Caused by IED Explosion under the Vehicle in Military Environments
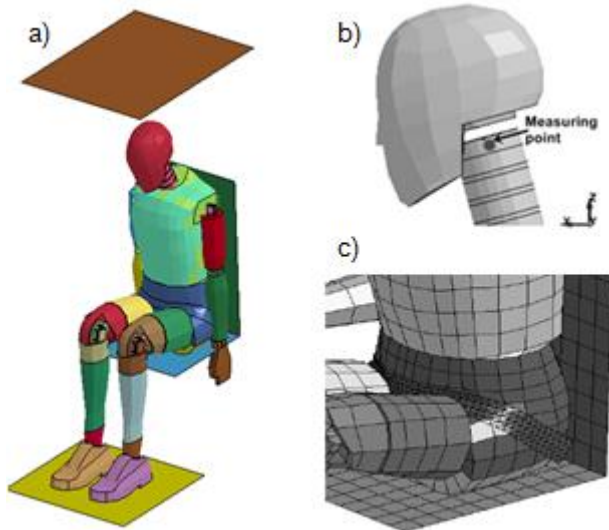
DOI 10.1515/ama-2016-0039

Fig. 6. Model: a) Mannequin type Hybrid III 50th Male Dummy, b) head and cervical spine indicating the measuring point, c) hip belt

In the second stage, the impact of detonating the load on the body of a soldier driving a combat vehicle was examined (P1) and two soldiers in the range of amphibious assault in extreme place-ment: P3-seating closest to the place of explosion and P4-seating situated furthest away from it. A variant of the fastened hip belt and its omission were considered for each of the cases (Fig. 6c). In the study the mannequin type model of a soldier used was the Hybrid III 50th Male Dummy (Fig. 6a).

During the analysis a change of acceleration and trajectory displacement of the measurement point located on the neck por-tion of the spine, at the height of the C1 circle with respect to the mounting points of the seat (Fig. 6b) in the coordinate system inside the vehicle at the time of 140ms was recorded.

3. RESULTS

Analysis of the impact of detonation on wheeled APCs under the right front wheel showed significant displacement in the Z vertical axis of 30cm and a small rotation on the sides (10cm) for both measuring points positioned on the floor and on the wall of the compartment of amphibious assault at an altitude of fas-tening the seat, which is shown in Figs. 7 and 8.

The results of the effect of the load detonation on the dis-placement of the soldiers' body are shown as characteristics depending on the x, y, z displacement components in time (Fig. 9). There are differences in the range of movements for each of the directions in the coordinate system of the vehicle on the graphs. In the case of the soldier driver (P1), the smallest move-ment of the cervical spine ranging up to a maximum of 100 mm was observed along the y-axis. This indicates that during the explosion under the right wheel, less displacement of driver to the side occurs. The largest absolute displacement value is present in the x and z direction. In driver (P1) with a fastened belt and without belts, large displacement in the x direction can cause whiplash injury and spinal compression injury. Attaching the belt to the driver's seating during the event results in the displacement values in the x direction not being characterized as linear, but wavy, which indicates a limitation of neck movement with the head and forcing their oscillatory motion.
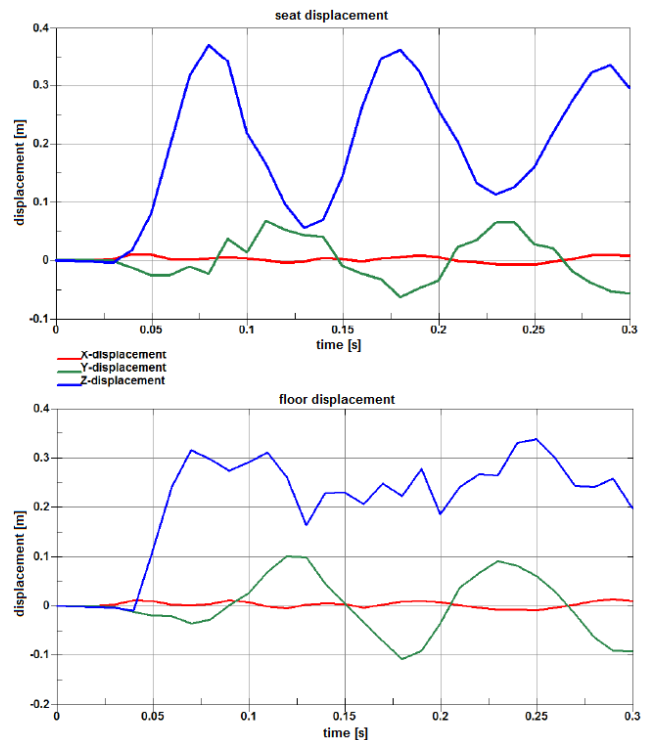
Fig. 7. Charts of displacement components of hull measuring point
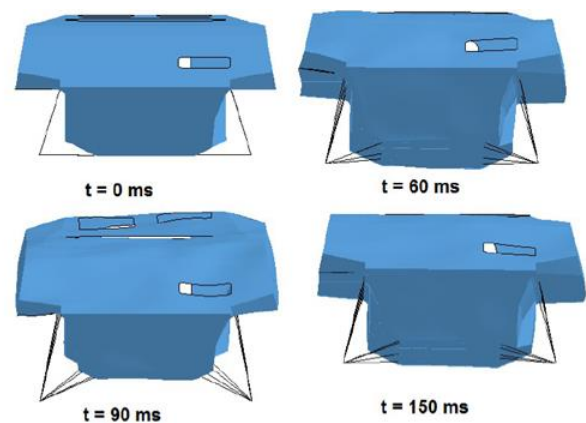
Fig. 8. Displacement of hull

In the P4 soldier (most distant from the place of explosion) with and without fastened belts, the component of displacement in the x-axis achieves peak values. Soldiers P3 and P4 are at higher risk of compression injuries associated with a shift in the z direction. We observe the movement of both dummies in the x direction as a consequence of the distribution of seats along the walls of the amphibious assault compartment and the slowdown of vehicle as a result of the explosion. As a result, it exposes the cervical spine to lateral bending. In the variant with a fastened seat belt, x displacement reaches a value of approximately four times lower than displacement values when the belt is not fas-tened. In this case, changing the position of the measuring point on the neck of a soldier (P4) in the y direction has a value almost twice higher than for the P3 soldier. It is worth noting that the displacement in the case of the P4 soldier with a fastened seat belt has a positive and negative value which also indicates the possibility of flexion - hyperextension or flexion-rotational injury taking into account the displacement in the x-axis.

Fig. 9. Charts of displacement measuring points of driver dummies P1 passengers P4 and P5 with and without seat belt
in the co-ordinate system x-direction of travel, y-perpendicular direction to the direction of travel z-vertical direction

Fig. 10. Charts of acceleration measuring point of P3 and P4 dummies, with and without a seat belt

DE GRUYTER
OPEN

Agnieszka Mackiewicz, Grzegorz Sławiński, Tadeusz Niezgoda, Romuald Będziński
Numerical Analysis of the Risk of Neck Injuries Caused by IED Explosion under the Vehicle in Military Environments

DOI 10.1515/ama-2016-0039

The analysis of accelerations recorded at the point of measurement of the cervical spine for a P3 and P4 soldier (Fig. 10) showed the greatest acceleration in the direction of the z-axis. The grea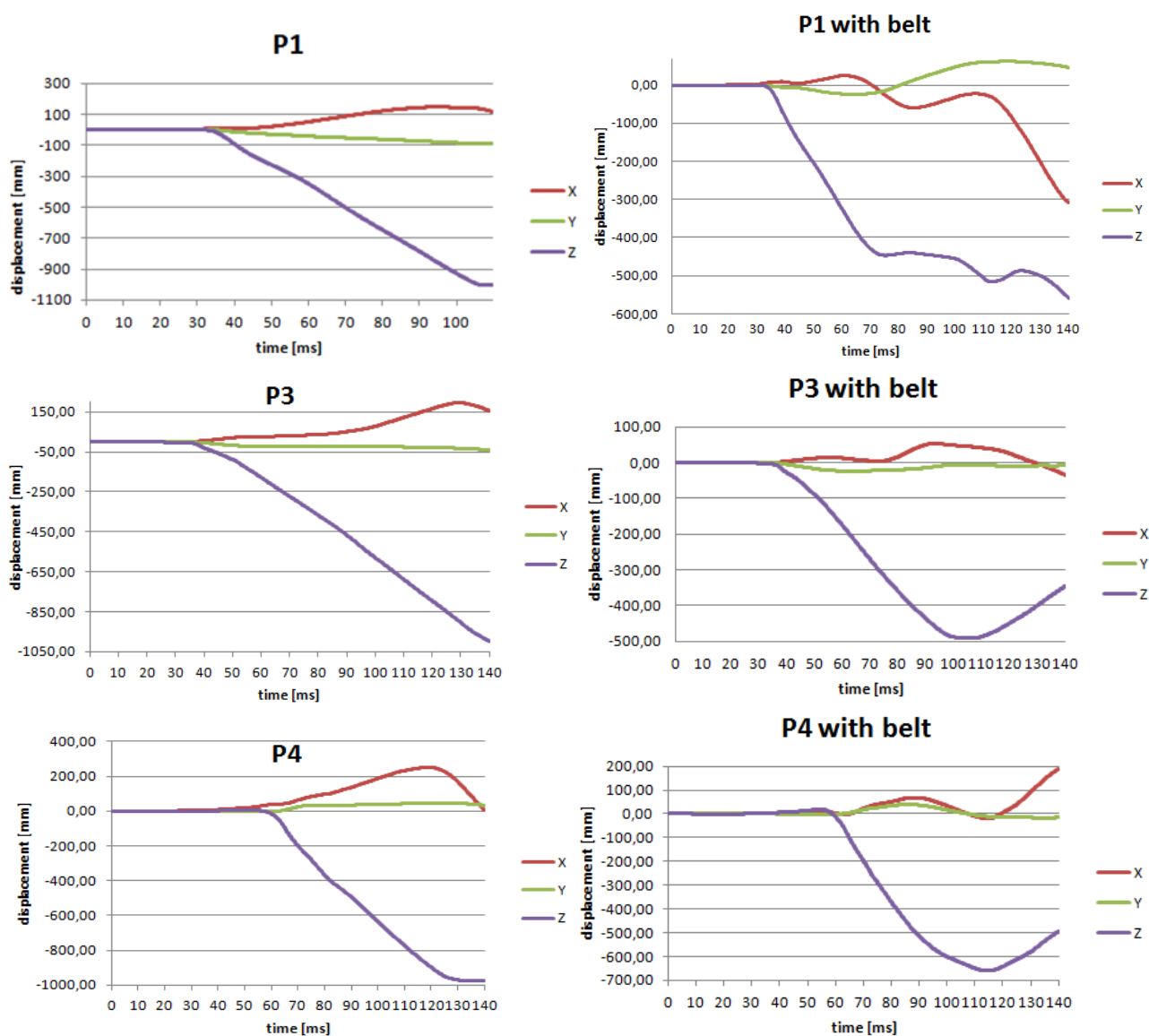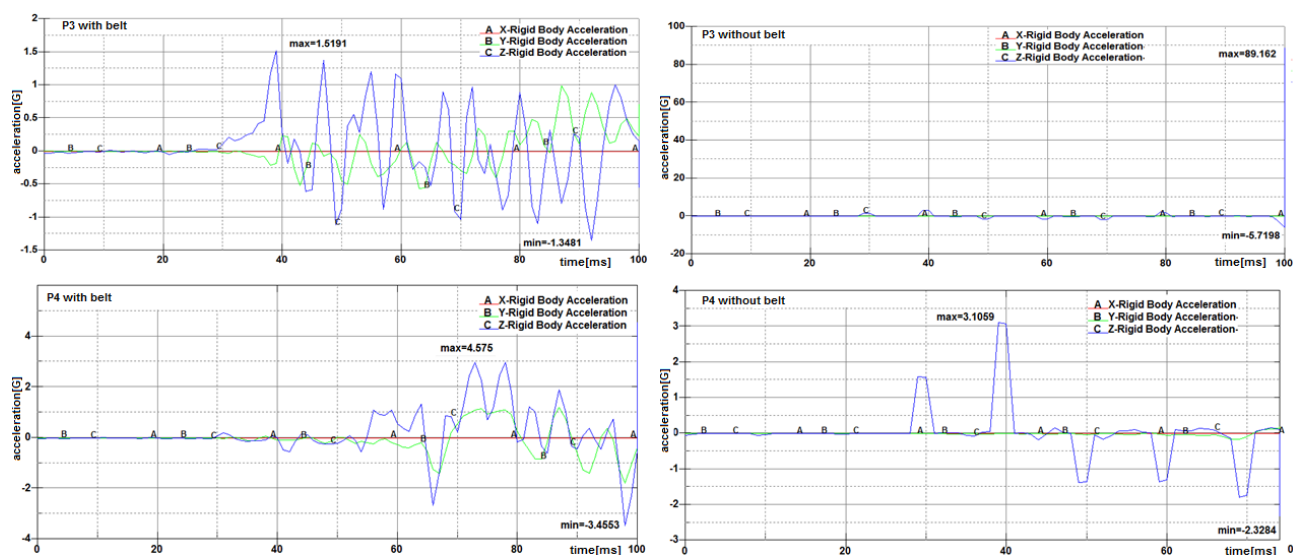test absolute acceleration values were reported in the P3 passenger without a seatbelt and it was almost 2 times higher than in the same case for the P4 passenger. The acceleration was recorded at 100 ms, which, as confirmed by the analysis of the course of the shock wave is most likely to damage the anatomical structures. It is worth noting that the P4 passenger is located closest to the explosion site and receives the greatest acceleration from the floor and the affixed place of their seating. Recognizing the mechanism and direction of movement enables the prediction of possible traumatic changes in the neck column of soldiers exposed to the shock wave.

4. DISCUSSIONS

Injuries of passengers of military vehicles are the result of floor acceleration changes occurring as a result of pressure from the blast. The mechanism of compressive strength of the cervical spine is caused by exulting the soldier with the seat and his head hitting the roof of the vehicle. In analysing the cases of explosion in front part of the vehicle, it should be noted that the driven vehicle crashing into an explosive charge comes to a halt as a result and there is destabilization and displacement in the vertical or upright-side which was also observed in the test case. Doing so may prevent other traumatic mechanisms than only compression. It is important to study both displacements caused by the explosion and displacement transmitted through seats on the individual segments of the bodies of soldiers (Ramasamy et al., 2011). Three-dimensional analysis of the trajectory movement of each of the soldiers enables the probable dysfunction of the cervical spine caused by extortion as an IED explosion to be specified. The cervical spine is particularly susceptible to damage when the corps of the body relative to the neck is subjected to sudden acceleration or deceleration (Schmitt et al., 2010, Cronin, 2011). The results obtained in the course of research allow for the classification of cases with soldiers in two groups. The first one is a P1 soldier-driver, the other is a P3 and P4 amphibious assault soldier. The basis of classification is to consider the neck and head movement relative to the force derived from an IED explosion. In both cases there is a displacement of all the soldiers in the z-axis and x-axis, which is the direction of travel of the vehicle. The difference is the location of the seat relative to the direction of travel, wherein the P1 soldier is seated in the direction of driving, and in the perpendicular direction, additionally sitting opposite each other. The consequence of such an arrangement of seating is the back movement of the P1 driver, causing the forward bend and backward hyperextension in the sagittal plane in the case of belts fastened to the sides and flexion in the frontal plane for the P3 and P4 soldiers. For the the variant without belts, which forces oscillatory motion in the direction of the x-axis, displacement in accordance with only one vector - flexion of P1, and lateral bending one side of P3 and P4, is observed. Cronin (2014) describes the phases of whiplash injury in his work. Kinematic response of the cervical spine and head during this type of damage is reduced to generating "S" shape in the neck in the first phase, by withdrawing the lower vertebrae in the back (extension) and upper vertebrae with the head forward (flexion). Then

there is movement of the head backwards and hyperextension as a result of inertia of the entire spinal column (Cronin, 2014). A similar trajectory can be observed in our case for the P1 soldier, so an accession of ligament damage which can cause instability is probability. The mechanism of whiplash injury may cause damage to both the back (PLL - posterior longitudinal ligament) and front (ALL - anterior longitudinal ligament) ligaments. Depending on the vector of the applied load during accelerated and delayed injury, it can include a hyper flexion mechanism (destruction of the LF Flavum Ligament and the ISL Interspinous Ligament) or hyperextension (destruction of the ALL anterior longitudinal ligament and tear of the FC Facet Capsule) (Ivancic et al., 2004, Panjabi et al., 2006). Leahny (2012) conducted an experimental and numerical simulation studying the impact of whiplash injury to the ligaments of the kinematics of the spine. The researcher found that damaged ligaments do not limit movement and are primarily responsible for the increase of its range, thus reducing stability. At the same time stating that after the simulation of whiplash injury, the relaxed ligaments force the necessity of using the same degree of clinical stabilization as in patients with completely torn structures (Leahy et al., 2012). Instability associated with dysfunction of the ligaments can lead to dislocation of the spine column (column buckling or fracture), thereby causing pressure on the nerve structures and vessels. As shown for each soldier, there is considerable displacement in the vertical axis Z, which increases the risk of the head hitting the roof of the vehicle. This results in a high probability of compression injury. According to the experimental studies of Denis (1983) compression fracture is located most often in the middle of the front of the vertebral body; however, it often comes up to the rear surface and the endplates, which may result in fragments penetrating deep into the spinal cord (Denis, 1983).

The type of dysfunction occurring on the traumatology base depends on where and how the tissue structures are load. Injuries of the upper segments are directly related to the force applied from the skull to the atlanto-occipital joint, and the lower segments are caused by impact forces directly to the vertebral body and the lever arm of force of several adjacent segments as in the case of P1 soldiers (Cusick et al., 2002). Similar conclusions were reached by Daffner (2006) and Robertson (2002) analyzing the cases in medical databases. The researchers showed that the fracture occurred at every level of the vertebrae, but the large majority of cracks occur in the extreme segments (Daffner et al., 2006, Robertson et al., 2002). The damage at these levels are usually caused by trauma on the mechanism of compression and flexion, causing comminuted fractures of the vertebral bodies (DeWit et al., 2012). According to Pintar (1998) in order to evaluate mechanisms of cervical injuries, the analysis of the rate of increase in the force and value and direction plays a key role. The researcher confirms that most of the damage of the cervical spine and the spinal cord is due to fractures and dislocations which are caused by the compression and flexion mechanism. Experimental studies determined that there is a 50% probability of damage at a load speed of 4.5 m / s and achieving a force of 3.9kN (Pintar et al., 1998).

Experimental studies have shown that damage to the lower segments of the cervical spine occurs when the operating acceleration is in the range of 17-25g (g=9.81m/s^2). In the case of appreciable accelerations of 34-38g it was noted that the resulting dysfunctions are located at the upper vertebrae and at the connection of the skull to the spine (Levine, 1994). Analysis of the studies of absolute acceleration values for a P3 and P4 soldier

is in the range corresponding to Levine (1994) and the possibility of injuries in the lower segments of the cervical spine. The maximum acceleration values of 5.72 g were reported for a P3 soldier located on the seat closest to the explosion in the case of a hip belt not being fastened. In the case of a lap belt being fastened, acceleration in the z-axis was almost 75% lower. For a P4 soldier, the situation was opposite. In the variant of a fastened lap belt, acceleration in the z-axis was 30% higher than in the case of the hip belt being omitted. It should be noted that the explosion caused displacement for this passenger in the Z-axis of 150mm higher than in variant despite a fastened seat belt.
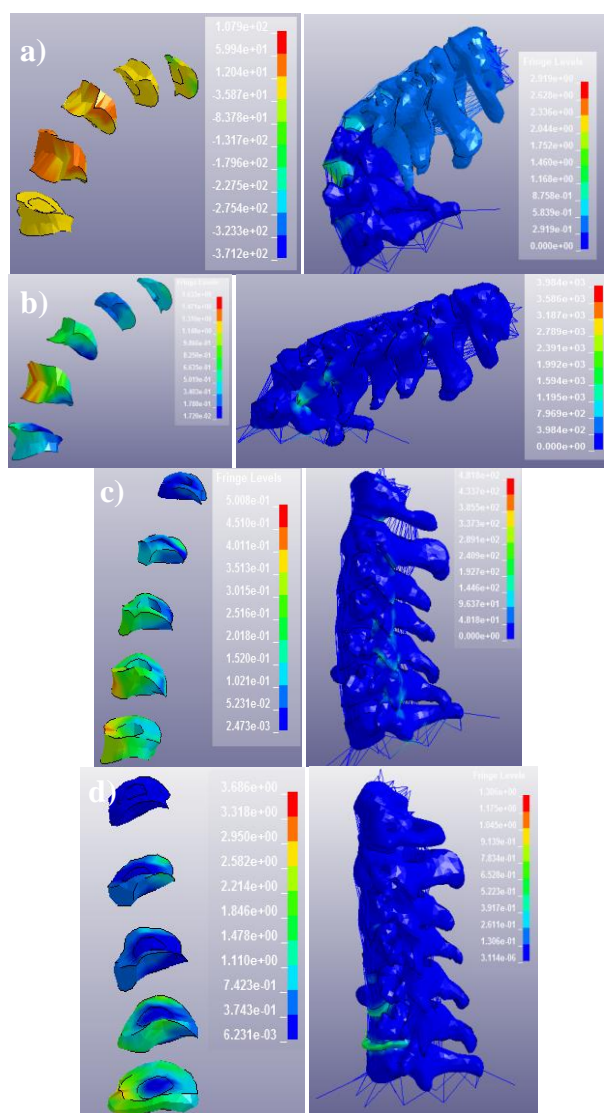

Fig. 11. The strain distribution in the intervertebral discs and spine column: a) P4 without belts, b) P4 with belts, c) P3 without belts, d) P3 with belts

Strain distribution as shown in Fig. 11 was analyzed for P3 and P4 soldiers. According to their placement, the biggest changes on the destructive ground occurred in the lower segments of the cervical spine, which were confirmed by the results obtained in the research of Levine (1994) (Levine, 1994). This was particularly noticeable in the structure of the C5C6 and C6C7 intervertebral disc. Bambach (2013) also conducted research on the impact of a passenger's head hitting the roof of the vehicle during a collision and the possibility of cervical spine injuries. The

results obtained by the researcher are similar to results obtained in the study. Bambach (2013) states that most of the damage occurs at the level of C5-C7, and the mechanism of damage is compression with the head extension or lateral bending. As a result of these mechanisms, Bambach informs that fracture of the lamina vertebral, intervertebral joint dysfunction, anterior longitudinal ligament (ALL) and posterial longitudinal ligament dysfunction (PLL) most often occurs (Bambach et al., 2013).

Hryciów (2013) has sought to assess the level of dynamic loads acting on an armored personnel carrier and its crew during frontal collisions at low speeds. The study provides that there is a substantial threat to soldiers, resulting from the high level of load inertia during impact and deceleration of the vehicle in the way. As a result of experimental collision studies using dummies of the Hybrid III 50th Male dummy localized between the amphibious assault and the driver (all fastened in with a lap safety belt) the researcher analyzes the trajectory movement of soldiers. In the case of the driver, the maximum flexion of the cervical spine after 120 ms from the moment of impact is observed.

Due to the use of the safety belt, movement of the whole body is limited. After 340 ms from the moment of impact, the head is tilted up to the rear and the trunk is halted on the seat, which is characteristic in case of frontal collisions. Different behavior is observed for a dummy in range of amphibious assault. Approximately 220 ms after collision, maximum displacement of the dummy occurs. The trunk and head are first bent to the right, with the simultaneous forward inclination and slight rotation of the vertical axis. Hryciów notes the displacement acting on the neck of the dummies during the 5 trials, which are in the range 2.44-5.97g are similar to results obtained by us for P3 and P4 soldiers (Hryciów et al., 2013).

It is worth noting that the highest probability of compression injury occurred in the P3 soldier without belts with whom we recorded the biggest acceleration in the x-axis of up to a value of nearly 90g. This fact can be explained by the smallest distance of the seat in relation to the explosion site.

Vertebral fractures are combined with application of variable force and hence Yogananda and Stemper (2013) drew attention to the issue of the vertical load of cervical spine in relation to combat injuries. The basis of their study was to measure the force acting on the vertical axis of the cervical spine during the compression and swinging impact, and effect of dynamic loads on the spine intact. Injuries differ from each other, during the action of the mechanism of pure compression, vertebral compression occurs and flexion mechanism causes distraction of the rear parts of the spine and injuries of joints, in reaction to stress in the upper part of the cervical spine injuries occur and fracture of endplates separating adjacent intervertebral discs. Yogananda and Stemper (2013) put forward the thesis that other biomechanical reaction results are to be obtained by applying axial compressive force to formulations, but by using a higher loading speed (Yoganandan et al., 2013).

Knowledge about the mechanisms of damage and of the cervical spinal column resulting from the instability in combat is essential in clinical practice. Anticipation and correct diagnosis of dysfunction and their classification as stability or instability is extremely important both in the prognosis and during first conservative treatment or surgical field hospitals.

Agnieszka Mackiewicz, Grzegorz Sławiński, Tadeusz Niezgoda, Romuald Będziński
Numerical Analysis of the Risk of Neck Injuries Caused by IED Explosion under the Vehicle in Military Environments

DOI 10.1515/ama-2016-0039

5. CONCLUSION

Irrespective of the seating of the soldier, in connection with displacement in the vertical axis, there is a high probability of hitting his head on the roof of the vehicle thereby a compressional injury to the cervical spine occurs. The effect of fastening belts is undoubtedly significant, since they protect the soldier before moving under the influence of mass forces and the head hitting hull fittings. The use of safety belts affect the trajectory of head movement in relation to the body, giving rise to displacement of the neck in the sagittal and lateral plane.

REFERENCES

1. **Bambach M.R., Grzebieta R.H., McIntosh A.S., Mattos G.A.** (2013), Cervical and thoracic spine injury from interactions with vehicle roofs in pure rollover crashes, *Accident Analysis and Prevention* 50, 34– 43.
2. **Brzozowski R., Guła P., Sanak T.** (2014), The army security in the aspect of threats resulting from the use of improvised explosive devices, Red.: S. Kowalkowski, B. Bębenek, T. Całkowski, Postexplosion soft tissue injuries, *National Defence University Publishing House*, Warsaw (in polish).
3. **Cronin D**. (2014), Finite element modeling of potential cervical spine pain sources in neutral position low speed rear impact, *Journal of the mechanical behavior of biomedical materials*, 33, 55–66.
4. **Cusick J.F., Yoganandan N.** (2002), Biomechanics of the cervical spine 4: major injuries, *Clinical Biomechanics*, 17, 1–20.
5. **Daffner R.H., Sciulli R.L., Rodriguez S.A., Protech J.** (2006), Imaging for evaluation of suspected cervical spine trauma: a 2-year analysis, *Injury: International Journal of the Care of the Injured*, 37(7), 652–658.
6. **Denis, F.** (1983), The three column spine and its significance in the classification of acute thorocolumbar spinal injuries, *Spine*, 8(8), 817–831.
7. **DeWit J.A., Cronin D.S.** (2012), Cervical spine segment finite element model for traumatic injury prediction, *Journal of the Mechanical Behavior of Biomedical Materials*, 10, 138–150.
8. **Heider N, Denefeld V, Holzwarth A.** (2010), Methods for the analysis of global IED effects on military vehicles, 5t*h European Survivability Workshop*, Alesund Norway.
9. **Hryciów Z., Borkowski W., Wysocki J., Rybak P., Wiśniewski A.** (2013), Experimental researches of safety of armoured personnel carrier crew during collision with obstacle, T*he Archives of Automotive Engineering*, 61, 87-96.
10. **Ivancic, P.C., Pearson, A.M., Panjabi, M.M., Ito, S**. (2004), Injury of the anterior longitudinal ligament during whiplash simulation, *European Spine Journal*, 13(1), 61–68.
11. **Krzystała E., Mężyk A., Kciuk S.** (2011a), Analysis of the influence of the blast on wheeled military vehicle and their crew, Fast Tracked Vehicles, 28(2), 99-110.
12. **Krzystała E., Mężyk A., Kciuk S.** (2011b), Analysis of threat to crew posed by explosion of charge placed under wheeled armoured vehicle, *Jouranl of Science of the Gen. Tadeusz Kosciuszko Military Academy of Land Forcs*, 1(159) , 145-154.
13. **Leahy P.D., Puttlitz Ch.M.** (2012), The effects of ligamentous injury in the human lower cervical spine, *Journal of Biomechanics*, 45, 2668–2672.
14. **Levine R.S.** (1994), *Head and Neck Injury*, Society of Automotive Engineers, USA.
15. **Nilakantan G. Tabiei A.** (2009), Computational Assessment of occupant Injury Caused by Mine Blasts underneath Infantry *Vehicles, Int. J. Vehicle Structures & Systems*, 1(1-3), 50-5.
16. **Operating Instructions, description and use** (2005), 8x8 Wheeled Armored ROSOMAK Tower HITFIST 30 mm, Wojskowe Zakłady Mechaniczne S.A, Siemianowice Slaskie.
17. **Panjabi, M.M., Maak, T.G., Ivancic, P.C., Ito, S.** (2006), Dynamic intervertebral foramen narrowing during simulated rear impact, *Spine*, 31(5), 128–134.
18. **Pintar F.A, Yoganandan N., Voo L.** (1998), Effect of age and loading rate on human cervical spine injury threshold, *Spine Sep*, 15;23(18), 1957-62.
19. **Protocol HFM-090/TG-25** (2007), The mine detonation process and occupant loading.
20. **Ramasamy A., Masouros S.D., Newell N., Hill A.M**. (2011), Proud W.G., Brown K.A., Bull A.M.J., Clasper J.C., In-vehicle extremity injuries from improvised explosive devices: current and future foci, *Phil. Trans. R. Soc.*, 366, 160–170.
21. **Robertson A., Branfoot T., Barlow I.F., Giannoudies P.V.** (2002), Spinal injury patterns resulting from car and motorcycle accidents, *Spine*, 27(24), 2825–2830.
22. **Schmitt K.-U., Niederer P., Muser M., Walz F.** (2010), *Trauma Biomechanics*, Third Edition, Springer, Berlin.
23. **Sławiński G.** (2012)**,** *Pictures of AMV Rosomak after IED explosion*, Afghanistan - own resources.
24. **Sławiński G., Niezgoda T., Barnat W.** (2013), Numerical analysis of the influence of blast wave on human body, *Journal of KONES Powertrain and Transport*, 20(3), 113-122.
25. **Wojtkowski M., Ziółek J., Płomiński J., Waliński T.** (2014), The army security in the aspect of threats resulting from the use of improvised explosive devices, Red.: S. Kowalkowski, B. Bębenek, T. Całkowski, Postexplosion analysis musculoskeletal injuries of Polish soldiers in military contingents - preliminary, *National Defence University Publishing House*, Warsaw (in polish).
26. **Yang Y., Liou W.W., Sheng, J.Gorsich, D., Arepally, S.**, (2013) Shock wave impact simulation of a vehicle occupant using fluid/structure/ dynamics interactions, *International Journal of Impact Engineering*, 52, 11-22.
27. **Yoganandan N., Stemper B.D., Pintar F.A., Maiman D.J., McEntire B.J**., (2013), Chancey V.C., Cervical spine injury biomechanics: Applications for under body blast loadings in military environments, *Clinical Biomechanics*, 28, 602–609.

RATCHETING SIMULATION IN A TITANIUM-STEEL BIMETALLIC PLATE BASED ON THE CHABOCHE HARDENING MODEL

Aleksander KAROLCZUK*

*Faculty of Mechanical Engineering, Opole University of Technology, ul. Mikołajczyka 5, 45-271 Opole, Poland

a.karolczuk@po.opole.pl

Abstract: The paper presents the results of fatigue loading simulation applied to bimetallic model using the Chaboche kinematic hardening rule. Three cases of simulations were performed: (i) without residual stresses; (ii) considering residual stresses and (iii) considering asymmetrical geometry of bimetal, i.e. cross area reducing under tension period of loading. Experimental results exhibit the ratcheting phenomenon in titanium-steel bimetallic specimens. The observed ratcheting phenomenon could be explained by the third case of simulation which is supported by detection of microcracks in the vicinity of welded area.

Key words: Ratcheting Phenomenon, Explosive Welding, Cyclic Loading, The Chaboche Kinematic Hardening Model

1. INTRODUCTION

Bimetallic plates are sometimes required in specific industry equipment where different physical properties are needed in single plate. One layer of bimetallic plate offers for example excellent resistance against corroding medium and the second one provides appropriate mechanical stiffness and strength (Sulym et al., 2016; Ganczarski and Szubartowski, 2015). But, these different physical properties are often the reason that the required materials are unweldable by standard methods. In such case one of the alternatives is to use explosive welding technology (Findik, 2011; Crossland, 1982). This technology applies energy of detonation that accelerates one metallic material (the flayer) that collides to the base material and the metallic bond is formed. However, depending on explosive welding parameters and mechanical properties of parent materials the interface between the joint metals is characterized by different types of inhomogeneities (Paul et al., 2012; Lazurenko et al., 2016; Gloc et al., 2016). These inhomogeneities could be considered as defects and stress rising factors having influence on the monotonic and fatigue strengths (Song et al., 2011; Karolczuk et al., 2013). Besides, the unique mechanical and structural properties of joint area there are also residual stresses locked during explosive welding or introduced by the heat treatment (Karolczuk et al., 2014). Experimental tests under fully reversed cyclic loading exhibit ratcheting phenomenon in titanium-steel bimetallic specimens (Karolczuk et al., 2013). According to (Hubel, 1996) if the element has inhomogeneous elastic-plastic properties the structural ratcheting could appear since the two materials undergo plastic strains under different stress states.

There are two aims of the paper. The one is to show that the structural ratcheting in titanium-steel plate could not be simulated using the Chaboche hardening model even taking into account residual stresses. The second aim is to propose a model able to simulate the ratcheting phenomenon in the bimetallic plate.

2. EXPERIMENT

The tested and analyzed specimens were cut out from large bimetallic plate (4330x3150 mm) obtained during explosive welding process. The titanium plate (Titanium Grade 1) with thickness equal to 6 mm was cladded on the steel plate (S355J2+N) with thickness equal to 40 mm. The part of plate for specimens was cut out from the corner and the ignition point was in the center of the plate. The chemical composition and basic mechanical properties of parent materials are presented in Tab. 1 and 2. The bimetallic plate after the welding process was subjected to the heat treatment. The heat treatment consists in soaking by 90 minutes at 600oC. After the heat treatment the plate undergoes the cold flattening process. The flat specimens were cut out from the bimetallic plate and subjected to fatigue tests described in details in Karolczuk et al. (2013), Karolczuk and Kowalski, (2014).

Tab. 1. Chemical composition of parent materials

S355J2+N steel (in weight-%)						**Titanium Grade 1** (in weight-%)					
C	C	Si	Mn	P	S	C	Fe	H	N	O	Ti
0.22	0.22	0.55	1.60	0.025	0.025	0.10	0.20	0.015	0.03	0.18	99.5

Tab. 2. Mechanical properties of S355J2+N steel and Tytanium Grade 1

Material	**R$_{eH}$, MPa**	**R$_m$, MPa**	**E, GPa**	**ν, -**	**A$_5$, %**
S355J2+N	382-395	598-605	206-220	0.27-0.30	24-34
Titanium Grade 1	189-215 (R$_{p02}$)	308-324	100-105	0.37-0.39	43-56

3. THE CHABOCHE HARDENING MODEL

The Chaboche model applied in simulation is a basic version consisted in the following decomposition rule of the kinematic hardening (Chaboche et al. 1979, 2012):

$$da = \sum_{i=1}^{3} da^{(i)},$$
$$d a^{(i)} = \frac{2}{3} C^{(i)} d\varepsilon^p - \gamma^{(i)} a^{(i)} dp,$$
$$dp = \sqrt{\frac{2}{3} d\varepsilon^p : d\varepsilon^p},$$

(1)

where: a – back stress tensor, $C^{(i)}$, $\gamma^{(i)}$ – material parameters, ε^p – plastic strain tensor, : – inner product, d – increment. The constitutive equations (1) were completed with the associated flow rule:

$$d\varepsilon^p = d\lambda \frac{\partial f}{\partial s} = \frac{ds:n}{H} n,$$

(2)

where: H – the plastic modulus, s – the deviatoric stress tensor, n – tensor normal to yield surface f of the Huber-Mises-Hencky hypothesis

$$\frac{3}{2}(s - a):(s - a) - \sigma_y^2 = 0,$$

(3)

where σ_y is the yield stress.

4. IDENTIFICATION OF MATERIALS PARAMETERS FOR THE CHABOCHE HARDENING MODEL

One of the main problem in the Chaboche hardening model is identification of values of material parameters: $C^{(i)}$, $\gamma^{(i)}$. In the identification procedure the standard Ramberg-Osgood plastic strain-stress characteristic was used:

$$\varepsilon_a^p = \left(\frac{\sigma_a}{K'}\right)^{1/n'},$$

(4)

where: ε_a^p – plastic strain amplitude; σ_a – stress amplitude; K', n' – cyclic hardening coefficient and exponent, respectively. The materials constants are presented in Tab. 3.

Tab. 3. Mechanical properties of S355J2+N steel and Titanium Grade 1 (Karolczuk and Kowalski, 2014; Gómez et al., 2011)

Material	K', MPa	n', -
S355J2+N	721	0.1258
Titanium Grade 1	190	0.0641

Under uniaxial stress state (monotonic tension) the constitutive equation of the Chaboche model could be solved and the relation between tension stress and plastic strain is as follows:

$$\sigma_a = \sigma_y + \sum_{i=1}^{3} \frac{C^{(i)}}{\gamma^{(i)}}\left(1 - e^{-\gamma^{(i)}\varepsilon_a^p}\right).$$

(5)

Identification procedure consisted in a minimization of parameter δW being the function of:

$$\delta W = \frac{\int |dW|}{W_{RO}} 100\%$$

(6)

where: $W_{RO} = \int (\varepsilon_a^p)^{n'} K' d\varepsilon_a^p,$

(7)

$$dW = \left(\sigma_y + \sum_{i=1}^{3} \frac{C^{(i)}}{\gamma^{(i)}}\left(1 - e^{-\gamma^{(i)}\varepsilon_a^p}\right) - (\varepsilon_a^p)^{n'} K'\right) d\varepsilon_a^p.$$

(8)

In other words, it is a minimization of difference in plastic strain energy densities (areas under the curves $\varepsilon_a^p - \sigma_a$) calculated using both curves, i.e. eq. 4 and 5. Minimization was performed using iteration algorithm of the interior point method (function fmincon in Matlab R2011b - optimization toolbox). Final fitting features between both curves are presented in Figs. 1 and 2. The values of determined material constants are presented in Tab. 4.
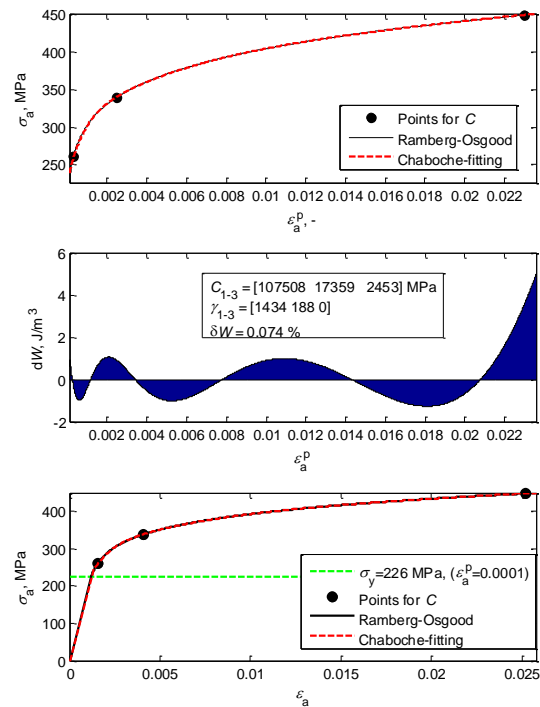

Fig. 1. The stress-strain curves and dW (eq.8) parameter plots with the computed materials constants for the Chaboche model for the S355J2+N steel
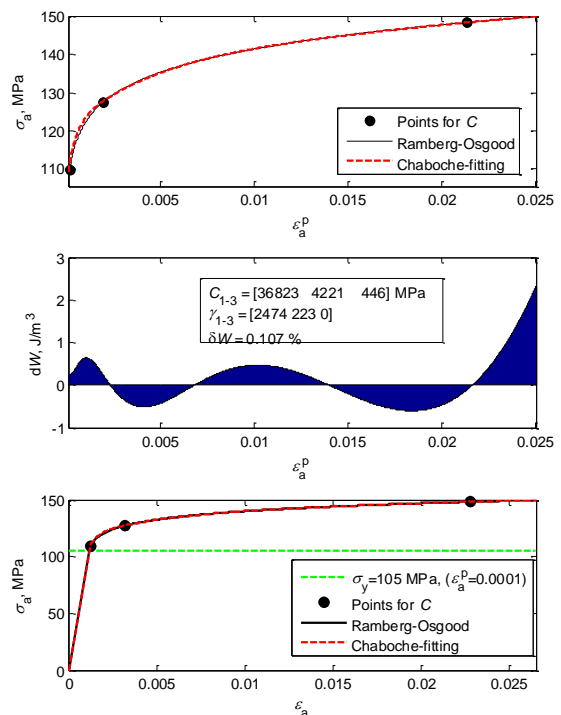

Fig. 2. The stress-strain curves and dW (eq.8) parameter plots with the computed materials constants for the Chaboche model for the titanium grade 1

Tab. 4. Material parameters for the Chaboche hardening model

Material	σ_y, MPa	$C^{(1)}$, MPa	$C^{(2)}$, MPa	$C^{(3)}$, MPa	$\gamma^{(1)}$	$\gamma^{(2)}$	$\gamma^{(3)}$
S355J2+N	226	107508	17359	2453	1434	188	0
Titanium Grade 1	105	36823	4221	446	2474	223	0

5. BIMETALLIC MODEL

Loading scheme and model geometry are presented in Fig. 3. The equilibrium equations were formulated with the following assumptions:
— full and perfect connection between metals in form of plane without defects,
— uniform distribution of strain increments $d\varepsilon$,
— stress increment distributions $d\sigma(Ti)$, $d\sigma(St)$ are uniform for each layer,
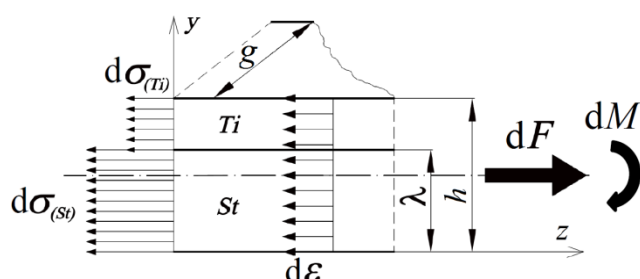— uniaxial stress state ($\sigma_{zz} \neq 0$, Fig.3).

Fig. 3. Geometry and loading condition of bimetallic model

The equilibrium equations are written in the following forms

$$d\sigma(Ti)g(h - \lambda) + d\sigma(St)g\lambda - dF = 0 \qquad (9)$$

$$d\sigma(Ti)g(h - \lambda)(h + \lambda)/2 + d\sigma(St)g\lambda 2/2 \qquad (10)$$
$$- dFh/2 - dM = 0$$

where: $d\sigma(Ti)$, $d\sigma(St)$– stress increments in titanium and steel layers, respectively; dF – force increment, dM – moment increment. Equation (9) is treated as the aim function that together with the constitutive equations of material hardening is solved incrementally in Matlab software. Residuals $Er(t)$ of equation (9) are traced and plotted in Figs. in next paragraph.

6. SIMMULATIONS

Analysis of influence of sinusoidal loading $F(t) = F_a sin(2\pi f t)$ (where f – frequency of loading; f = 4 Hz) on cyclic behavior bimetallic layers was performed with force amplitude F_a=24500 N that corresponds to experimental fatigue life N_{exp} equal to 26570 cycles. The observed ratcheting phenomenon for this specimen is shown in Fig. 4. Fig. 5 presents the changes in mean value of total strain cycle by cycle. The mean strain rate oscillates around 10^{-7} 1/cycle.

In simulations two initial stress state were considered (Tab. 5). In the case 0 it is assumed that residual stresses in both metals are equal to zero and in the second case it is assumed that residual stress state in titanium is -100 MPa (z direction, Fig. 3). The negative value comes from residual stress measurement and analysis of the heat treatment process (Karolczuk et al.,

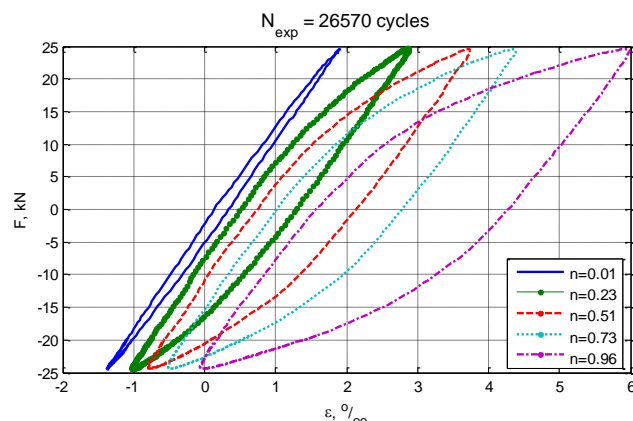2014). The positive value of residual stress in steel comes from the equilibrium of forces.

Fig. 4. Hysteresis loops $F - \varepsilon$ showing ratcheting phenomenon, i.e. strain accumulation in direction of tension, where $n = N/N_{exp}$ (damage degree)
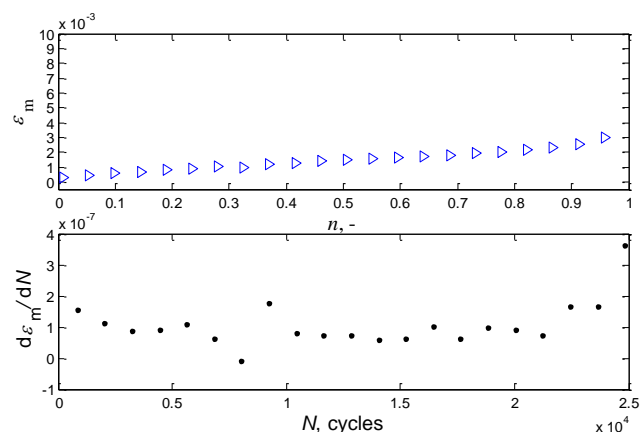

Fig. 5. Evolution of mean value of total strain and estimated mean strain rate

Tab. 5. Simulation cases

Material	Titanium Grade 1	S355J2+N
Simulation	σ_{res}, MPa	σ_{res}, MPa
0	0	0
1	-100	50

Results of simulations are presented in Figs. 6 and 7, where: (a), (b) final positions or yield surfaces in space $\sigma_z - \sigma_y$ for steel and titanium, respectively; (c) stress courses for steel and titanium; (d) strain courses; (e) hysteresis loops; (f) residuals of Eq. 9.

It could be noticed that the maximum value of $Er(t)$ does not exceed the value of 5·10-6 N. The strain amplitudes and mean values are stabilized after tens of cycles. Detailed analysis of stability of strain courses is presented in Figs. 8-11. Figs. 8a and 10a present simulated hysteresis loops $F - \varepsilon$, where ε is calculated without the residual stress influence, i.e. the starting point is assumed as $F(t = 0) = 0$ then $\varepsilon(t = 0) = 0$ (in titanium and steel layers, as measured by extensometer during fatigue test). Figs. 8b and 10b present the changes in the amplitudes and mean values of strain during subsequent cycles.
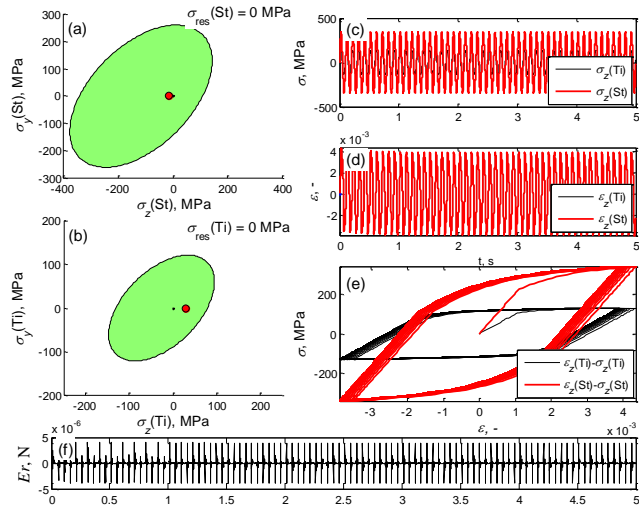
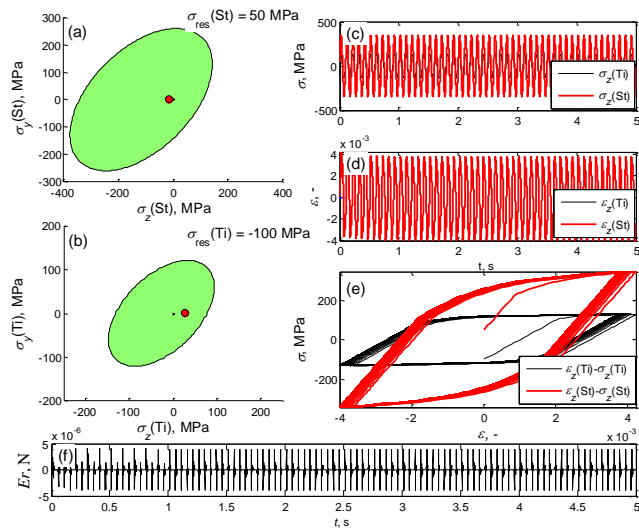**Fig. 6.** Behavior of bimetal under cyclic loading and case 0 of simulation

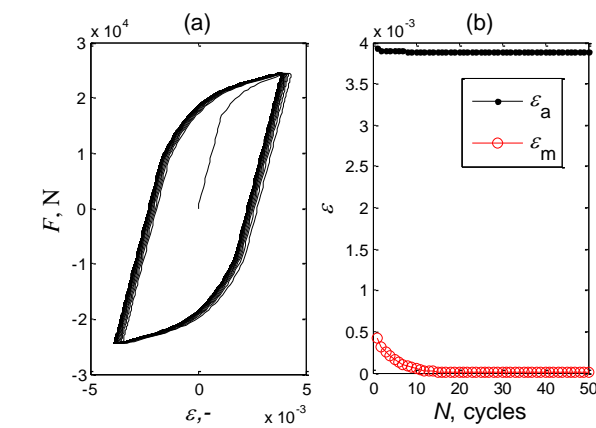**Fig. 7.** Behavior of bimetal under cyclic loading and case 1 of simulation

Fig. 8. Simulation: case 0. (a) Hysteresis loops $\varepsilon - F$;
(b) strain amplitudes ε_a and mean values ε_m
in function number of cycles N

The rates of strain amplitudes $d\varepsilon_a/dN$ and mean values $d\varepsilon_m/dN$ show precisely that for case 0 of simulation the strain rates achieve value below 10^{-10} 1/cycle after 37 cycles and for case 1 of simulation the strain rates achieve value below 10^{-10}

1/cycle after 49 cycles. The rate value equal to 10^{-10} 1/cycle could be treated as stabilization since, e.g. after 10^6 cycles the accumulated strain would be equal to 10^{-4}, i.e. around 2.5 % of strain amplitude. In case 1 of simulation the mean value of stress, i.e. residual stresses are relaxed very quickly in a few first cycles.
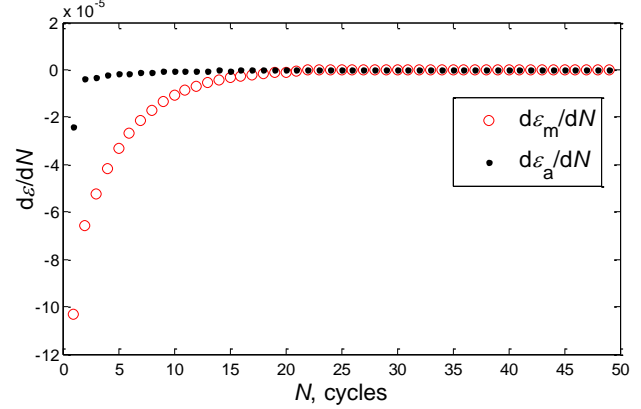
Fig. 9. Simulation: case 0. Rates of strain amplitudes ε_a
and mean values ε_m in function number of cycles N

The conclusion is that different cyclic properties of parent materials and even existence of residual stresses are not the cause of the experimentally observed ratcheting phenomenon.
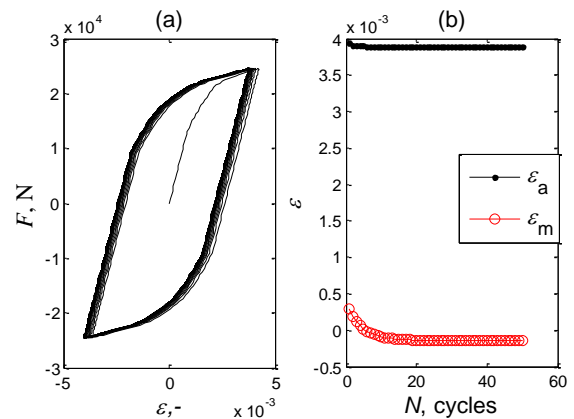
Fig. 10. Simulation: case 1. (a) Hysteresis loops $\varepsilon - F$; (b) strain amplitudes ε_a and mean values ε_m in function number of cycles N
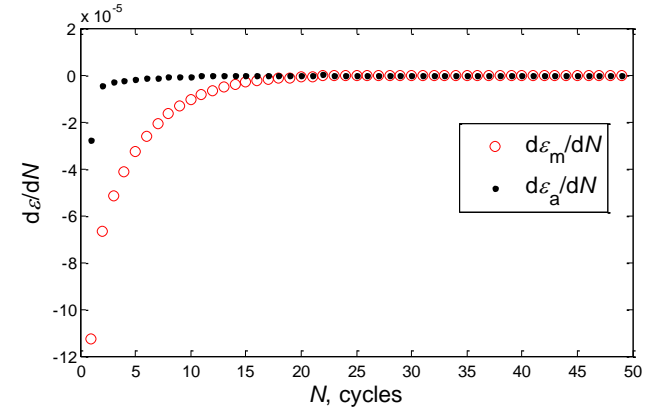
Fig. 11. Simulation: case 1. Rates of strain amplitudes ε_a
and mean values ε_m in function number of cycles N

The other reasons of ratcheting phenomenon in the analyzed bimetal that could be consider are specific structural and mechanical properties of joint area. During the collision of flayer plate with base plate very high pressure around 19-50 GPa is created in time around 2-5 μs (Walczak, 1989; Crossland, 1982) as a result thin very hard layer of intermetallics is formed (Paul et al., 2011) sometimes with larger local melted areas. Those melted areas could already have very short cracks (Fig. 12) before fatigue test. The melted areas could be the places of stress concentration and fatigue crack initiators (Fig. 13).

Fig. 12. Photo of joint area of one of tested bimetallic specimen before fatigue test
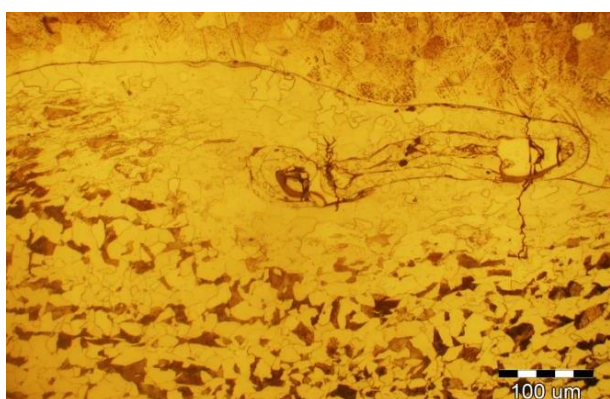

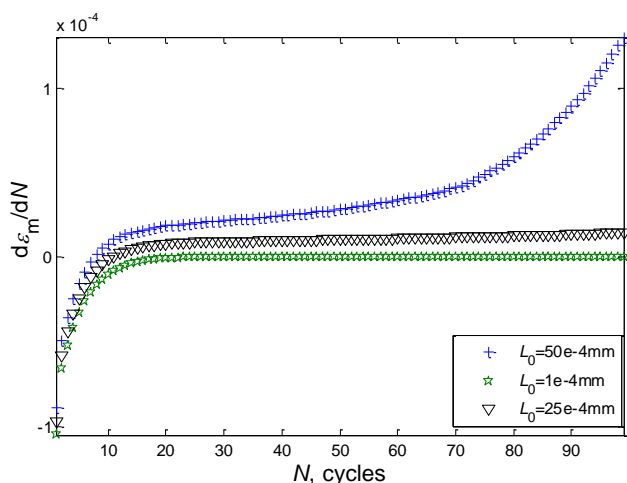**Fig. 13.** Photo of joint area after fatigue test (steel – low part of photo)

Fig. 14. Simulation with different crack lengths L_0. Rates of strain mean values ε_m in function number of cycles N for different crack lengths

In the third simulation the micro crack with length L_0 is introduced into model. This introduction is very simplified just in order to simulate the difference in force transmission between tension and compressive period of loading. Thus, under tension the crack decreased the cross section of specimen by $L_0 - g$ (Fig. 3) equally in both layers and under compressive period the cross section is not changed. The tension period were defined as $\varepsilon(t) > 0$ and $dF/dt > 0$. The results of simulations are presented in Fig. 14.

Fig. 14 shows that the strain rate of mean values strongly depends on the simulated crack length. For the crack length equal to 0.0001 mm the strain rate is close to experimental one, i.e. 10^{-7} 1/cycle (Fig. 5).

7. CONCLUSIONS

— Different elastic-plastic properties of parent materials used in the applied bimetallic and material models cannot explain the ratcheting phenomenon.
— The ratcheting phenomenon could be simulated using asymmetrical geometrical model of bimetal, i.e. cross area reduced under tension period of loading.
— The simulated strain rate using asymmetrical geometrical model of bimetal is very sensitive to the applied asymmetry.

REFERENCES

1. **Chaboche J., Dang Van K., Cordier G**. (1979), Modelization of the strain memory effect on the cyclic hardening of 316 stainless steel, *Structural mechanics in reactor technology. Transactions,* Vol. L, 1-10.
2. **Chaboche J.-L., Kanouté P. & Azzouz F**. (2012), Cyclic inelastic constitutive equations and their impact on the fatigue life predictions, *International Journal of Plasticity*, 35, 44–66.
3. **Crossland B.** (1982), *Explosive welding of metals and its application*, Clarendon Press, Oxford.
4. **Findik F.** (2011), Recent developments in explosive welding, *Materials & Design*, 32 (3), 1081–1093.
5. **Ganczarski A., Szubartowski D.** (2015), On The Stress Free Deformation Of Linear FGM Interface Under Constant Temperature, *Acta Mechanica et Automatica*, 9(3), 135-139.
6. **Gloc M., Wachowski M., Plocinski T., Kurzydlowski K.J.** (2016), Microstructural and microanalysis investigations of bond titanium grade1/low alloy steel st52-3N obtained by explosive welding, *Journal of Alloys and Compounds*, 671, 446–451.
7. **Gómez C., Canales M., Calvo S., Rivera R., Valdés J.R., Núñez, J.L.** (2011), High and low cycle fatigue life estimation of welding steel under constant amplitude loading: Analysis of different multiaxial damage models and in-phase and out-of-phase loading effects, *International Journal of Fatigue*, 33 (4), 578–587.
8. **Hubel H.** (1996), Basic conditions for material and structural ratcheting, *Nuclear Engineering and Design*, 162(1), 55–65.
9. **Karolczuk A., Kowalski M.** (2014), *Fatigue phenomena in steel-titanium bimetallic composite* (in Polish), Politechnika Opolska, Opole, Poland.
10. **Karolczuk A., Kowalski M., Bański R., Żok F.** (2013), Fatigue phenomena in explosively welded steel–titanium clad components subjected to push–pull loading, *International Journal of Fatigue*, 48, 101–108.
11. **Karolczuk A., Kowalski M., Kluger K., Żok F.** (2014), Identification of Residual Stress Phenomena Based on the Hole Drilling Method in Explosively Welded Steel-Titanium Composite, *Archives of Metallurgy and Materials*, 59 (3), 1129-1133.

12. **Lazurenko D.V., Bataev I.A., Mali V.I., Bataev A.A., Maliutina I.N., Lozhkin V.S., Esikov M.A., Jorge A.M.J.** (2016), Explosively welded multilayer Ti-Al composites: Structure and transformation during heat treatment, *Materials and Design*, 102, 122–130.

13. **Paul H., Faryna M., Prażmowski M., Bański R.** (2011), Changes in the bonding zone of explosively welded sheets, *Archives of Metallurgy and Materials*, 56 (2), 463–474.

14. **Paul H., Lityńska-Dobrzyńska L., Miszczyk M., Prażmowski M.** (2012), Microstructure and Phase Transformations Near the Bonding Zone of Al/Cu Clad Manufactured by Explosive Welding, *Archives of Metallurgy and Materials*, 57 (4), 1151-1162.

15. **Song J., Kostka A., Veehmayer M., Raabe D.** (2011), Hierarchical microstructure of explosive joints: Example of titanium to steel cladding, *Materials Science and Engineering: A*, 528 (6), 2641–2647.

16. **Sulym H., Pasternak I., Tomashivskyy M.** (2016), Boundary Integral Equations for an Anisotropic Bimaterial with Thermally Imperfect Interface and Internal Inhomogeneities, *Acta Mechanica et Automatica*, 10 (1), 66-74.

17. **Walczak Z.** (1989), *Explosive welding* (in Polish),WNT.

ANALYSIS OF PLASTIC DEFORMATION OF DOUBLE REDUCED SHEETS

Emil SPIŠÁK*, Janka MAJERNÍKOVÁ*, Emília DUĽOVÁ SPIŠÁKOVÁ**, Ľuboš KAŠČÁK*

*Faculty of Mechanical Engineering, Department of Technologies and Materials, Technical University of Košice,
Letná 9, 040 01 Košice, Slovakia
**University of Economics in Bratislava, Faculty of Business Economy with seat in Košice, Tajovského 13, Slovakia

emil.spisak@tuke.sk, jana.majernikova@tuke.sk, emilia.spisakova@euke.sk, lubos.kascak@tuke.sk

Abstract: This paper discusses the causes and the effects of plastic deformation of double reduced sheets under uniaxial and biaxial loading. It focuses on the specific inhomogeneity and localization of plastic deformation, which is analysed in detail. The uniaxial and the hydraulic biaxial tensile tests were used for material testing and the results were compared and evaluated. The final part of the paper deals with the microstructure of material deformations.

Key words: Tinplates, Double Reduction, Tensile Tests, Plastic Deformation

1. INTRODUCTION

An accurate determination of mechanical properties is one of the key issues in the analysis of behaviour of material deformation. Tinplate forming is characterized by a phenomenon of specific inhomogeneity, of which causes and effects are analysed in this paper. Tinplates can be classified according to the type of production, into the simply reduced (SR) and the double reduced (DR) sheets. The thickness of the sheets is effected by the method of production, and it ranges from 0.13 to 0.50 mm. A significant strain hardening of the material occurs during the process of production, with the use of a cold rolling tandem mill. This adverse effect is eliminated either by a continuous annealing (CA) or by a batch annealing (BA). Protection tin coating is applied on the modified material, it brings several advantages such as excellent formability, sufficient strength and corrosion resistance (European Standard 2001). Modern tinplate has several important advantages, including excellent drawability combined with good strength, good solderability and corrosion resistance.

DR tinplate is currently and mostly tested by the tension test (uniaxial tensile test). However, this test showed that there is severe variance in the case of identified mechanical and plastic properties. Significantly high variance is observed in the case of material plasticity which is demonstrated through the material elongation. The measured properties of DR tinplate after the elongation, which were identified by the uniaxial tensile test, tend to be very low (starting at 0.2%). We tried to experimentally test the behaviour of DR tinplate by means of a hydraulic biaxial tensile test which uses hydrostatic bulging and to analyse the root causes of non-homogenous plastic deformation with subsequent disruption of tested specimens during tension test (Spišák et al., 2012).

2. LOCAL PLASTIC DEFORMATION AND ITS PROGRESS

Plastic deformation of material can be generally divided into and dealt with at the three levels, namely micro, meso and macro level. In a majority of low-carbon sheets, deformation takes place evenly along the whole length of the test specimen, until a certain phase of the process where the loss of stability occurs, which is manifested through the local narrowing and thinning of the specimen (Fig. 1).
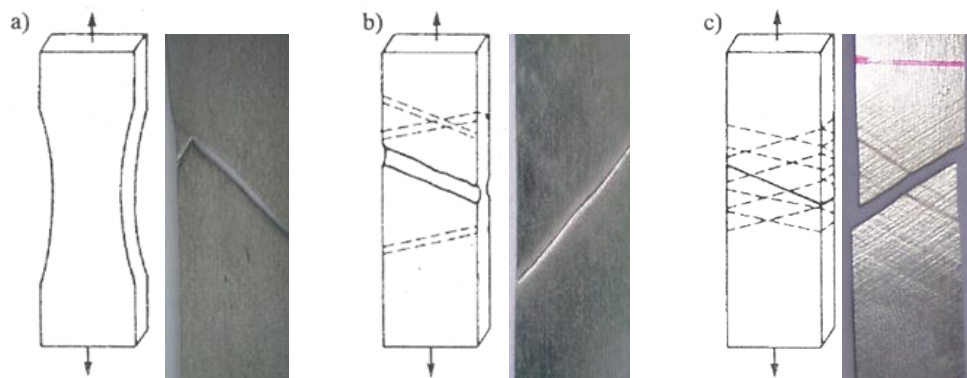

Fig. 1. Ways of loss of stability of the test specimen: a) without localization of deformation, b) Marciniak model, c) several slip lines
(European Standard EN 10202:2001, 2001)

Emil Spišák, Janka Majerníková, Emília Duľová, Ľuboš Kaščák
Analysis of Plastic Deformation of Double Reduced Sheets

The reduction of width and thickness of the material continues until another type of the stability loss in the area appears. The loss of stability of the plate appears as a local change, there is a change of its thickness along the certain line. This type of deformation can be observed as a local thinning visible on the surface of the specimen (Fig. 1b). Its width depends on the thickness of the sheet. The local thinning continues until the slip strips appear across its whole length. When the loss of stability of the material occurs, local deformation appears in the form of shear bands (Fig. 1c) at the moment when the load reaches the maximum. Methods for localization of deformation as well as the conditions of the loss of stability were described by many authors (Hill, 1952; Marciniak, 1978; Swift, 1952).

Generally, there are three basic models of the loss of stability, which are accepted (Fig. 1), including a model of the diffusion thinning (Swift, 1952), the localized thinning (Hill, 1952) and a model of the initial inhomogeneity in the material – Fig. 1b (Marciniak, 1978).

Deformation proceeds at a decreased stress level, known as the lower yield stress, but it is inhomogeneous. The specimen is divided into the regions where the strain is relatively high (Lüders strain) and the regions which are still elastic. The distinct plateau in the stress-strain curve is characterized by the propagation of Lüders bands. The propagation of Lüders bands is influenced by many factors including crystal structure, grain size, composition and microstructure, shape and stiffness of the testing specimen, strain rate and the type of loading. Experimental study of local deformation has been described previously by the authors (Zhang and Jiang, 2004). It was found out that the strain at the beginning of Lüders band is lower than the total strain. Generally, this phenomenon is important in the process of material deformation (Zhang and Jiang, 2004a, b).

3. MATERIAL FOR THE EXPERIMENTAL RESEARCH

Tinplate TH 415 CA with the thickness of 0.18 mm was used for the experiment. The tinplate had been processed by double reduction and continuous annealing. The specimens were taken in the rolling direction (0°) and the direction perpendicular to the rolling direction (90°). The chemical composition of the material is given in Tab. 1.

Tab. 1. Chemical composition of the material TH 415 CA expressed in [wt. %]

Fe	C	Si	Mn	P	S	Cu	Al
99.52	0.075	0.022	0.130	0.014	<0.002	0.030	0.065
Cr	**Mo**	**Ni**	**V**	**Ti**	**Nb**	**Co**	**W**
0.009	0.013	0.005	0.009	<0.002	0.018	0.036	0.048

In order to identify the mechanical properties of the tested material, uniaxial tensile test (Fig. 2a) and hydraulic biaxial tensile test (Fig. 2b - Bulge test) were conducted. The plastic deformation is observed in particular areas on the specimens. The specimens were difficult to evaluate because numerous damages occurred out of the measured section of specimens. Besides the deformation in the observed area, there occurred damage in other locations, with cracks of different shapes; however, major part of the specimen remained without plastic deformation, as illustrated in Fig. 3. Mechanical properties of the tested material TH 415 CA obtained from uniaxial tensile test are shown in the Tab. 2.

a)

b)
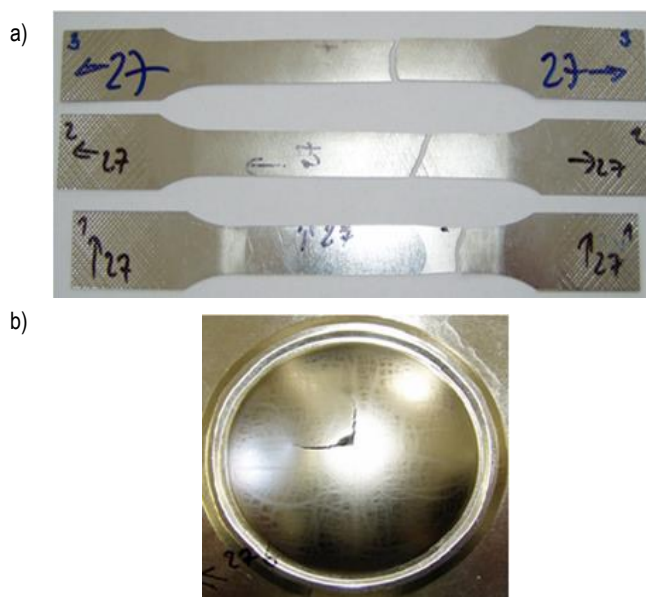
Fig. 2. Specimen No. 27: a) uniaxial tensile test, b) hydraulic biaxial tensile test

a) b)
c)
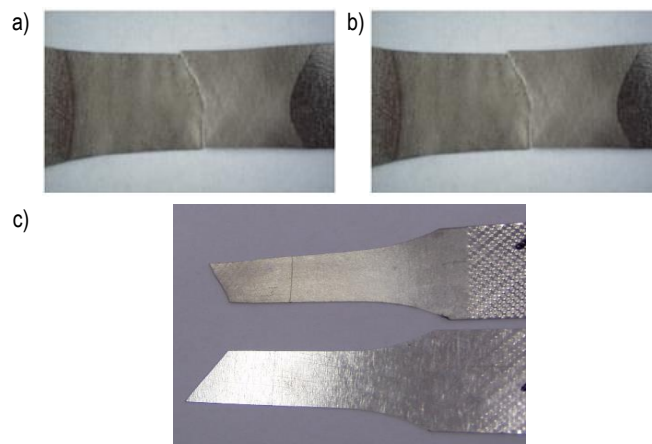
Fig. 3. Detail of plastic undeformed parts of specimen after uniaxial tension test: a) local deformation with a fracture, b) local deformation without a fracture, c) fractured material after plastic deformation and without plastic deformation

Tab. 2. Mechanical properties of material obtained from uniaxial tensile test

Specimen number	$R_{p0,2}$ [MPa]	R_m [MPa]	A_{50} [%]
÷27 0°	**450.7**	**443**	**21.61**
÷27 90°	**504**	**499.7**	**1.89**

The specimen obtained from hydraulic biaxial test after failure is documented in Fig. 2b. Slip bands were clearly visible in the deformed area of specimens. Anisotropic properties obtained from this test are shown in Tab. 3.

Tab. 3. Mechanical properties of tested steel sheet obtained from hydraulic biaxial tensile test

Specimen number	$R_{p0,2}$ [MPa]	R_m [MPa]	A [%]	h_{dome} [mm]
÷27	**370**	**507. 3**	**12.59**	**17.7**

4. EXPERIMENTAL METHODS

Uniaxial tensile test was carried out on the TIRA test 2300. Test conditions and the shape of the specimen corresponded to standards STN EN 10002-1+AC1 and STN 42 0321.

Hydraulic biaxial tensile test was performed on the equipment for hydraulic bulging (Bulge test). The test plate is clamped between the bottom plate and die with a diameter of 80 mm. The blankholder prevents pulling material through the rib located in die. Fluid pressure is used for deformation and subsequent burst of the specimen. The plastic properties of the tested plate are identified from the height of the bulge and shape of the crack after the bulge is damaged. Hydraulic biaxial tensile tests are used for evaluation of parameters such as yield strength R_e, ultimate tensile strength R_m, total elongation of specimen A_{50} and the height of bulge h. Hydraulic bulge test was performed using six specimens of steel sheet TH 415CA with thickness 0.18 mm and size 130 mm x 130 mm.

Subsequently, metallographic observation of material structure was performed. Specimens were observed and evaluated using a GX 71 Olympus light microscope. Specimens were taken from deformed parts after uniaxial (Fig. 4) and hydraulic biaxial tensile tests (Fig. 5). Figs. 4 and 5 show areas marked with highlighted detail "C" for metallographic observation, which is shown in Figs. 6 and 7.
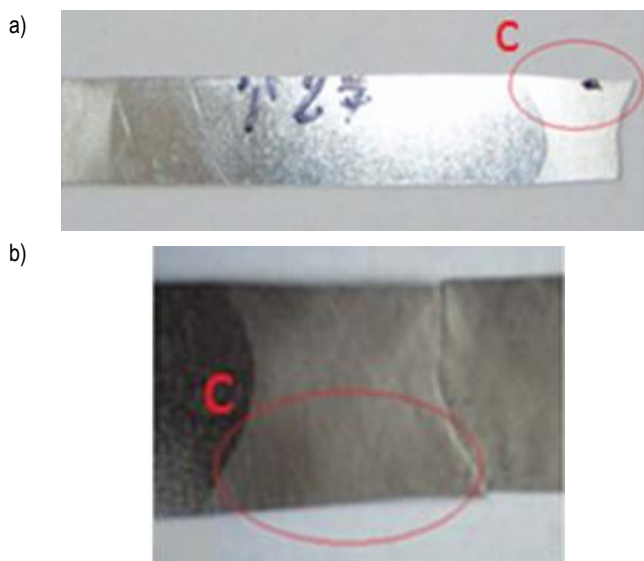
a)

b)

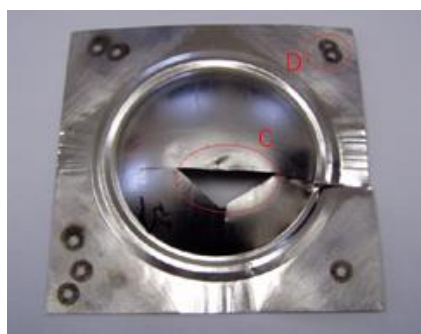**Fig. 4.** Specimen for metallographic observation: a) detail "C", b) after uniaxial tensile test

Fig. 5. Specimen for metallographic observation – detail "C" and for the analysis of the chemical composition of the material – detail "D" (hydraulic biaxial tensile test)

5. EXPERIMENTAL RESULTS AND THEIR ANALYSIS

Tinplate TH 415 CA was used for metallographic observation of the microstructure. After uniaxial tensile test in the 0° direction, the microstructure showed significantly elongated grains in the rolling direction, which is the result of the double reduction (Fig. 6a). The microstructure of the specimen taken in the 90° direction is characterized by uniform structure (Fig. 6b). The localization of deformation and fracture of specimens in the tensile test can be explained by Marciniak's theory, according to which the localization of deformation occurs in areas with a strong inhomogeneity of the material. Inhomogeneity of the material can cause changes in the surface micro-geometry; internal inhomogeneity of the material can cause a lot of surface defects. The depth of defects plays the main role in this process. Non-metallic inclusions – oxides were observed at these locations and at the coupling of the base material with deformation slivers. Their presence depends on the material conditions of annealing (Fig. 6a, b).

a)

b)
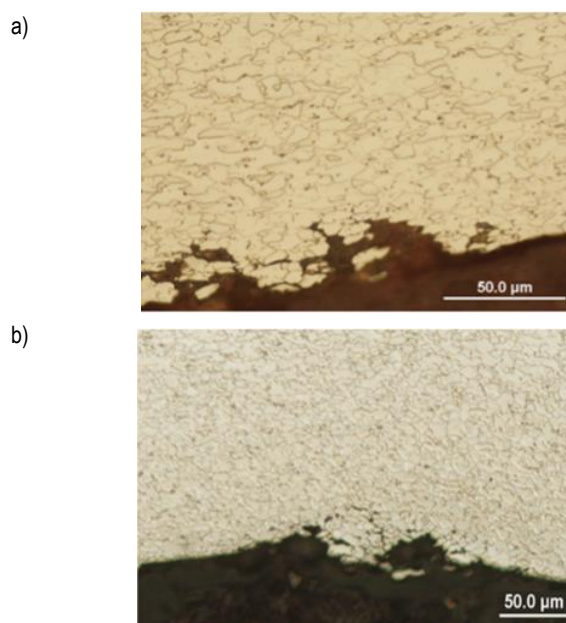
Fig. 6. Deformed material structure after uniaxial tensile test taken from place "C": a) rolling direction 0°, b) rolling direction 90°

The average value of elongation of tinplate in the 0° direction was 2%, and it reached 22% in the 90° direction. Significant difference was observed in the mechanical properties of specimen taken in the 0° and 90° direction, particularly in their non-deformed parts. The value of elongation difference observed in most cases was up to 100 %.
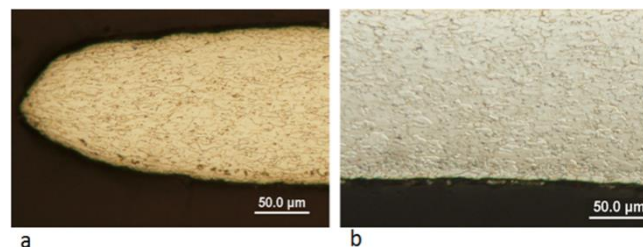
Fig. 7. Deformed material structure after hydraulic biaxial tensile test test taken from place "C" in rolling direction 0°: a) area of fracture, b) base material

To determine the properties of tinplate, hydraulic biaxial tensile test appeared to be preferable. The average value of elongation of this material was 13%. The microstructure of the deformed material was also characterized by a uniform structure in the failure area, which was typically plastic with a significant narrowing (Fig. 7a, b). Breakage of the specimen is initiated at a particular location when the slip bands and thinning occur. They are not able to resist the increasing tension, which results in the failure of material.

6. CONCLUSIONS

Firstly, this paper described the causes and consequences of the loss of stability and violations of tinplate in uniaxial and biaxial tensile loading. Secondly, it analysed the deformation and loss of stability in individual tests. The metallographic structure of material was observed, which served for the analysis of the structure and mechanism of plastic deformation. At the very beginning of plastic deformation in the uniaxial tensile test, the slip lines are generated; these exist in areas with inner inclusions in material. In these spots, as tension force increases, deformation is localized in the area of slip plains without spreading plastic deformation along the whole length of test specimen. The test specimen disrupts in this spot.

In case of hydraulic biaxial tensile test, the difference between yield strength Rp0.2 and Rm is higher. Plastic deformation occurs in various directions (suitably oriented grains), thus the difference is not localized in its slip plain.

Based on the results we can conclude that uniaxial tensile test does not provide objective information regarding the plastic properties of material. Hydraulic biaxial tensile test is more suitable for DR tinplate thinner than 0.18 mm, as it provides more objective information on plastic properties of DR tinplate.

REFERENCES

1. **Aerts T., Dimogerontakis Th., DeGraeve I., Fransaer J., Terryn H.** (2007), *nfluence of the anodizing temperature on the porosity and the mechanical properties of the porous anodic oxide film*, *Surface and Coatings Technology*, 201(16-17), 7310–7317.
2. **European Standard EN 10202:2001** (2001) *Cold reduced tin mill products-electrolytic tinplate and electrolytic chromium/Cr oxide coated steel*, The European Standard Publications, Brussels.
3. **Gburík R., Černík M., Legatt R., Vranec P.** (2015), *Crystallographic texture of light tinplate coatings made in various electrolytes*, *IOP Conference Series: Materials Science and Engineering*, 82(1), 4.
4. **Hill R.** (1952), On discontinuous plastic states with special reference to localized necking in thin sheets, *Journal of the Mechanics and Physics of Solids*, 1, 19-30.
5. **Kvačkaj T., Bacsó J. , Bidulská J. , Lupták M., Pokorný I., Kvačkaj M., Vlado, M.** (2010), *Influence of cryo and classic rolling conditions on processing parameters of C-Si steel*, *Acta Metallurgica Slovaca*, 16(4), 268-276
6. **Kvačkaj T., Bidulská J.** (2014), *From micro to nano scale structure by plastic deformations*, Materials Science Forum, 783-786, 842-847.
7. **Makarov P.V., Schmauder S., Cherepanov O.I., Smolin I.Yu., Romanova V.A., Balokhonov R.R., Saraev D.Yu., Soppa E., Kizler P., Fischer G., Hu S., Ludwig M.** (2004), *Simulation of elastic–plastic deformation and fracture of materials at micro-, meso- and macrolevels*, *Theoretical and Applied Fracture Mechanics,* 37(1-3), 183-244.
8. **Makarov P.V., Schmauder S., Cherapanov I.O., Smolin Yu.I., Romanova A.V., Balokhonov R.R., Saraev D.Yu., Soppa E., Kizler P., Fischer G., Hu S., Ludwig M.** (2001), Simulation of elastic-plastic deformation and fracture of materials at micro, meso- and macrolevels, *Theoretical and Applied Fracture Mechanics*, 37, 183-244**.**
9. **Marciniak Z.** (1978), *Mechanics of sheet metal forming*, Plenum Press, New York.
10. **Mihaliková M., Ambriško L., Pešek L.** (2011), *Videoextensometric measuring of deformation processes in automotive steel sheets at two strain rate levels*, *Kovové materiály*, 49(2), 137-141.
11. **Slota J., Spišák E., Jurčišin M.** (2014), *Local strain hardening and non-uniformity of plastic strain of tinplate*, *Key Engineering Materials*, 606, 23-26.
12. **Spišák E., Majerníková J.** (2014), The Loss of Plastic Properties Stability of Thin Tinplates and Its Influence on Change of Corrosive Resistance, *Applied Mechanics and Materials: Novel Trends in Production Devices and Systems 2*, 693, 340-345.
13. **Spišák E., Džupon M., Majerníková J., Spišáková Duľová E.** (2015), Failure of coatings of tinplates, *Acta Metallurgica Slovaca*, 21(3),213-219
14. **Spišák E., Majerníková J.** (2014a), *The Loss of Plastic Properties Stability of Thin Tinplates and Its Influence on Change of Corrosive Resistance*, Applied Mechanics and Materials, 693, 340-345.
15. **Spišák E., Slota J., Majerníková J.** (2011), The analysis of plastic strain of single and double reduced tinplates, *Chem. Lett.*, 105, 485-487.
16. **Spišák E., Slota J., Majerníková J., Kaščák Ľ., Malega P.** (2012), Inhomogeneous plastic deformation of tinplates under uniaxial stress state, *Chem. Lett.*, 106, 537-540.
17. **Spišák E., Majerníková J.** (2012), *Analysis of variance of mechanical properties of sheets as the input parameters for simulation of processes*, *Acta Metallurgica Slovaca*, 18(2-3), 109-116.
18. **Spišák E., Majerníková J.** (2014b), The Loss of Plasticity Stability, *Applied Mechanics and Materials: Novel Trends in Production Devices and Systems 2*, 693, 346-351.
19. **Swift H.W.** (1952), Plastic instability under plane stress, *Journal of the Mechanics and Physics of Solids*, 1(1), 1-18.
20. **Yu H., Burgess I.W., Davison J.B., Plank R.J.** (2008), Journal of Constructional Steel Research, 64(5), 515-525.
21. **Zhang J., Jiang Y.** (2004a), A study of inhomogeneous plastic deformation of 1045 steel, *J. Eng. Mater. Technol.,* 126, 164-172.
22. **Zhang J., Jiang Y.** (2004b), Lüders bands propagation of 1045 steel under multiaxial stress state, *International Journal of Plasticity*, 21, 651-670.
23. **Zhang J., Jiang Y.A.** (2005), International Journal of Plasticity, 21(3), 651-670.

SURFACE LAYER PROPERTIES OF LOW-ALLOY HIGH-SPEED STEEL AFTER GRINDING

Jan JAWORSKI*, Tomasz TRZEPIECIŃSKI****

*Faculty of Mechanical Engineering and Aeronautics, Department of Manufacturing and Production Engineering,
Rzeszow University of Technology, Al. Powstańców Warszawy 12, 35-959 Rzeszów, Poland
**Faculty of Mechanical Engineering and Aeronautics, Department of Materials Forming and Processing,
Rzeszow University of Technology, Al. Powstańców Warszawy 12, 35-959 Rzeszów, Poland

jjktmiop@prz.edu.pl, tomtrz@prz.edu.pl

Abstract: Investigations of the surface layer characteristics of selected kinds of low-alloy high-speed steel after grinding were carried out. They were carried out on the flat-surface grinder with a 95A24K grinding wheel without cooling. The influence of grinding parameters was defined especially for: the quantity of secondary austenite, surface roughness, microhardness and grinding efficiency with a large range of grinding parameters: grinding depth 0.005–0.035 mm, lengthwise feed 2–6 m/min, without a cross-feed on the whole width of the sample. It was found that improvement of grinding properties of low-alloy high-speed steels is possible by efficient selection of their chemical composition. The value of the grinding efficiency is conditioned by grinding forces, whose value has an impact on the grinding temperature. To ensure high quality of the tool surface layer (i.e. a smaller amount of secondary austenite, lack of wheel burn and micro-cracks) in the case of sharpening of tools made of low-alloy high-speed steel, the grinding temperature should be as low as possible.

Key words: Grinding, High-Speed Steel, Microhardness, Secondary Austenite, Surface Roughness

1. INTRODUCTION

Grinding and sharpening are the final operations in the manufacturing of cutting tools. Under the influence of these operations, in the tool surface layer occur e.g. structural changes, surface stresses, plastic deformations and others (Józwik and Pietras, 2013). These phenomena determine the quality of the tools to a great extent, which mainly depends on the state of the surface layer (Jaworski and Trzepieciński, 2016b; Li and Axinte, 2016; Uhlmann et al., 2016). Grinding is an integral process composed of several simultaneous sub-processes, and chemical additives can affect these sub-processes. The past reports on the effect of physico-chemical parameters of the environment on mechanical properties and grindability of materials were reviewed by El-Shall (1984). The degree of the effect of grinding on the properties of high-speed steel depends on such factors as the abrasive, the workpiece, the type and parameters of grinding, coolant, etc. (Ding et al., 2015). For example, increasing the speed of grinding or lengthwise feed leads to grinding burns on the surface layer of the workpiece or tool made of steel with low grindability. The mathematical model relating the heat transfer between the grinding wheel, fluid, and the workpiece is presented by Gu et al. (2004). Coolant fluids have been used in grinding processes to reduce workpiece temperature and decrease the risk of thermal damage (Tawakoli et al., 2011) In addition, thanks to their lubricant properties fluids serve to enhance process performances (Torrance, 1978).

Many studies have shown that the formation of grinding burns denotes the formation of a clear layer having an austenitic-martensitic microstructure on the hardened steel surface, due to secondary hardening (El-Rakayby and Mills, 2013; Romano et al., 2006; Zhou et al., 2016). This shows that the temperature in the grinding zone exceeds the transition temperature $Fe_\alpha - Fe_\gamma$.

In grinding, the literature generally distinguishes two transient temperatures: a background temperature rise and a local temperature rise (Lefebvre et al., 2012). The background temperature results from the cumulative effect of all local heat sources on the ground surface. The background temperature damages the workpiece subsurface, whilst the temperature flashes and heat generated at the grain/workpiece interface increase the wear rate (Lefebvre et al., 2008; 2012). The grain–workpiece interactions at the local level and the wheel–workpiece interactions at the global level are studied by Hou and Komanduri (2004). The first attempt to correlate actual grinding temperatures with structural metallurgical changes in the workpiece was reported by Littman and Wulf (1955). The heat is primarily carried away to the machined part, because the cross-section and volume of the chip are very small, and the grinding wheel hardly conducts heat. Stresses are formed in the surface layer under the influence of heating and phase transformations. The magnitude of stresses may even exceed the allowable stress of the workpiece, which can lead to the formation of micro-cracks on the surface of the workpiece. Thermal damage is one of the main factors which affects workpiece quality, so it is especially important to understand the underlying factors which affect the grinding temperatures. The use of superabrasive grinding wheels is known to reduce the risk of thermal damage of the workpiece (Rowe et al., 1995). A comprehensive overview of thermal analyses for grinding processes and the effect of grinding temperatures on thermal damage is provided by Malkin and Guo (2007). The changes in the microstructure of the steel as a result of grinding depend on its chemical composition and parameters of the grinding (Abidi et al., 2013; Jaworski and Trzepieciński, 2016b). These changes can be divided into two categories:

− changes related to the establishment of microstructure of secondary hardening with tempering; and

– changes related to the establishment of microstructure with different degrees of tempering.

On the whole, in the surface layer, one changed zone of secondary hardening or secondary tempering, or several zones can be created i.e. secondary hardening, transient and secondary tempering (Bonek, 2014; Moravcik et al., 2012). During the secondary hardening, a clear outer surface layer consisting of a large amount of austenite, usually ~10–70%, is normally formed. Austenite is formed at high intense heat, is very stable, and hardly decomposes upon cooling. However, the decomposition of high-speed steels occurs from 400–450°C during the heating. Walton et al. (2006) found that the effect of the heating rate due to the grinding conditions have a significant influence on the A3 austenitic transition temperature. A review of early works concerned on hardening of alloy steel surfaces by grinding was done by Torrance (1978).

Because all of the mentioned changes in the surface layer when sharpening of tools directly affect the durability of the tools, they can be used to assess the grindability of high-speed steel. Steel grindability can be interpreted as a comprehensive parameter that allows one to characterise the ability of steel to provide the required properties of the surface layer under certain conditions (Urbaniak, 2006). For grindability assessment, a knowledge of the efficiency of the grinding process of a particular grade of steel is also important. The grindability strongly depends on the tendency of grinding wheels to blunt. Therefore, to determine the grindability, first we must examine all the physical processes that occur during the grinding. The characteristics of ground surface layer depend on the depth of microhardness variation, depth of occurrence of structural modifications in the surface layer, micro-cracks forming and surface roughness (Foeckerer et al., 2013; Jaworski and Trzepieciński, 2016a; Oliveira et al., 2009; Weiss et al., 2015; Zhang et al., 2015). The grindability of high speed steel in terms of specific grinding energy versus undeformed chip thickness and maximum temperature rise versus specific material removal rate is presented by Krajnik et al. (2011).

Wear and tear of cutting and grinding tools is one of the most important characteristics that define the accuracy of technological system of parts machining (Arsecularatne et al., 2006; Jaworski et al., 2014; Jaworski et al., 2016). Recognition of the machining properties and defining the tool operational reliability as one of the elements of that system is realised through the help of experimental data about wear and tear of a knife-edge, depending on machining time or path (Kulesza et al., 2012).

Here, the measurements of parameters of the surface layer and grinding efficiency of selected kinds of low-alloy high-speed steel were carried out. The aim of the investigations is to find the effect of grinding depth and lengthwise feed on such grinding parameters as the quantity of secondary austenite, surface roughness, microhardness, and grinding efficiency.

2. MATERIALS AND METHOD

The cubicoid samples have dimensions of 6 x 6 x 65 mm. The heat treatment was carried out according to the recommendation of suitable standards. The selected physical-mechanical properties of the tested steels are shown in Tab. 1.

The investigations were carried out on the flat-surface grinder with a disk-type grinding wheel 95A24K without cooling. The influence of the grinding parameters was defined especially for: quantity of secondary austenite, roughness of surface, microhard-

ness and coefficient of grinding with a large range of grinding parameters: v_c = 20 m/s, a_p = 0.005–0.035 mm, v_f = 2–6 m/min, without cross-feed on the whole width of sample. After each study, the disk-type grinding wheel was dressed by diamond dresser. The temperature was measured using a half-artificial thermocouple according to methodology, which is known. The force was measured using a dynamometer, whereas the roughness of the surface was measured using Surtronic 3+ profilograph and the microhardness using the Brivisor KL2 microhardness tester on oblique cuts. The surface roughness is calculated by choosing cut-off length of 0.8 mm, according to the recommendation of ISO 3274:1998 and ISO 4288:1998 standards. The amount of secondary austenite both on the surface and in depth was determined using a Philips device.

3. RESULTS AND DISCUSSION

3.1. Microhardness

To increase the efficiency of sharpening by means of increasing its parameters, it is better to increase lengthwise feed than the grinding depth. The microhardness of the surface layer in relation to the grinding depth was measured on the skew-polished sections. The microhardness of HS3-1-1 steel has undergone considerable modification together with an increase of grinding depth (Fig. 1). The decrease of microhardness can be observed at a_p = 0.015 mm and increase of microhardness at a_p = 0.025–0.035 mm. The decrease of hardness for HS6-5-2 steel is not observed at all cutting depths and decrease of hardness at a_p = 0.035 mm is less substantial (Fig. 2). Results confirm higher propensity to structural modifications for HS3-1-1 steel during grinding. At the distance from the surface layer d_s = 0.02 mm for both steels the change of microhardness value is not observed.
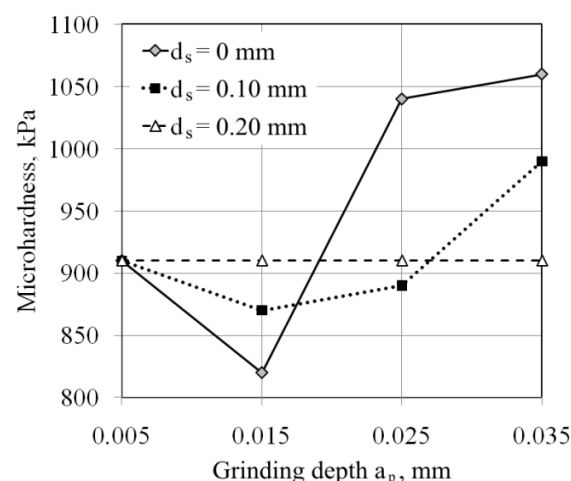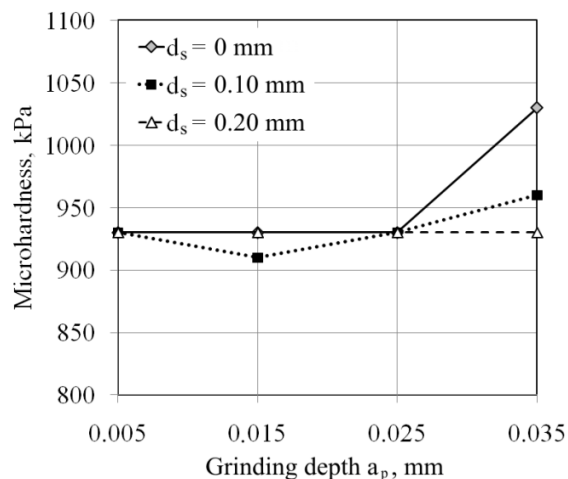

Fig. 1. Effect of grinding depth on microhardness of HS3-1-1 steel
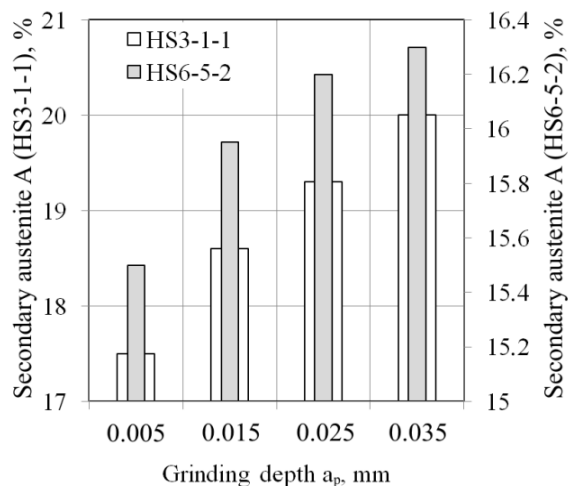
3.2. Secondary austenite

In many investigations (e.g., Bonek, 2014; Sinopalnikov and Grigoriew, 2003) the amount of secondary austenite is a main criterion in the evaluation of surface layer quality during tools sharpening.

Tab. 1. Low-alloy high-speed steel grades – chemical constitution and physical-mechanical properties

| Steel grade	Chemical constitution in % wt.						Physical-mechanical properties			
	C	W	Mo	Cr	V	Si	Hardness HRC	Bending strength R_g, MPa	Impact resistance, J/m²	Hardening temperature, ºC
HS3-3-3	1.00	2.98	2.83	4.27	2.30	-	64	3400÷3800	$3.2 \cdot 10^5 \div 4 \cdot 10^5$	1180÷1210
HS2-5-2	0.99	1.67	4.79	3.78	1.15	-	64	3000÷3400	$4 \cdot 10^5 \div 4.5 \cdot 10^5$	1080÷1170
HS3-1-1	1.11	3.35	1.15	4.65	1.75	2.05	63÷68	3000÷3600	$4.6 \cdot 10^5$	1080÷1170
HS6-5-2	0.82	5.55	5.13	4.27	2.06	-	64	3200÷3600	$4.8 \cdot 10^5$	1200÷1230

Fig. 2. Effect of grinding depth on microhardness of HS6-5-2 steel

The effect of grinding depth in a range of 0.005–0.035 mm on the amount of secondary austenite for HS3-1-1 and HS6-5-2 steels is presented in Fig. 3. The amount of secondary austenite for HS3-1-1 steel is larger than for HS6-5-2 steel and increases with increasing grinding depth.

Fig. 3. The influence of grinding depth on the amount of secondary austenite

The influence of lengthwise feed on the amount of secondary austenite for both on the surface layer and at the depth of 0.01 mm is shown in Fig. 4. The amount of secondary austenite at the depth of 0.01 mm deceases with increasing lengthwise feed; however at a lengthwise feed v_f = 6 m/min, the amount of austenite is almost imperceptible. With lengthwise feed increase, austen-

ite is located in more thin layers, which is proved by decreasing its content at a depth of 0.01 mm, although its amount is considerably higher on the surface layer (Fig. 4). The impact of grinding depth on the amount of austenite on the surface layer is presented more distinctly.
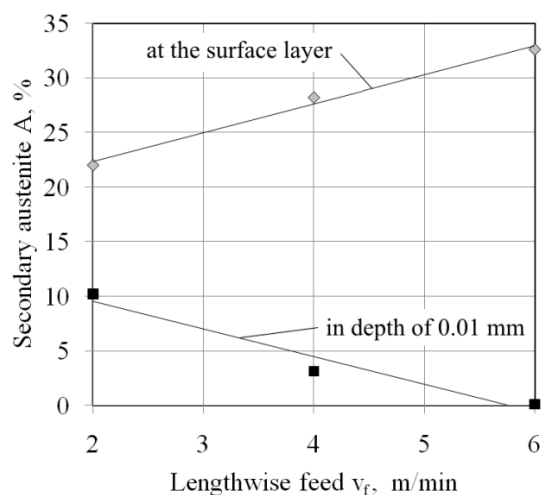
Fig. 4. The influence of lengthwise feed on the amount of secondary austenite for HS6-5-2 high-speed steel

3.3. Surface roughness

Results of the measurement of the Ra parameter are presented in Fig. 5 and Tab. 2. Substantial differences of surface finish for selected steel grades are not observed.
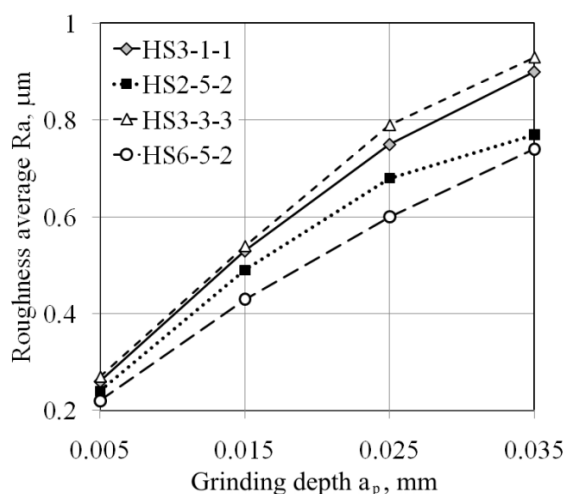
Fig. 5. Effect of grinding depth on the Ra parameter value

The value of Ra parameter increases together with an increase of grinding depth (Fig. 2) and lengthwise feed (Tab. 2), for all steels used. Furthermore, the quite linear relation between the roughness average Ra and the grinding depth is observed (Fig. 5). Differences in the surface finish do not have an impact on the machinability of tools.

Tab. 2. Effect of lengthwise feed v_f on the roughness of the average Ra value

Steel grade	v_f, m/min	Ra, µm
HS3-1-1	4	0.67
	6	0.80
HS3-3-3	4	0.63
	6	0.77
HS6-5-2	4	0.71
	6	0.86
HS2-5-2	4	0.63
	6	0.74

3.4. Grinding ratio

The value of grinding efficiency can be, to a certain degree, the characteristic of efficiency and quality of low-alloy high-speed steel grinding process. The value of this parameter is evaluated using (Jaworski, 2002):

$$K = Q_m/P_y \qquad (1)$$

where: Q_m – the amount of material that is removed, P_y – inverted grinding force.

The values of grinding efficiency are shown in Fig. 6. Low-alloy high-speed steel has poorer grinding properties than HS6-5-2 steel, with the exception of HS2-5-2, where that ratio is slightly higher. Other investigations of the grinding efficiency value (Masłow, 1974) have shown that in the case of grinding of HS3-1-1 steel using a CBN grinding wheel, the grinding efficiency value is 2.5 times greater than in the case of grinding using a corundum grinding wheel. Furthermore, in the case of grinding using the corundum wheel, the value of the grinding efficiency is the same for each grade of low-alloy high-speed steel.
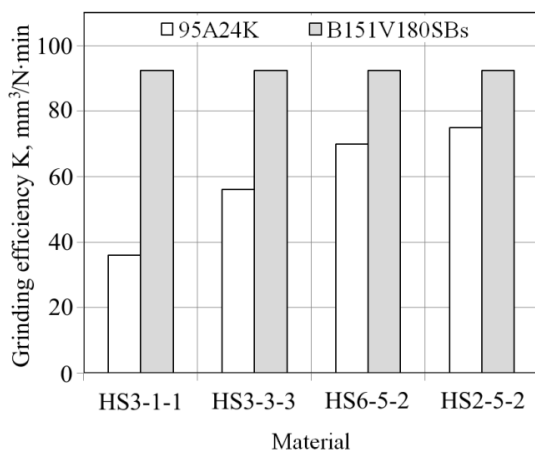

Fig. 6. The grinding efficiency for selected grades of low-alloy high-speed steels during grinding using corundum (B151V180SBs) and CBN (95A24K) wheels at v_c = 20 m/s, v_f = 2 m/min and a_p = 0.005 mm

Because there is a direct relationship between the grinding temperature and the quality of the surface layer, to improve the grinding efficiency it is necessary to create the conditions allowing us to reduce cutting forces and the temperature in the surface layer of high-speed steel. This can be achieved by using cutting-tool lubricants (Brinksmeier, 1999). However, in industrial conditions, tool sharpening is usually carried out without the use of cutting-tool lubricants and therefore more efficient in this case is the use of cubic boron nitride (CBN) grinding wheels (Sallem and Hamdi, 2015).

4. CONCLUSIONS

We have shown that the characteristics of ground surface layer depend on the depth of microhardness variation, the depth of occurrence of structural modifications in the surface layer, and the amount of secondary austenite and process parameters. To ensure a lack of burn and micro-cracks during the sharpening of tools made of low-alloy high-speed steel, the grinding temperature should be maintained as low as possible. To achieve this aim, the following criteria must be met: use of a borazon abrasive disk, decreasing the sharpening parameters, or selection of optimal grinding fluids for the specific conditions. To increase the efficiency of sharpening by means of increasing its parameters, it is better to increase the lengthwise feed than the grinding depth.

REFERENCES

1. **Abidi H., Rezaei S.M., Sarhan A.A.D.** (2013), Analitycal modeling of grinding wheel loading phenomena, *International Journal of Advanced Manufacturing Technology*, 68(1-4), 473-485.
2. **Arsecularatne J.A., Zhang L.C., Montross C.** (2006), Wear and tool life of tungsten carbide, PCBN and PCD cutting tools, *International Journal of Machine Tools and Manufacture*, 46(5), 482-491.
3. **Bonek M.** (2014), The investigation of microstructures and properties of high speed steel HS6-5-2-5 after laser alloying, *Archives of Metallurgy and Materials*, 59, 1647-1651.
4. **Brinksmeier E., Heinzel C., Wittmann M.** (1999), Friction, cooling and lubrication in grinding, *CIRP Annals - Manufacturing Technology*, 48(2), 581-598.
5. **Ding Z., Li B., Liang S.Y.** (2015), Phase transformations and residual stress of Maraging C250 steel during grinding, *Materials Letters*, 154, 37-39.
6. **El-Rakayby A.M., Mills, B.** (2013), On the microstructure and mechanical properties of high-speed steels, *Journal of Materials Science*, 23(12), 4340-4344.
7. **El-Shall H.** (1984), Physico-chemical asects of grinding: a review of use of additives, *Powder Technology*, 38, 275-293.
8. **Foeckerer T., Zaeh M.F., Zhang O.B.** (2013), A three-dimensional analytical model to predict the thermo-metallurgical effects within the surface layer during grinding and grind-hardening, *International Journal of Heat and Mass Transfer*, 56(1–2), 223-237.
9. **Gu R.J., Shillor M., Barber G.C., Jen T.** (2004), Thermal analysis of the grinding process, *Mathematical and Computer Modelling*, 39(9-10), 991-1003.
10. **Hou Z.B., Komanduri R.** (2004), On the mechanics of the grining process, Part II—thermal analysis of the fine grinding, *International Journal of Machine Tools and Manufacture*, 44(2-3), 247-270.
11. **Jaworski J., Kluz R., Trzepieciński T.** (2014), The influence of machining parameters on the place of formation and intensity of the wear process of drills, *Tribologia*, 45(3), 81-90 (in Polish).

12. **Jaworski J., Kluz R., Trzepieciński T.** (2016), Operational tests of wear dynamics of drills made of low-alloy high-speed HS2-5-1 steel, *Eksploatacja i Niezawodnosc - Maintenance and Reliability*, 18(2), 271-277.

13. **Jaworski J., Trzepieciński T.** (2016a), Grindability of selected grades of low-alloy high-speed steel, *Advances in Science and Technology Research Journal*, 10(31), 222-228.

14. **Jaworski J., Trzepieciński T.** (2016b), Research on durability of the turning tools made of low-alloy high-speed steels, *Kovové Materialy – Metallic Materials*, 54(1), 17-25.

15. **Józwik J., Pietras P.** (2013), Investigation and assessment of occupational risk of the metal cutting machine tool stand, *Advances in Science and Technology Research Journal*, 7(20), 47-54.

16. **Krajnik P., Drazumeric R., Badger J., Kopač J., Nicolescu C.M**. (2011), Particularities of grinding high speed steel punching tools, *Advanced Materials Research*, 325, 177-182.

17. **Kulesza E., Dąbrowski J.R., Sidun J., Neyman A., Mizera J.** (2012), Freeting wear of materials - methodological aspects of research, *Acta Mechanica et Automatica*, 6(3), 58-61.

18. **Lefebvre A., Lanzetta F., Lipinski P., Torrance A.A.** (2012), Measurement of grinding temperatures using a foil/workpiece thermocouple, *International Journal of Machine Tools and Manufacture*, 58, 1-10.

19. **Lefebvre A., Lipinski P., Vieville P., Lescalier C**. (2008), Experimental analysis of temperature in grinding at the global and local scales, *Machining Science and Technology*, 12(1), 1-14.

20. **Li H.N., Axinte D.** (2016), Textured grinding wheels: A review, *International Journal of Machine Tools and Manufacture*, 109, 8-35.

21. **Littman, W. E., Wulff, J.** (1955), The influence of the grinding process on the structure of hardened steels, *Transactions of the American Society for Metals*, 47, 692-714.

22. **Malkin S., Guo C.** (2007), Thermal analysis of grinding, *CIRP Annals - Manufacturing Technology*, 56(2), 760-782.

23. **Masłow E.N.** (1974), *Theory of material polishing*, Maschinostrojenie, Moscow.

24. **Moravcik R., Stefanikova M., Cicka R., Caplovic L., Kocurova K., Sturm R.** (2012), Phase transformations in high alloy cold work tool steel, *Strojniski Vjesnik - Journal of Mechanical Engineering*, 58(12), 709-715.

25. **Oliveira J.F.G., Silva E.J., Guo C., Hashimoto F.** (2009), Industrial challenges in grinding, *CIRP Annals - Manufacturing Technology*, 58(2), 663-680.

26. **Romano P., Velasco F.J., Torralba J.M., Candela N**. (2006), Processing of M2 powder metallurgy high-speed steel by 419(1-2), 1-7.

27. **Rowe W.B., Black S.C.E., Mills B.** (1995), Experimental investigation of heat transfer in grinding, *CIRP Annals – Manufacturing Technology*, 44(1), 329-332.

28. **Sallem H., Hamdi H.** (2015), Analysis of measured and predicted residual stresses induced by finish cylindrical grinding of high speed steel with CBN wheel, *Procedia CIRP*, 31, 381-386.

29. **Sinopalnikow W.A., Grigoriew S.N.** (2003), *Reliability and diagnosis of technological systems,* MGU Stankin, Moscow.

30. **Tawakoli T., Hadad M., Sadeghi M.H., Daneshi A., Sadeghi B.** (2011), Minimum quantity lubrication in grinding: effects of abrasive and coolant–lubricant, *Journal of Cleaner Production*, 19(17–18), 2088-2099.

31. **Torrance A.A**. (1978), Metallurgical effects associated with grinding, *Proceedings of 19th Machine Tool Design and Research Conference*, Manchester, England, 637-644.

32. **Uhlmann E., Lypovka P., Hochschild L., Schröer N.** (2016), Influence of rail grinding process parameters on rail surface roughness and surface layer hardness, *Wear*, 366-367, 287-293.

33. **Urbaniak M.** (2006), Effect of the conditioning of CBN wheels on the technological results of HS6-5-2 steel grinding, *Archives of Civil and Mechanical Engineering*, 6(2), 31-39.

34. **Walton I.M., Stephenson D.J., Baldwin A.** (2006), The measurement of grinding temperatures at high specific material removal rates, *International Journal of Machine Tools & Manufacture*, 46, 1617-1625.

35. **Weiss B., Lefebvre A., Sinot O., Marquer M., Tidu A.** (2015), Effect of grinding on the sub-surface and surface of electrodeposited chromium and steel substrate, *Surface and Coatings Technology*, 272, 165-175.

36. **Zhang D., Li C., Jia D., Zhang Y., Zhang X.** (2015), Specific grinding energy and surface roughness of nanoparticle jet minimum quantity lubrication in grinding, *Chinese Journal of Aeronautics*, 28(2), 570-581.

37. **Zhou N., Peng R.L., Pettersson R.** (2016), Surface integrity of 2304 duplex stainless steel after different grinding operations, *Journal of Materials Processing Technolog*y, 229, 294-304.

IMPACT BEHAVIOUR OF SPOT-WELDED THIN-WALLED FRUSTA

Maria KOTEŁKO[*], Artur MOŁDAWA[*]

*Faculty of Mechanical Engineering, Department of Strength of Materials, Łódź University of Technology,
ul. Stefanowskiego 1/15, 90-924 Łódź, Poland

maria.kotelko@p.lodz.pl, artur.moldawa@dokt.p.lodz.pl

Abstract: In the paper the dynamic response of thin-walled, spot-welded prismatic frusta subjected to axial impact load is investigated. The parametric study into the influence of several parameters on the energy absorption capability, expressed by some crashworthiness indicators is performed, using Finite Element simulations. FE model is validated by experimental results of quasi-static and dynamic (impact) tests. Results of initial study concerning influence of spot welds are presented. Some conclusions are derived from the parametric study into the influence of frustum angle and wall thickness upon the energy absorption capability.

Key words: Thin-Walled Structures, Frusta, Impact, Energy Absorption

1. INTRODUCTION

Dynamic response of structures in the plastic range is a significant problem in the case of energy absorbers. Such a structural member converts totally or partially the kinetic energy into another form of energy. One of the possible design solutions is the conversion of the kinetic energy of impact into the energy of plastic deformation of a thin-walled metallic structural member. There are numerous types of energy absorbers of that kind cited in the literature (Alghamidi, 2001).

Thin-walled metal tubes are widely used as energy absorption systems in automotive industry due to their high energy absorption capability, easy to fabricate, relatively low price and sustainability at collapse.

A designer of any impact attenuation device must meet two main requirements. The initial collapse load (peak load) must not be too high in order to avoid unacceptably high impact velocities of the vehicle. On the other extreme, the main requirement is a possibly highest energy dissipation capacity, which may not be achieved if the collapse load of the impact device is too low. Thus, maximizing energy absorption and minimizing peak to mean force ratio by seeking for the optimal design of these components are of great significance. Many efforts have been made so far by several researchers to reduce the peak load at initial stage of the crushing process and simultaneously to increase energy absorption capacity in metal tubes, acting as energy absorbers.

One of the solutions are flaws or dents acting as triggers. A trigger may induce the most desirable crushing (collapse) mode, leading to higher energy absorption and mean to peak crushing force ratio. Ferdynus (Ferdynus and Kotełko, 2015) performed the static analysis of axially compressed square section tube with dents in the corners. A parametric study into an optimal dents situation and geometry with respect to the energy absorption capacity of tubes with dents subjected to axial impact was performed by the same author in Abbasi et al., (2015).

In last few years research was carried out into another solution, namely an application of multi-cornered thin-walled tubes as energy absorbing members. Abbasi et al. (2015) investigated crushing behavior and energy absorption of hexagonal, octagonal and 12-edge thin-walled columns. Reddy et al. (2015) continued to analyze the similar problem for 12-edge columns of different geometry. Ali et al. (2015) analyzed axial crushing of pentagonal and cross-shape thin-walled tubes. Another solution, bitubal energy absorber was investigated experimentally under quasi-static load by Sharifi et al. (2015).

An alternative solution are compressed thin-walled frusta (truncated circular cones or prisms) (Alghamdi, 2001), currently used as impact attenuation members in car structures, mainly due to the reduction of the peak crushing load in relation to parallelepiped. There are few published results, concerning this type of energy absorbing members. Very recently, Sarkabiri et al. (2015) published the results of multi-objective crashworthiness optimization of thin-walled conical groove tubes filled with polyurethane foam. They stated, that the conical angle reduces the peak crushing force, however it reduces also the absorbed energy.

2. SUBJECT AND OBJECTIVES OF THE ANALYSIS

The subject of investigation was a thin-walled prismatic frustum on square foundation of constant edge length a = 90 mm and height h =160 mm, shown in Fig. 1, subjected to axial, dynamic (impact) compressive load.

The first objective of the research was the investigation into an influence of spot welds on the crushing behavior of the frustum. Particularly, situation, number of spot welds and their diameter were taken into account in the analysis.

The main objective was the parametric study into the energy absorption capacity, ultimate load and mean crushing load of thin-walled prismatic frusta subjected to axial impact compressive

force. Particularly, the influence of the angle of inclination of the frustum wall was examined.
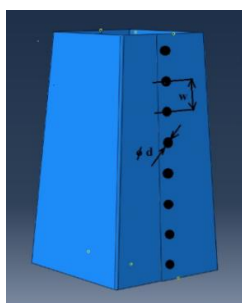

Fig. 1. Thin-walled spot welded frustum

There are several crashworthiness indicators (Jones, 2003) used to evaluate the crashworthiness of the energy absorbing structure (energy absorber). In the present analysis the following indicators are applied:

- energy absorption (EA);
- mean crushing force (MCF);
- crash load efficiency (CLE).

The typical crushing force – displacement curve for a thin-walled member subjected to axial impact is shown in Fig. 2.
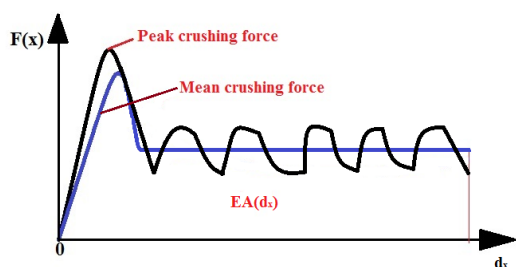

Fig. 2. Exemplary force – displacement curve for thin-walled member under axial impact

The energy absorbtion (EA) is calculated as an following integral:

$$EA(d_x) = \int_0^{d_x} F(x)dx \qquad (1)$$

where d_x is a crushing distance (see Fig. 2). The mean crushing force (MCF) for a given crushing deformation d_x is calculated as:

$$MCF = \frac{EA(d_x)}{d_x} \qquad (2)$$

Crash load efficiency is a mean crushing force (MCF) to peak crushing force (PCF – see Fig.2) ratio:

$$CLE = \frac{MCF}{PCF} \cdot 100\% \qquad (3)$$

In the parametric study the above mentioned indicators were determined in terms of the angle of inclination of the frustum and its wall thickness.

3. FINITE ELEMENT MODEL

Finite element calculations were carried out using commercial code Abaqus (Finite Element calculations carried out in Abaqus by CYFRONET AGH. MNiSW/IBM_BC_HS21/PŁódzka/013/2013)

and explicit dynamic analysis (Dassault Systems, 2013). An FE model of the column was created using 4-node shell elements S4R. A column model was situated between two rigid elements R3D4 (Fig. 3). Between upper and lower rigid elements and the column Tie links were applied. In the analysis the residual stresses coming from forming process of the metal sheet were taken into account. FE simulation of sheet folding process was performed. Then, the equivalent residua stresses obtained in this simulation were used as initial conditions in the explicit analysis of impact behaviour.
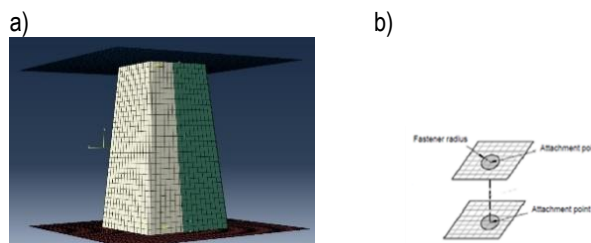
a)   b)

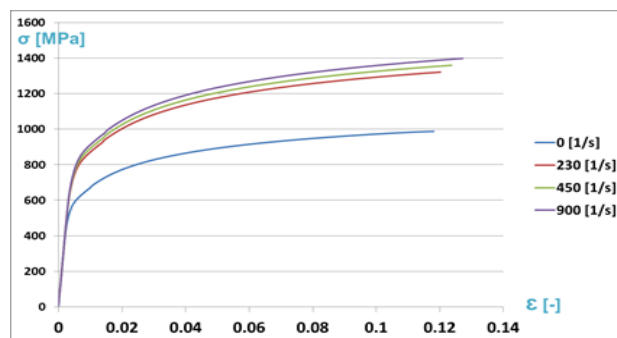**Fig. 3.** FE model: a)- frustum model, b)- spot weld model

Fig. 4. Material characteristics for varying strain rates

The spot welds were modelled using the rigid beam elements (Fig. 3b), situateted between two overlapping shell elements. Using the FASTENER elements nodes in the area of the spot weld were connected.

$$\bar{\sigma}(\dot{\bar{\varepsilon}}_{pl}, \bar{\varepsilon}_{pl}) = \sigma_0(\bar{\varepsilon}_{pl}) \cdot R(\dot{\bar{\varepsilon}}_{pl}) \qquad (4)$$

where: σ_0 – static (initial) yield stress, $\dot{\bar{\varepsilon}}_{pl}$ – equivalent plastic strain rate, R – yield stress ratio, $\bar{\varepsilon}_{pl}$ – equivalent plastic strain.

The rate-dependent elasto-plastic material model, taking into account the strain rate and strain hardening has been applied, the constitutive relation of which is given in (4). Equivalent stress and equivalent plastic strain were calculated using Huber-Mises yield criterion. The coefficient R was determined for subsequent equivalent plastic strain rates from tensile and compressive test curves (Fig.4) corresponding to subsequent strain rates. First, material parameters were determined in tensile and compressive static tests, in order to obtain a basic stress-strain curve. Then, on the basis of the data from literature (Kaczyński and Rusiński, 2014), curves corresponding to subsequent strain rates were determined. Afterwards, calibration of the material model was carried out using Abaqus program (Dassault Systems, 2013).

Calculations were carried out for high quality steel Dual Phase DP 800, with main strength parameters: yield stress σ_0 = 590 MPa,

Young modulus E = 210 GPa. From the same material columns (frusta) for experimental tests were fabricated.

4. EXPERIMENTAL VALIDATION OF FE RESULTS

Experimental verification of FE simulations was carried out both for quasi-static and dynamic (impact) load. Quasi-static tests were performed on the testing machine Instron, with the load velocity v_0 = 600 mm/min. The comparative load-shortening diagram and failure modes obtained theoretically and experimentally are shown in Fig. 5. The agreement of FE simulation results and experimental results of quasi-static tests was satisfactory.

Preliminary impact tests were performed on the drop-hammer rig, described in detailes in Kotełko et al., (2014). The comparative load-time diagram for the parallelepiped is shown in Fig. 6. The agreement in the case of impact load was also satisfactory, although the discrepancy of experimental and theoretical results was larger in the final stage of failure, which was partially caused by additional vibrations measured by the accelerometer (Kotełko et al., 2014).
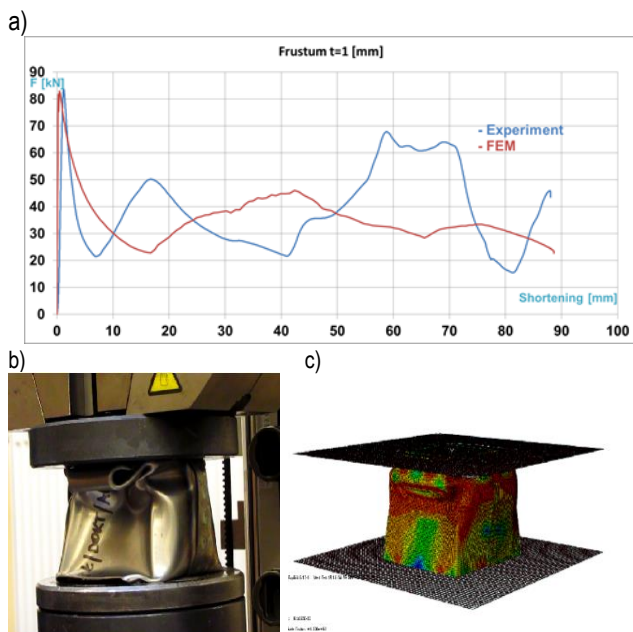
a)

b)   c)

Fig. 5: a) Load-shortening comparative diagram for quasi-dynamic load: frustum angle α = 5°, t = 1 mm, b) failure mode (experiment), c) – failure mode (FE simulation)
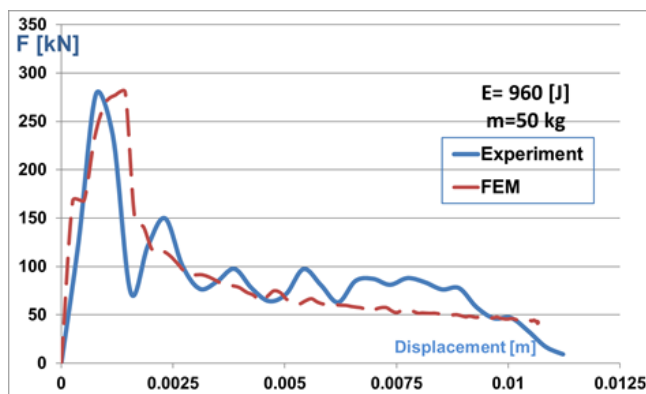

Fig. 6. Load-time comparative diagram for dynamic load for parallelepiped (α = 0°), t = 1, v_0 = 6.19 m/s

5. RESULTS OF PARAMETRIC STUDY

5.1. Influence of spot welds on the frusta crushing behavoiur

There are very few fragmented information about an influence of spot welding on the crushing behavior of thin-walled members subjected to axial impact (Rusiński et al., 2004).

In the present study the influence of the diameter and number of spot welds was investigated. Fig. 7 shows load-shortening diagrams for the frusta of angle 5° of the same number of spot welds, but of different diameter. In Fig.8. the influence of the number of spot welds of the same diameter is presented. The results of the study indicate, that that the diameter and number of spot welds do not influence the crushing behavior of frusta significantly.
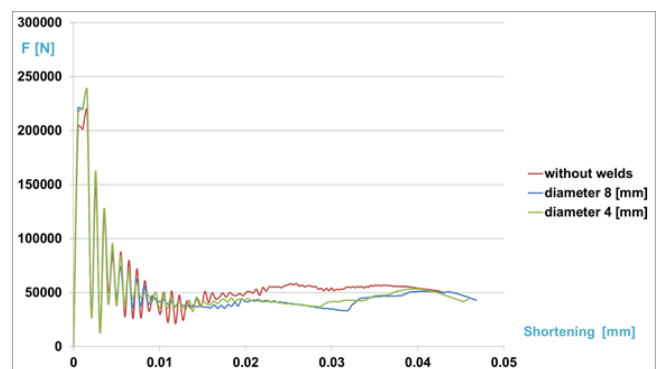
Fig. 7. Influence of spot weld diameter. Wall thickness t = 1 mm, α = 5˚, spot weld diameter d = 8 mm, d = 4 mm, n=8
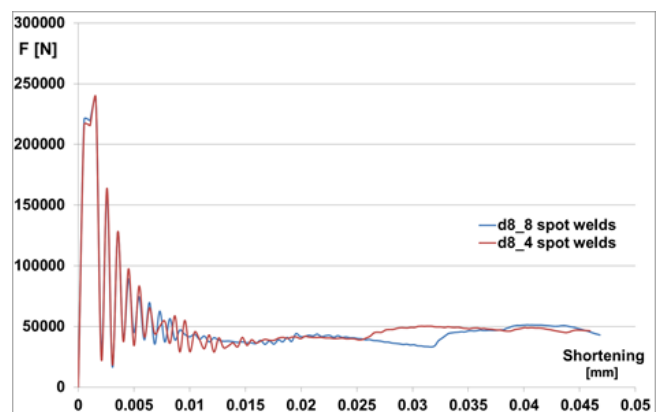
Fig. 8. Influence of spot weld diameter. Wall thickness t = 1 mm, α = 5˚, spot weld diameter d = 8 mm, n=8 and n=4

5.2. Parametric study of energy absorption capability

The parametric study was focused on the analysis into an optimal angle of frustum wall inclination (frustum angle) with respect to the energy absorbed, mean crusshing force (MCF) and crash load efficiency (CLF).

The subject of the parametric study was the frustum with 8 Spot welds of diameter d= 8 mm. Frusta of different wall thickness were examined.

Fig. 9. Influence of frustum angle on the crushing behaviour; wall thickness t = 0.8 mm

Fig. 10. Crash load effeciency (CLE)

Fig. 11. Energy absorption (EA)

Fig. 12. Energy absorption (EA) for wall thickness t = 0.8 mm

Fig. 9. shows load-shortening diagrams for the frustum of wall thickness t=0.8 mm and for different frustum angles. The structural crushing behaviour is similar for all frustum angles. However-

er, a significant decrease of peak crushing force with the increase of frustum angle is observed. In Fig. 10 CLE indicator in terms of frustum angle for different wall thickness values, which were examined, is presented. Fig.11 shows the energy absorption (EA) in terms of frustum angle for wall thickness values from t = 1 to t = 1.8. Similar diagram for one wall thickness t = 0.8 mm is presented in F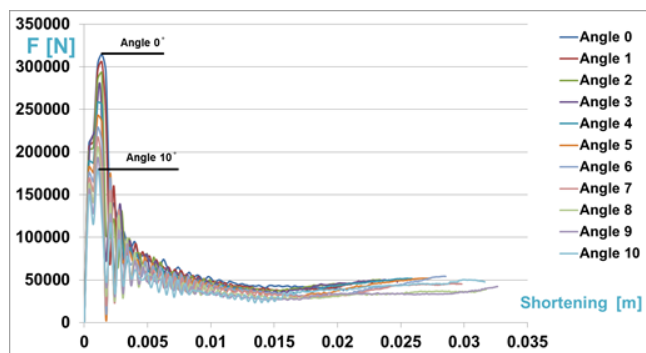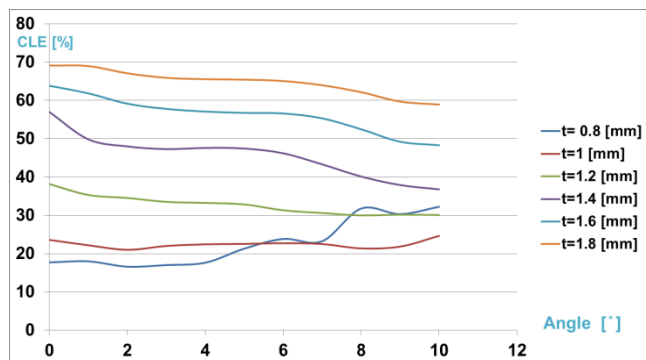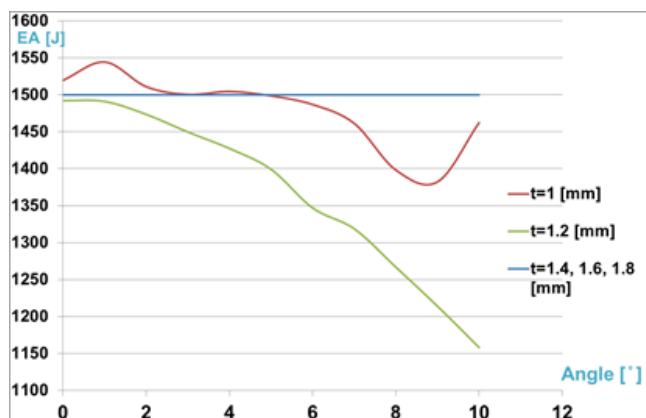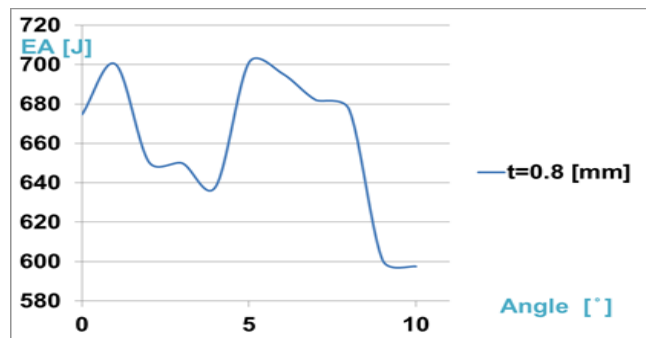ig.12. Fig.13. indicates the decrease of peak crushing force with the increase of frustum angle for wall thickness t = 0.8 mm.
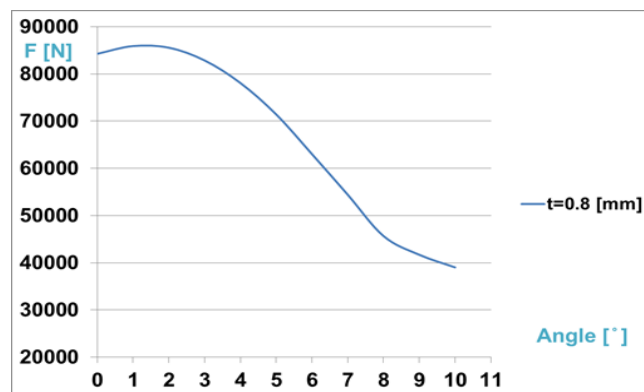
Fig. 13. Peak crushing force in terms of frustum angle for wall thickness t = 0.8 mm

6. FINAL REMARKS

The results of the parametric study indicate significant decrease of peak crushing force with the increase of frustum angle (see Fig. 9 and 13).

The influence of frustum angle on the crashworthiness indicators are different for different wall thickness values. Relation of the energy absorption in terms of frustum angle is non-linear. For the lowest examined wall thickness (t = 0.8 mm) , there are two optimal values of the frustum angle (α = 1º and α = 5º) , for which EA indicator is of maximum value. However, the increase of EA with respect to parallelepiped is not significant. For larger values of wall thickness the energy absorption is influenced by the frustum angle insignificantly. The ecception is wall thickness t = 1.2 nmm, for which EA indicator decreases significantly.

Crash load efficiency (CLE) increases with the increase of frustum angle for wall thickenes t = 0.8 mm only. For other examined values of wall thickness the influence is minor.

The presented results indicate, that research should be continued for wider range of geometric parameters. Thus, further parametric study is planned into multi-objective optimization of frusta under investigatuion, using response surface techniques.

REFERENCES

1. **Abbasi M., Reddy S., Ghafari – Nazari A., Fard M**. (2015), Multiobjective crashworthiness optimization of multi-cornered thin-walled sheet metal members, *Thin-Walled Struct.*, 89, 31–41.
2. **Alghamdi A.A.A.** (2001), Collapsible impact energy absorbers: an overview, *Thin-Walled Struct*, 39, 189-213.
3. **Dassault Systems** (2013), *Abaqus 6.13 Documentation, Abaqus Online Documentation*.
4. **Ferdynus M.** (2013), An energy absorber in the form of a thin-walled column with square cross-section and dimples, *Eksploatacja I Niezawodność Maintenance and Reliability*, 15 (3), 253-258.

5. **Ferdynus M., Kotełko M.** (2015), Dynamic axial crushing of flawed thin-walled square section tubes, *Stability of Structures XIV Symposium*, Departament of Strength of Materials, Lodz Univesity of Technology, 39-40.
6. **Jones N**. (2003) *Structural Impact*, Cambridge University Press.
7. **Kaczyński P., Rusiński E.** (2014), Strength estimation of joints in thin-walled Energy absorbing structures (in Polish), Oficyna Wydawnicza Politechniki Wrocławskiej.
8. **Kotełko M., Mołdawa A., Jankowski M**., (2014), Axial impact of open-section twcf columns experimental study, *Romanian Journal of technical sciences - applied mechanics*, former Revue Roumaine des sciences techniques, série de mécanique appliquée. (v. 59, No 1 -2, 2014); Special Issue "Stability and nonlinear analysis of steel structures – research advances", 59, 72-86.
9. **Ali M., Ohioma E., Kraft F., Alam K.** (2015) Theoretical, numerical, and experimental study of dynamic axial crushing of thin walled pentagon and cross-shape tubes, *Thin-Walled Struct.*, 94, 253-272.
10. **Reddy S., Abbasi M., Fard M**. (2015), Multi-cornered thin-walled sheet metal members for enhanced crashworthiness and occupant protection, *Thin-Walled Struct.*, 94, 56-66.
11. **Rusiński E., et al.,** , (2004) Tests of thin-walled beams joined by spot welding, *J. of Materials Processing Technology*, 157-158, 405-409.
12. **Sarkabiri B., Jahan A., Rezvani M.** (2015), Multi-objective crashworthiness optimization of thin-walled conical groove tubes filled with polyurethane foam, 3 rd Polish Congress of Mechanics, *21 st International Conference o Computer Methods in Mechanics*, 947-948.
13. **Sharifi S., Shakeri M., Ebrahimi Fakhari H., Bodaghi M.** (2015) Experimental investigation of bitubal circular energy absorbers under quasi-static axial load, *Thin-Walled Struc.*, 89, 42-53.

ON THE NUMERICAL SOLUTION OF THE INITIAL-BOUNDARY VALUE PROBLEM
WITH NEUMANN CONDITION FOR THE WAVE EQUATION
BY THE USE OF THE LAGUERRE TRANSFORM AND BOUNDARY ELEMENTS METHOD

Svyatoslav LITYNSKYY[*], Yuriy MUZYCHUK[*], Anatoliy MUZYCHUK[*]

[*]Applied Mathematics and Informatics, Programming Department, Ivan Franko National University of Lviv, Universytetska 1, Lviv, Ukraine

s.litynskyy@gmail.com, yuriy.muzychuk@gmail.com, anatol.muzychuk@gmail.com

Abstract: Abstract. We consider a numerical solution of the initial-boundary value problem for the homogeneous wave equation with the Neumann condition using the retarded double layer potential. For solving an equivalent time-dependent integral equation we combine the Laguerre transform (LT) in the time domain with the boundary elements method. After LT we obtain a sequence of boundary integral equations with the same integral operator and functions in right-hand side which are determined recurrently. An error analysis for the numerical solution in accordance with the parameter of boundary discretization is performed. The proposed approach is demonstrated on the numerical solution of the model problem in unbounded three-dimensional spatial domain.

Key words: Boundary Integral Equation, Time-Domain Boundary Integral Equation, Wave Equation, Sobolev Spaces, Generalized Solution, Retarded Surface Potentials, Laguerre Transform, Boundary Elements Method

1. INTRODUCTION

The development of efficient numerical methods for initial-boundary value problems for the wave equation in unbounded three-dimension spatial domains is actual for simulation of wave processes. In this formulation, approaches based on retarded potentials are widely used since they reduce the time-dependent problem in the unbounded domain to an integral equation on the bounded surface. Theory of such time-domain boundary integral equations (TDBIEs) for the wave equation was first developed by Bamberger and Ha-Duong (1986a, 1986b). In these papers the Galerkin method for TDBIEs was also proved. However, practical usage of the Galerkin method has some computational complexity, caused by the presence of dependency of potential density on the time and the spatial coordinates (so-called delay). It requires very precise spatial quadrature on parts of boundary elements which depend on delay, see, for example, Ha-Duong (2003) and Mykhas'kiv et al. (2014).

To overcome such difficulties after traditional discretizations on spatial variables some auxiliary problems may be considered for taking into account the time dependency. In particular, a convolution quadrature method (Lubich, 1994) has been utilized in many applications (see, for example, Laliena and Sayas, 2009; Monegato et al., 2011; Sayas and Qiu, 2015, and references there). It is based on sustainable methods for ordinary differential equations and is more efficient than Galerkin or collocation time approximations.

Another method is to apply the Fourier-Laplace integral transform with respect to the time variable as proposed in Bamberger and Ha-Duong (1986a), Ha-Duong (2003) and in Dominguez and Sayas (2013). This method is well suitable for theoretical investigations, however, the corresponding numerical inverse operation is complicated (except for some cases). In this respect the Laguerre transform (LT), for which the inverse transform is to find

the sum of corresponding Fourier-Laguerre serie, proved to be more constructive. In combination with the method of boundary integral equations (BIEs) such transform was used in papers Halazyuk et al. (1984), Jung et al. (2010), Litynskyy and Muzychuk (2015a), Lyudkevych and Muzychuk (1990), Chapko and Johansson (2016), Vavrychuk (2011) for numerical solution of various evolution problems.

In Litynskyy and Muzychuk (2015b, 2016) generalized solutions of the Dirichlet and Neumann initial-boundary value problems for the wave equation with homogeneous initial conditions were built by using the retarded potentials in some weighted Sobolev spaces, where desired solutions and densities of potentials allow the LT with respect to the time variable. Using this transform the Dirichlet and Neumann problems were reduced to sequences of BIEs. This work is dedicated to applying of the boundary elements method (BEM) to obtained equations in the case of the Neumann problem.

We begin in Section 2 with defining the Neumann initial-boundary value problem for the wave equation and then we reduce it to an infinite triangular system of BIEs using LT. In Section 3 we rewrite it as a sequence of equations with the same integral operator in the left-hand side and apply the BEM to it with error analysis. At the end we consider results of the numerical experiment on solving of the model problem.

2. REDUCTION OF THE NEUMANN PROBLEM
TO AN INFINITE SYSTEM OF BIEs

Let Ω^- be a domain in $\mathbb{R}^3$ with Lipschitz boundary Γ, $\Omega := \mathbb{R}^3 \backslash \overline{\Omega^-}$, $\mathbb{R}_+ := (0, \infty)$, $Q := \Omega \times \mathbb{R}_+$, $\Sigma := \Gamma \times \mathbb{R}_+$, and $\boldsymbol{\nu}(x)$ be a unit vector in the direction of the outward normal to the surface Γ at a point $x \in \Gamma$.

We consider the initial-boundary value problem: find a function

DE GRUYTER
OPEN

Svyatoslav Litynskyy, Yuriy Muzychuk, Anatoliy Muzychuk
On the Numerical Solution of the Initial-Boundary Value Problem with Neumann Condition for the Wave Equation
by the Use of the Laguerre Transform and Boundary Elements Method

DOI 10.1515/ama-2016-0044

$u(x,t)$, $(x,t) \in \overline{Q}$, that satisfies (in some sense) the homogeneous wave equation

$$\frac{\partial^2 u(x,t)}{\partial t^2} - \Delta u(x,t) = 0, \quad (x,t) \in Q, \tag{1}$$

homogeneous initial conditions

$$u(x,0) = 0, \quad \frac{\partial u(x,0)}{\partial t} = 0, \quad x \in \Omega, \tag{2}$$

and the Neumann boundary condition

$$\partial_{\boldsymbol{v}(x)} u(x,t) = g(x,t), \quad (x,t) \in \Sigma. \tag{3}$$

Here Δ is the Laplacian and $\partial_{\boldsymbol{v}}$ denotes the normal derivative.

To solve the problem (1)-(3) we use the retarded double layer potential

$$(\mathcal{D}\lambda)(x,t) := \frac{1}{4\pi} \int_{\Gamma} \partial_{\boldsymbol{v}(y)} \left(\frac{\lambda(z,t-|x-y|)}{|x-y|} \right)\big|_{z=y} d\Gamma_y, (x,t) \in Q, \tag{4}$$

where $\lambda: \Gamma \times \mathbb{R} \to \mathbb{R}$ is a density. It is known (see, e.g., Bamberger and Ha-Duong, 1986a or Polozhyy, 1964) that if an arbitrary function $\lambda(y,\tau)$, $(y,\tau) \in \Gamma \times \mathbb{R}$, is smooth enough and $\lambda(y,\tau) = 0$ when $y \in \Gamma, \tau \leq 0$, then function

$$u(x,t) := (\mathcal{D}\lambda)(x,t), \quad (x,t) \in Q, \tag{5}$$

satisfies (in the classical sense) the wave equation and initial conditions (2).

Note that for a sufficiently smooth density λ and surface Γ we can express the operator $\partial_{\boldsymbol{v}}$ as $\partial_{\boldsymbol{v}(x)} u(x,\cdot) = \boldsymbol{v}(x) \cdot \nabla_x u(x,\cdot)$, where ∇_x is the gradient operator. Then there exists the following limit

$$(\mathcal{W}\lambda)(x,t) :=$$
$$\frac{1}{4\pi} \boldsymbol{v}(x) \cdot \lim_{x' \to x} \nabla_{x'} \int_{\Gamma} \boldsymbol{v}(y) \cdot \nabla_y \left(\frac{\lambda(z,t-|x'-y|)}{|x'-y|} \right)\big|_{z=y} d\Gamma_y, \tag{6}$$

where $x' := x - \varepsilon \boldsymbol{v}(x) \in \Omega$, $\varepsilon > 0$, denotes a point close to the point $x \in \Gamma$. We say that x' approaches x, $x' \to x$, when $\varepsilon \to 0$. The function u satisfies the boundary condition (3), if the function λ is a solution of the retarded potential integral equation (RPIE)

$$(\mathcal{W}\lambda)(x,t) = g(x,t), (x,t) \in \Sigma. \tag{7}$$

We shall briefly give the essential notions of the Laguerre transform in the weighted Lebesgue space $L_\sigma^2(\mathbb{R}_+; X)$ with some parameter $\sigma > 0$ and weight $\rho_\sigma(t) = e^{-\sigma t}, t \in \mathbb{R}_+$. Here X is a Hilbert space with an inner product $(\cdot, \cdot)_X$ and an inducted norm $||\cdot||_X$. Elements $v \in L_\sigma^2(\mathbb{R}_+; X)$ are measurable functions $v: \mathbb{R}_+ \to X$ such that $\int_{\mathbb{R}_+} ||v(t)||_X^2 e^{-\sigma t} dt < \infty$. This space is equipped with the inner product

$$(v,w)_{L_\sigma^2(\mathbb{R}_+;X)} := \int_{\mathbb{R}_+} (v(t), w(t))_X \, e^{-\sigma t} dt, \; v, w \in L_\sigma^2(\mathbb{R}_+; X), \tag{8}$$

and the norm

$$||v||_{L_\sigma^2(\mathbb{R}_+;X)} := \sqrt{(v,v)_{L_\sigma^2(\mathbb{R}_+;X)}}, \quad v \in L_\sigma^2(\mathbb{R}_+; X). \tag{9}$$

It is well-known (Reed and Simon, 1977) that the space $L_\sigma^2(\mathbb{R}_+; X)$ is complete. We will assume that the elements of space $L_\sigma^2(\mathbb{R}_+; X)$ are extended with zero for non-positive arguments.

For any $m \in \mathbb{N}$ (set of natural numbers) let us denote the weighted Sobolev space as

$$H_\sigma^m(\mathbb{R}_+; X) := \{v \in L_\sigma^2(\mathbb{R}_+; X) | \, v^{(k)} \in L_\sigma^2(\mathbb{R}_+; X), k = \overline{1,m}\} \tag{10}$$

with the norm $||v||_{H_\sigma^m(\mathbb{R}_+;X)} := \left(\sum_{k=0}^m \left\| v^{(k)} \right\|_{L_\sigma^2(\mathbb{R}_+;X)}^2 \right)^{1/2}$. Here derivatives $v^k (k \in \mathbb{N})$ are understood in terms of the space $\mathcal{D}'(\mathbb{R}_+; X)$, elements of which are distributions with values in the space X.

We introduce a couple of notations. As the sequence of elements of set X we understand a vector-column $\boldsymbol{v} := (v_0, v_1, \dots)^T$. All possible sequences of elements of the set X are denoted by X^∞. We consider the Hilbert space $l^2(X) := \{\boldsymbol{v} \in X^\infty \mid \sum_{j=0}^\infty ||v_j||_X^2 < +\infty\}$ with the inner product $(\boldsymbol{v}, \boldsymbol{w}) = \sum_{j=0}^\infty (v_j, w_j)_X$, $\boldsymbol{v}, \boldsymbol{w} \in l^2(X)$, and the norm $||\boldsymbol{v}||_{l^2(X)} := (\sum_{j=0}^\infty ||v_j||_X^2)^{1/2}$, $\boldsymbol{v} \in l^2(X)$. Recall that for $X = \mathbb{R}$ we have $l^2(\mathbb{R}) = l^2 := \{\boldsymbol{v} \in \mathbb{R}^\infty \mid \sum_{j=0}^\infty |v_j|^2 < +\infty\}$.

Now let us give the definition of the Laguerre transform and outline some of its properties (Litynskyy and Muzychuk, 2015b). Consider a mapping $\mathcal{L}: L_\sigma^2(\mathbb{R}_+; X) \to X^\infty$ which operates according to the rule

$$f_k := \sigma \int_{\mathbb{R}_+} f(t) L_k(\sigma t) \, e^{-\sigma t} dt, \quad k \in \mathbb{N}_0 := \mathbb{N} \cup \{0\}, \tag{10}$$

where $\{L_k(\sigma \cdot)\}_{k \in \mathbb{N}_0}$ are Laguerre polynomials, which form orthogonal basis in the space $L_\sigma^2(\mathbb{R}_+)$ (Keilson et al., 1980). Also consider the mapping $\mathcal{L}^{-1}: l^2(X) \to L_\sigma^2(\mathbb{R}_+; X)$, which maps an arbitrary sequence $\boldsymbol{h} = (h_0, h_1, \dots, h_k, \dots)^T$ to a function

$$h(t) := (\mathcal{L}^{-1}\boldsymbol{h})(t) = \sum_{k=0}^\infty h_k L_k(\sigma t), \; t \in \mathbb{R}_+. \tag{11}$$

Proposition 2.1 (theorem 2 from Litynskyy and Muzychuk, 2015b) *The mapping $\mathcal{L}: L_\sigma^2(\mathbb{R}_+; X) \to X^\infty$ that maps the arbitrary function f to the sequence $\boldsymbol{f} = (f_0, f_1, \dots, f_k, \dots)^T$ according to the formula(10), is injective and its image is the space $l^2(X)$, and*

$$||f||_{L_\sigma^2(\mathbb{R}_+;X)}^2 = \frac{1}{\sigma} \sum_{k=0}^\infty ||f_k||_X^2. \tag{12}$$

In addition, for the arbitrary function $f \in L_\sigma^2(\mathbb{R}_+; X)$ we have an equality

$$\mathcal{L}^{-1}\mathcal{L}f = f, \tag{13}$$

where the mapping $\mathcal{L}^{-1}: l^2(X) \to L_\sigma^2(\mathbb{R}_+; X)$ is the inverse to $\mathcal{L}$ and maps the arbitrary sequence $\boldsymbol{h} = (h_0, h_1, \dots, h_k, \dots)^T$ to the function h according to the formula (11).

Definition 2.2 (Litynskyy and Muzychuk, 2015b) *Let $\sigma > 0$ and X be a Hilbert space. Mappings $\mathcal{L}: L_\sigma^2(\mathbb{R}_+; X) \to l^2(X)$ and $\mathcal{L}^{-1}: l^2(X) \to L_\sigma^2(\mathbb{R}_+; X)$, mentioned in Proposition 2.1, are called, respectively, direct and inverse Laguerre transforms, and the formula (12) is an analogue of the Parseval equality.*

Definition 2.3 (Litynskyy et al., 2009) *Let X, Y, Z be arbitrary sets and $q: X \times Y \to Z$ be some mapping. By a q-convolution of sequences $\boldsymbol{u} \in X^\infty$ and $\boldsymbol{v} \in Y^\infty$ we understand the sequence $\boldsymbol{w} := (w_0, w_1, \dots, w_j, \dots)^T \in Z^\infty$, whose elements are obtained by the rule*

$$w_j := \sum_{i=0}^j q(u_{j-i}, v_i) \equiv \sum_{i=0}^j q(u_i, v_{j-i}), \quad j \in \mathbb{N}_0; \tag{14}$$

the q-convolution of $\boldsymbol{u}$ and $\boldsymbol{v}$ is shortly written in the form $\boldsymbol{w} = \boldsymbol{u} \underset{q}{\circ} \boldsymbol{v}$.

If $X = \mathcal{L}(Y,Z)$ is the space of linear operators acting from the space Y into the space Z and $q(A,v) := Av, A \in \mathcal{L}(Y,Z)$, $v \in Y$, then for components of the q-convolution of arbitrary sequences

$A \in (\mathcal{L}(Y, Z))^\infty$ and $\boldsymbol{v} \in Y^\infty$ we will have the following formula

$$w_j = \sum_{i=0}^{j} A_{j-i} v_i, \quad j \in \mathbb{N}_0, \qquad (15)$$

and will write $\boldsymbol{w} := \boldsymbol{A} \underset{Z}{\circ} \boldsymbol{v}$.

Now let's consider a sequence of functions

$$e_0(z) := \frac{e^{-\sigma|z|}}{4\pi|z|}, \quad e_k(z) := \frac{e^{-\sigma|z|}}{4\pi|z|}(L_k(\sigma|z| - L_{k-1}(\sigma|z|)), \ k \in \mathbb{N},$$
$$z \in \mathbb{R}^3 \backslash \{0\}. \qquad (16)$$

Based on the above, in the space $H^1(\Omega) := \{v \in L^2(\Omega) | |\nabla v| \in L^2(\Omega)\}$ we can define a function sequence

$$\boldsymbol{u}(x) := (\boldsymbol{D} \underset{H^1(\Omega)}{\circ} \boldsymbol{\lambda})(x), \quad x \in \Omega, \qquad (17)$$

where $\boldsymbol{\lambda} = \mathcal{L}\lambda$ for any $\lambda \in L^2_\sigma(\mathbb{R}_+; H^{1/2}(\Gamma))$ and the sequence $\boldsymbol{D}$ is composed of operators $D_k : H^{1/2}(\Gamma) \to H^1(\Omega, \Delta), k \in \mathbb{N}_0$, given by the rule

$$(D_k \xi)(x) := \frac{1}{4\pi} \int_\Gamma \xi(y) \boldsymbol{v}(y) \cdot \nabla_y e_k(x - y) d\Gamma_y. \qquad (18)$$

Here $H^1(\Omega, \Delta) := \{v \in H^1(\Omega) | \Delta v \in L^2(\Omega)\}$, $H^{1/2}(\Gamma)$ denotes a space of traces of elements of $H^1(\Omega)$ on the surface Γ and $H^{-1/2}(\Gamma) := (H^{1/2}(\Gamma))'$. If u is expressed by the retarded double layer potential (4) with some density λ then the sequence (17) represents the transformation $\boldsymbol{u} = \mathcal{L}u$ (Litynskyy and Muzychuk, 2016). Similarly, applying the LT to the equation (7), we obtain a BIE system

$$\boldsymbol{W} \underset{H^{-1/2}(\Gamma)}{\circ} \boldsymbol{\lambda} = \boldsymbol{g} \quad in \quad l^2(H^{-1/2}(\Gamma)), \qquad (19)$$

where $\boldsymbol{g} = \mathcal{L}g$ and $\boldsymbol{W} : l^2(H^{1/2}(\Gamma)) \to l^2(H^{-1/2}(\Gamma))$ is a sequence of boundary operators

$$(W_k \xi)(x) := \frac{1}{4\pi} \boldsymbol{v}(x) \cdot \lim_{x' \to x} \nabla_{x'} \int_\Gamma \xi(y) \boldsymbol{v}(y) \cdot \nabla_y e_k(x' - y) d\Gamma_y,$$

$$k \in \mathbb{N}_0. \qquad (20)$$

After finding the solution $\boldsymbol{\lambda} = (\lambda_0, \lambda_1, \dots)^T$ of the BIEs (19), the generalized solution of the problem (1)-(3) can be presented as a sum of the series

$$u(x, t) = \sum_{k=0}^\infty \left(\sum_{i=0}^k D_{k-i} \lambda_i(x)\right) L_k(\sigma t), \quad (x, t) \in Q. \qquad (21)$$

Proposition 2.4 (theorem 2.4 from Litynskyy and Muzychuk, 2016) *Let* $g \in H^{m+4}_{\sigma_0}(\mathbb{R}_+; H^{-1/2}(\Gamma))$ *for some* $\sigma_0 > 0$ *and* $m \in \mathbb{N}_0$. *Then there exists a unique generalized solution of the problem (1)-(3), it belongs to the space* $H^{m+1}_{\sigma_0}(\mathbb{R}_+; H^1(\Omega))$ *and for any* $\sigma \geq \sigma_0$ *such an inequality holds*

$$||u||_{H^{m+1}_\sigma(\mathbb{R}_+; H^1(\Omega))} \leq C ||g||_{H^{m+4}_\sigma(\mathbb{R}_+; H^{-1/2}(\Gamma))}, \qquad (22)$$

where $C > 0$ *is a constant that is not dependent on* g.

In addition, the generalized solution of the problem (1)-(3) can be obtained by the inverse transform $u = \mathcal{L}^{-1}\boldsymbol{u}$, *where* $u_j \in H^1(\Omega, \Delta)$ $(j \in \mathbb{N}_0)$ *are the corresponding components of the q-convolution (17), and elements of the sequence* $\boldsymbol{\lambda} \in l^2(H^{1/2}(\Gamma))$ *are solutions of BIE system (19), in which* $\boldsymbol{g} = \mathcal{L}g$.

3. BEM FOR THE INFINITE BIE SYSTEM

We have now the new representation (21) of the solution of the problem (1)-(3) and the infinite BIE system (19) with unknown functions $\boldsymbol{\lambda} = (\lambda_0, \lambda_1, \dots)^T$. It is easy to see that the sys-

tem (19) can be rewritten as a sequence of BIEs

$$\begin{cases} W_0 \lambda_0 = g_0 & in \quad H^{-1/2}(\Gamma), \\ W_0 \lambda_1 = \tilde{g}_1 & in \quad H^{-1/2}(\Gamma), \\ \quad \cdot \ \cdot \ \cdot \ \cdot \ \cdot \ \cdot \ \cdot \\ W_0 \lambda_k = \tilde{g}_k & in \quad H^{-1/2}(\Gamma), \quad k \in \mathbb{N}, \\ \quad \cdot \ \cdot \ \cdot \ \cdot \ \cdot \ \cdot \ \cdot \end{cases} \qquad (23)$$

with recursive right-hand sides

$$\tilde{g}_k := g_k - \sum_{i=0}^{k-1} W_{k-i} \lambda_i, \quad k \in \mathbb{N}. \qquad (24)$$

For every $k \in \mathbb{N}_0$ the corresponding k-th equation of (23) is a hypersingular equation that has the form

$$W_0 \eta = f \quad in \quad H^{-1/2}(\Gamma). \qquad (25)$$

It has a unique solution $\eta \in H^{1/2}(\Gamma)$ for an arbitrary function $f \in H^{-1/2}(\Gamma)$ (Hsiao and Wendland, 2008). We can choose (by some criteria) value N and find from (23) the first components $\lambda_0, \lambda_1, \dots, \lambda_N$. Then the approximate solution of the problem (1)-(3) is the partial sum

$$u^N(x, t) = \sum_{j=0}^N \left(\sum_{i=0}^k D_{k-i} \lambda_i(x)\right) L_k(\sigma t), \quad (x, t) \in Q. \qquad (26)$$

We are now in position to apply the BEM for finding unknown functions. Consider in $H^{1/2}(\Gamma)$ a sequence of finite-dimensional subspaces $X^M \subset H^{1/2}(\Gamma)$, $M \in N$, assuming that $\{\phi_i\}_{i=1}^M$ is a basis of X^M. The numerical solution of the equation (25) can be presented as a linear combination

$$\eta^M := \sum_{i=1}^M \eta_i \phi_i \in X^M \qquad (27)$$

that is a solution of such variational equation

$$\langle W_0 \eta^M, \eta \rangle_\Gamma = \langle f, \eta \rangle_\Gamma \quad \forall \eta \in X^M. \qquad (28)$$

Applying the Galerkin method, that is taking the elements of the basis ϕ_j as test functions in order to find the vector of unknown coefficients $\boldsymbol{\eta}^{[M]} := \{\eta_i\}_{i=1}^M \in \mathbb{R}^M$, we will get a system of linear algebraic equations (SLAE)

$$W_0^{[M]} \boldsymbol{\eta}^{[M]} = \boldsymbol{f}^{[M]}. \qquad (29)$$

where $W_0^{[M]}[j, i] := \langle W_0 \phi_i, \phi_j \rangle_\Gamma$, $f_j^{[M]} := \langle f, \phi_j \rangle_\Gamma$, $i, j = \overline{1, M}$. As a result of the $H^{1/2}(\Gamma)$-ellipticity of the operator W_0, the matrix $W_0^{[M]}$ is positive definite (Costabel M., 1988; Hsiao and Wedland, 1977; Schtainbah, 2008). Therefore, the system (29) has a unique solution for an arbitrary right-hand side $\forall M \in N$.

Let $\Gamma_{\tilde{M}} = \cup_{l=1}^{\tilde{M}} \bar{\tau}_l$ be some approximation of the boundary Γ composed of triangular boundary elements $\{\tau_l\}_{l=1}^{\tilde{M}}$ with vertices $\{x^{[l_1]}, x^{[l_2]}, x^{[l_3]}\}$. We assume that vertices of all triangles have a global numbering $\{x_k\}_{k=1}^{M^*}$ and for each point x_k there exists an associated set $\mathcal{J}(k)$ of numbers of those triangles that have this point as a vertex. We treat the value $h := \max_{l=1,\tilde{M}}(\int_{\tau_l} ds)^{1/2}$ as the parameter of the spatial approximation.

Note that each triangle can be projected on a "standard'" triangle $\tau := \{\xi := (\xi_1, \xi_2) \in R^2 : 0 < \xi_1 < 1, \ 0 < \xi_2 < 1 - \xi_1\}$. Following Dautray and Lions (1992) and Schtainbah (2008), functions $\phi_1^1(\xi) = 1 - \xi_1 - \xi_2$, $\phi_2^1(\xi) = \xi_1$ and $\phi_3^1(\xi) = \xi_2$, defined locally on the triangle τ, form a set $\{\varphi_i^1\}_{i=1}^M$, $M = M^*$, that contains linearly-independent on $\Gamma_{\tilde{M}}$ functions. Moreover, $\text{supp} \ \varphi_i^1 = \cup_{l \in \mathcal{J}(i)} \bar{\tau}_l =: \tau_i^*$. Then the numerical solution $\boldsymbol{\lambda}^h := (\lambda_0^h, \lambda_1^h, \dots)^T$ of the BIE system (23) is sought in the form

$$\lambda_k^h = \sum_{l=1}^M \lambda_{k,l}^h \varphi_l^1 \in S_h^1(\Gamma) := \text{span}\{\varphi_i^1\}_{i=1}^M, \ k \in N_0, \qquad (30)$$

DE GRUYTER OPEN

Svyatoslav Litynskyy, Yuriy Muzychuk, Anatoliy Muzychuk
On the Numerical Solution of the Initial-Boundary Value Problem with Neumann Condition for the Wave Equation by the Use of the Laguerre Transform and Boundary Elements Method

DOI 10.1515/ama-2016-0044

where $\{\lambda_{k,l}^h\}_{l=1}^M$ are the unknown coefficients. In order to find the vector $\lambda_k^h := \{\lambda_{k,l}^h\}_{l=1}^M \in \mathbb{R}^M$ we obtain the following SLAE from (29)

$$W_0^h \lambda_k^h = g_k^h - \sum_{i=0}^{k-1} W_{k-i}^h \lambda_i^h, \quad k \in N , \tag{31}$$

where

$$W_j^h[i,l] = \int_{\tau_i^*} \varphi_i^1(x) \partial_{\nu(x)} \int_{\tau_l^*} \varphi_l^1(y) \partial_{\nu(y)} E_j(x-y) ds_y ds_x, \quad j = \overline{0,k}, \tag{32}$$

$$g_k^h[i] = \int_{\tau_i^*} \varphi_i^1(x) \tilde{g}_k(x) ds_x, \quad i, l = \overline{1, M}. \tag{33}$$

After finding the consequent vector λ_k^h we can compute the corresponding element of the sequence $\boldsymbol{u}^h := (u_0^h, u_1^h, \ldots, u_k^h, \ldots, u_N^h, 0, \ldots)^T$:

$$u_k^h(x) = \sum_{j=0}^k (D_j \lambda_{k-j}^h)(x), \quad x \in \Omega. \tag{34}$$

Having $\boldsymbol{u}^h$, the numerical solution of the Neumann problem is found by the formula

$$u^{N,h}(x,t) = \sum_{j=0}^N u_k^h(x) L_k(\sigma t), \quad (x,t) \in Q. \tag{35}$$

Let us obtain, following Hsiao and Wedland (1977), an a priory error estimate of the numerical solution after the introduction of Sobolev spaces of piecewise-smooth on the boundary Γ functions. Let Γ be a union $\Gamma = \cup_{i=1}^{\tilde{N}} \overline{\Gamma}_i$ of surfaces Γ_i ($\Gamma_i \cap \Gamma_j = \emptyset$ when $i \neq j$), each of which has a sufficiently smooth parameterization $\Gamma_i := \{x \in R^3 : x = \tilde{\chi}_i(\xi), \ \xi \in \tilde{\tau}_i \subset R^2\}$. Then, using the set of the non-negative functions $\phi_i \in C_0^\infty(R^3)$ such that $\sum_{i=1}^{\tilde{N}} \phi_i(x) = 1 \quad \forall x \in \Gamma, \qquad \phi_i(x) = 0 \quad \forall x \in \Gamma \backslash \Gamma_i$, an arbitrary piecewise-smooth function can be given in a form

$$v(x) = \sum_{i=1}^{\tilde{N}} \phi_i(x) v(x) = \sum_{i=1}^{\tilde{N}} v_i(x) \quad \forall x \in \Gamma, \tag{36}$$

where $v_i(x) := \phi_i(x)v(x) \quad \forall x \in \Gamma_i$. Taking into account the parameterization of the fragments Γ_i, we consider Sobolev spaces $H^s(\tilde{\tau}_i)$, elements of which are functions $\tilde{v}_i(\xi) := v_i(\tilde{\chi}_i(\xi))$ when $\xi \in \tilde{\tau}_i$, with corresponding norms and semi-norms

$$||\tilde{v}_i||_{H^s(\tilde{\tau}_i)} := (\sum_{|\alpha| \leq m} ||\partial^\alpha \tilde{v}_i||_{L^2(\tilde{\tau}_i)}^2)^{\frac{1}{2}},$$

$$|\tilde{v}_i|_{H^s(\tilde{\tau}_i)} := (\sum_{|\alpha|=m} |\partial^\alpha \tilde{v}_i|_{L^2(\tilde{\tau}_i)}^2)^{\frac{1}{2}}, \quad s = m \in N ;$$

$$|\tilde{v}_i|_{H^s(\tilde{\tau}_i)} := (\sum_{|\alpha|=m} \int_{\tilde{\tau}_i} \int_{\tilde{\tau}_i} \frac{|\partial^\alpha \tilde{v}_i(\xi) - \partial^\alpha \tilde{v}_i(\eta)|^2}{|\xi - \eta|^{2+2\sigma}} ds_\xi ds_\eta)^{\frac{1}{2}},$$

$$s = m + \sigma, \ \sigma \in (0,1). \tag{37}$$

Here ∂^α is a notation of the partial derivative with a multi-index $\alpha = (\alpha_1, \alpha_2)$. Moreover, for functions that are defined on the whole boundary Γ, we use the semi-norm

$$|v|_{H^s(\Gamma)} := (\sum_{i=1}^{\tilde{N}} |\tilde{v}_i|_{H^s(\tilde{\tau}_i)}^2)^{1/2}. \tag{38}$$

Lemma 3.1 *Let $\lambda \in (H^s(\Gamma))^\infty$ for some $s \in [\frac{1}{2}, 2]$ be the exact solution of the BIE system* (23)*, which satisfies an inequality*

$$\sum_{j=0}^\infty |\lambda_j|_{H^s(\Gamma)} < +\infty. \tag{39}$$

Then for any values of parameters $N \in \mathbb{N}_0$ and $T \in \mathbb{R}_+$ the following error estimates hold

$$\left\| \lambda^N(\cdot, t) - \lambda^{N,h}(\cdot, t) \right\|_{H^{\frac{1}{2}}(\Gamma)} \leq \tilde{C}_{N,T} h^{s-\frac{1}{2}} \sum_{k=0}^N |\lambda_k|_{H^s(\Gamma)},$$

$$t \in (0,T), \tag{40}$$

$$|u^N(x,t) - u^{N,h}(x,t)| \leq \tilde{C}_{N,T}^* h^{s-\frac{1}{2}} \sum_{k=0}^N |\lambda_k|_{H^s(\Gamma)},$$

$$x \in \Omega, \quad t \in (0,T), \tag{41}$$

where $\tilde{C}_{N,T}$ and $\tilde{C}_{N,T}^*$ are constants independent of h.

Proof. Let us fix two arbitrary values $N \in \mathbb{N}_0$ and $T \in \mathbb{R}_+$ and consider $\delta_{N,T} := ||\lambda^N(\cdot, t) - \lambda^{N,h}(\cdot, t)||_{H^{1/2}(\Gamma)} = ||\sum_{k=0}^N (\lambda_k(\cdot) - \lambda_k^h(\cdot)) L_k(\sigma t)||_{H^{1/2}(\Gamma)}$ for any $t \in (0,T)$. Setting $C_{N,T} := \max_{t \in [0,T], k=\overline{0,N}} |L_k(\sigma t)|$ we can write

$$\delta_{N,T} \leq C_{N,T} \sum_{k=0}^N ||\lambda_k - \lambda_k^h||_{H^{1/2}(\Gamma)}. \tag{42}$$

Note that for any function λ_k, which satisfies an equation like (25), the inequality (39) yields the following estimate (Schtainbah, 2008)

$$||\lambda_k - \lambda_k^h||_{H^{1/2}(\Gamma)} \leq \tilde{C}_k h^{s-1/2} |\lambda_k|_{H^s(\Gamma)}, \quad k \in N_0, \tag{43}$$

where $\tilde{C}_k$ are constants independent of h. Using this inequality and setting $\tilde{C}_{N,T} := C_{N,T} \max_{k=\overline{0,N}} \{\tilde{C}_k\}$ we obtain (40) from (42).

Since in the case of Lipschitz boundary all functions $E_j(x - \cdot)$ are bounded and infinitely continuously differentiable on Γ for any fixed point $x \in \Omega$, we get inequality $||\partial_{\nu(\cdot)} E_j(x - \cdot)||_{H^{-1/2}(\Gamma)} \leq c_j^* = const$. Taking it and (43) into account by the Generalized Cauchy-Schwarz inequality we obtain $|u_k(x) - u_k^h(x)| = |\sum_{i=0}^k \langle \partial_{\nu(\cdot)} E_{k-i}(x - \cdot), (\lambda_i - \lambda_i^h) \rangle_\Gamma| \leq \tilde{c}_k h^{s-1/2} \sum_{i=0}^k |\lambda_i|_{H^s(\Gamma)}$, where $\tilde{c}_k$ are constants independent of h. Using this estimate, the rest of the proof for (41) can be carried out analogously to the proof for (40). ∎

4. RESULTS OF THE COMPUTATIONAL EXPERIMENT

Let us demonstrate the suggested method to solve some model problem and assess the accuracy of numerical solutions. Let the domain $\Omega := R^3 \backslash \Omega^-$ be outside of a cube $\Omega^- := [-1,1] \times [-1,1] \times [-1,1]$ and the function $g(x,t) := -\partial_{\nu(x)} v(x,t)$, $(x,t) \in \Sigma$, in the boundary condition (3) is defined by means of a spherical impulse $v(x,t) := f_3(t - |x| + 1)|x|^{-1}$, $(x,t) \in Q$, where f_3 is a cubic B-spline.

Tab. 1. Convergence behavior of $u_0^h(x)$ at points $x = (x_1, 0,0)$

x_1	$u_0^h(x)$			$u_0(x)$
	$\overline{M} = 588$	$\overline{M} = 1200$	$\overline{M} = 1728$	
1.2	4.97567×10^{-1}	5.16241×10^{-1}	5.23443×10^{-1}	5.58600×10^{-1}
1.5	2.19226×10^{-1}	2.26607×10^{-1}	2.29583×10^{-1}	2.45252×10^{-1}
2.0	6.07058×10^{-2}	6.25240×10^{-2}	6.32929×10^{-2}	6.76676×10^{-2}
3.0	5.50191×10^{-3}	5.64833×10^{-3}	5.71311×10^{-3}	6.10521×10^{-3}
4.0	5.59834×10^{-4}	5.73967×10^{-4}	5.80360×10^{-4}	6.19688×10^{-4}

Since the function v satisfies the wave equation in Ω we can use it as a analytical solution of the Neumann problem (1)-(3). Following Muzychuk and Chapko (2012), we can also consider elements of sequence $v(x) = \mathcal{L}v(x,\cdot)$, $x \in \Omega$, as exact values for q-convolution $u^h(x)$, computed according to the formula (34) on the solution λ^h of BIE (23) with $g_k = -\partial_v v_k$, $k \in \mathbb{N}_0$, in right-hand side.

At first we consider how parameter h of BEM, that depends on the number $\overline{M}$ of boundary elements on the surface Γ, has effect on the approximation error of elements of the sequence v via corresponding elements of the sequence u^h. Table 1 contains values of numerical solutions u_0^h computed with various values $\overline{M}$. As expected, at all points of observation these values tend to corresponding exact values u_0 with decreasing of the value h. Note, that components u_k^h, $k \in \mathbb{N}$, have the same convergence behaviour.

Tab. 2. Error analysis of $u_0^h(x)$

$\overline{M}$	δ^h	eoc	$\varepsilon^h(\%)$
300	0.03539		8.34
588	0.02565	0.957	5.92
768	0.02254	0.967	5.16
972	0.02011	0.969	4.58
1200	0.01815	0.985	4.11
1728	0.01518	0.992	3.32

Let us now compute values $\delta^h := ||u_0^h - u_0||_{L^2(a,b)}$ and $\varepsilon^h := \delta^h ||u_0||_{L^2(a,b)}^{-1} \cdot 100\%$, where (a, b) is a spatial interval from which observation points x are taken, and also evaluate the estimated order of convergence $eoc := (\ln \delta^{h_j} - \ln \delta^{h_{j+1}})(\ln h_j - \ln h_{j+1})^{-1}$ (Schtainbah, 2008), where h_j and h_{j+1} are parameters of consequent spatial discretizations. Computed with $a = (1.2, 0, 0)$ and $b = (10, 0, 0)$ results are given in Tab. 2. They highlight that $eoc \approx 1$ for this class of problems. Note, that an analogous behaviour is intrinsic also to u_k^h, $k \in \mathbb{N}$.

On Figure 1 numerical solutions $u^{h,N}(x, t)$ of the Neumann problem (1)-(3), computed with various values of the parameter N in the partial sum (35) and $\overline{M} = 972$, are plotted as a comparison against the analytical solution $v(x, t)$. As we can see these results have close agreement in some initial time interval already for not large values N. This interval can be enlarged with increasing N. Numerical solutions $u^{h,N}(x, t)$ computed with $N = 40$ and $\overline{M} = 972$ are presented on Figure 2. They demonstrate signal propagation at different observation points x.
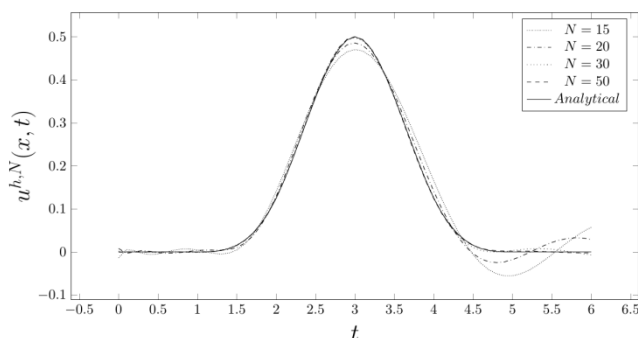

Fig.1. Numerical solutions $u^{h,N}(x, t)$ of problem (1)-(3) at point $x = (2,0,0)$ with various values N
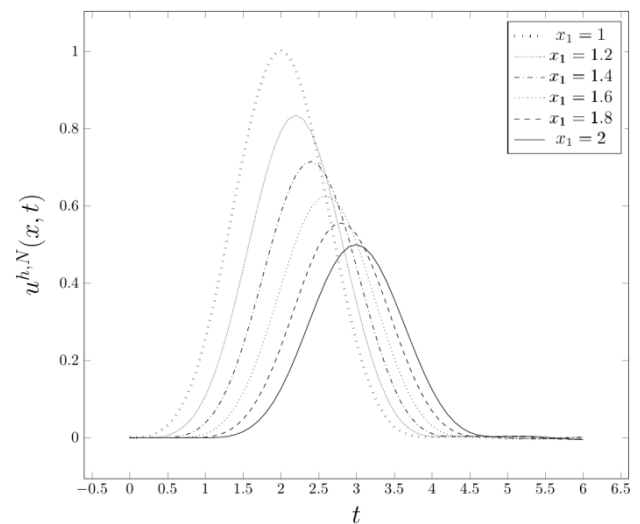

Fig. 2. Numerical solutions $u^{h,N}(x, t)$ of problem (1)-(3) at points $x = (x_1, 0, 0)$

5. CONCLUSION

The proposed method enables us to find the numerical solution of the Neumann problem for the homogeneous wave equation with homogeneous initial conditions. Applying the LT, we omit the delay in the retarded double layer potential and in the time-domain BIE making computation process clearer. As result we obtain the sequence of BIEs which enable us to use the BEM efficiently.

Results of computational experiments confirm apriori error estimates that are obtained in the article.

REFERENCES

1. **Bamberger A., Ha-Duong T.** (1986a), Variational formulation for calculating the diffraction of an acoustic wave by a rigid surface, *Math. Methods Appl. Sci.,* 8(4), 598-608 (in French).
2. **Bamberger A., Ha-Duong T.** (1986b), Variational space-time formulation for computation of the diffraction of an acoustic wave by the retarded potential (I), *Math. Methods Appl. Sci.,* 8(3), 405-435 (in French).
3. **Chapko R., Johansson B. T.** (2016), Numerical solution of the Dirichlet initial boundary value problem for the heat equation in exterior 3-dimensional domains using integral equations, *Journal of Engineering Mathematics*, 1-15.
4. **Costabel M.** (1988), Boundary integral operators on Lipschitz domains: elementary results, *SIAM J. Math. Anal., V. 19*, 613626.
5. **Dautray R., Lions J. L.** (1992), *Mathematical analysis and numerical methods for science and technology, Volume 5 Evolution problems I.*, Springer-Verlag, Berlin.
6. **Dominguez V., Sayas F. J.** (2013), Some properties of layer potentials and boundary integral operators for wave equation, *Journal of Integral Equations and Applications,* 25(2), 253-294.
7. **Ha-Duong T.** (2003), On retarded potential boundary integral equations and their discretization, *In Davies P.; Duncan D.; Martin P.; Rynne B. (eds.): Topics in computational wave propagation. Direct and inverse problems,* Berlin: Springer-Verlag, 301-336.
8. **Halazyuk V. A., Lyudkevych Y. V., Muzychuk A. O.** (1984), Method of integral equations in non-stationary defraction problems, *LSU. Dep. in UkrNIINTI,* 601 (in Ukrainian).
9. **Hsiao G. C., Wendland W. L.** (1977), A finite element method for some integral equations of the first kind, *J. Math. Anal. Appl.,* 58, 449–481.

DE GRUYTER
OPEN

Svyatoslav Litynskyy, Yuriy Muzychuk, Anatoliy Muzychuk
On the Numerical Solution of the Initial-Boundary Value Problem with Neumann Condition for the Wave Equation
by the Use of the Laguerre Transform and Boundary Elements Method

DOI 10.1515/ama-2016-0044

10. **Hsiao G. C., Wendland W. L.** (2008), *Boundary Integral Equations*, Applied Mathematical Sciences, Springer-Verlag Berlin Heidelberg.

11. **Jung B. H., Sarkar T. K., Zhang Y., Ji Z., Yuan M., Salazar-Palma M., Rao S. M., Ting S. W., Mei Z., De A.** (2010), *Time and frequency domain solutions of em problems using integral equations and a Hybrid methodology*, Wiley-IEEE Press.

12. **Keilson J.** (1981), The bilateral Laguerre transform, *Applied Mathematics and Computation,* 8(2), 137–174.

13. **Laliena A. R., Sayas F. J.** (2009), Theoretical aspects of the application of convolution quadrature to scattering of acoustic waves, *Numer. Math.,* 112(4), 637-678.

14. **Litynskyy S., Muzychuk A.** (2015a), Retarded Potentials and Laguerre Transform for Initial-Boundary Value Problems for the Wave Equation, *20th IEEE International Seminar/Workshop on Direct and Inverse Problems of Electromagnetic and Acoustic Wave Theory (DIPED-2015), Lviv: Pidstryhach IAPMM of NASU*, 139-142 (in Ukrainian).

15. **Litynskyy S., Muzychuk A.** (2015b), Solving of the initial-boundary value problems for the wave equation by the use of retarded potential and the Laguerre transform, *Matematychni Studii,* 44(2), 185-203 (in Ukrainian).

16. **Litynskyy S., Muzychuk A.** (2016), On the generalized solution of the initial-boundary value problems with Neumann condition for the wave equation by the use of retarded double layer potential and the Laguerre transform, *Journal of Computational and Applied Mathematics*, 2(122), 21-39.

17. **Litynskyy S., Muzychuk Yu., Muzychuk A.** (2009), On weak solutions of boundary problems for an infinite triangular system of elliptic equations, *Visnyk of the Lviv university. Series of Applied mathematics and informatics,* 15, 52-70 (in Ukrainian).

18. **Lubich Ch.** (1994), On the multistep time discretization of linear initial-boundary value problems and their boundary integral equations, *Numer. Math.*, 365-389.

19. **Lyudkevych Y. V., Muzychuk A.** (1990), Numerical solution of boundary problems for wave eqution, *L'viv: LSU,* 80 (in Ukrainian).

20. **Monegato G., Scuderi L., Stanic M. P.** (2011), Lubich convolution quadratures and their application to problems described by space-time BIEs, *Numerical Algorithms, Springer Science,* 3(56), 405–436.

21. **Muzychuk Yu. A., Chapko R. S.** (2012), On variational formulations of inner boundary value problems for infinite systems of elliptic equations of special kind, *Matematychni Studii,* 38(1), 12-34.

22. **Mykhas'kiv V. V., Martin P. A., Kalynyak O. I.** (2014), Time-domain BEM for 3-D transient elastodynamic problems with interacting rigid movable disc-shaped inclusions, *Computational Mechanics*, 53(6), 1311-1325.

23. **Polozhyy H.** (1964), *Equations of mathematical physics*, Nauka, Moscow (in Russian).

24. **Reed M., Simon B.** (1977), *Methods of modern mathematical physics*, Mir, Moscow (in Russian).

25. **Sayas F. J., Qiu T.** (2015), The Costabel-Stephan system of Boundary Integral Equations in the Time Domain, *Mathematics of Computation,* 85, 2341–2364.

26. **Schtainbah O.** (2008), *Numerical Approximation Methods for Elliptic Boundary Value Problems. Finite and Boundary Elements*, Springer Science.

27. **Vavrychuk V. H.** (2011), Numerical solution of mixed non-stationary problem of thermal conductivity in partially unbounded domain, *Visnyk of the Lviv university, Series of Applied mathematics and informatics,* 17, 62-72 (in Ukrainian).

MODELLING AND TESTING OF THE PIEZOELECTRIC BEAM AS ENERGY HARVESTING SYSTEM

Andrzej KOSZEWNIK[*], Krzysztof WERNIO[*]

[*]Bialystok University of Technology, Faculty of Mechanical Engineering, ul. Wiejska 45C,15-351 Bialystok, Poland

a.koszewnik@pb.edu.pl, werniokrzysztof@gmail.com

Abstract: The paper describes modelling and testing of the piezoelectric beam as energy harvesting system. The cantilever beam with two piezo-elements glued onto its surface is considered in the paper. As result of carried out modal analysis of the beam the natural frequencies and modes shapes are determined. The obtained results in the way mentioned above allow to estimate such location of the piezo-actuator on the beam where the piezo generates maximal values of modal control forces. Experimental investigations carried out in the laboratory allow to verify results of natural frequencies obtained during simulation and also testing of the beam in order to obtain voltage from vibration with help of the piezo-harvester. The obtained values of voltage stored on the capacitor C_0 shown that the best results are achieved for the beam excited to vibration with third natural frequency, but the worst results for the beam oscillating with the first natural frequency.

Key words: Cantilever Beam, Piezo-Actuator, Energy Harvesting System, Modal Analysis

1. INTRODUCTION

Vibration-based energy harvesting has received a great attention in the past decade. Research motivation in this field is due to the reduced power requirement of small electronic components such as the wireless sensors used in structural health monitoring applications. Research in this area involves understanding the mechanics of vibrating structures, the behaviour of piezoelectric materials and the electric circuit theory. This promising way of powering small electronic components and remote sensors has attracted researches from different disciplines of mechanical and electrical engineering.

As described main editors of the book (Priya and Inman, 2009) exist three basic mechanisms of conversation vibration to electric energy: electromagnetic (Arnold, 2007; Williams and Yates, 1996), electrostatic (Roundy et al., 2002), and piezoelectric (Sodano et al., 2005). These transduction mechanisms in the last decade have been widely investigated by researches for vibration-based energy harvesting. The literature of the last eight years shows that piezoelectric transduction has received the most attention for vibration to electricity conversation. Especially, it is shown in review articles (Anton and Sodano, 2007; Bai et al, 2015; Borowiec, 2015; Chen et al., 2006; Friswell et al., 2012; Tan et al., 2015) which the simulation and experimental results proved that vibration to energy conversation by piezoelectric might be used in many applications. In these references probem of non-linear of the piezoelectric elements is considered in order to achieve maximum harvested energy.

Typically, a piezoelectric harvester is a cantilever beam with piezo-ceramic layers located on the a vibrating shake. As a result of vibration of the beam the dynamic strain induced in the piezo-ceramic layers generates an alternating voltage output across the electrodes covering the piezo-ceramic layers. In many cases such approach allow to determine the mathematical model of the beam that can be used in many practical applications.

In the present paper problem of conversion vibration to electric energy for active cantilever beam is described. In considered case the beam is excited to vibration by the piezo-stripe actuator located on the top side of the beam in quasi-optimal location. As a result of applied sinusoidal excitation to the piezo-actuator with frequency equals natural frequency the voltage from the piezo-harvester is obtained. The experimental investigations carried out at the lab stand show how the excitation of the beam may influence on the voltage derived from the piezo-harvester located on the free end of the beam. In results of such analysis can see relationship between mechanical and electrical part of consider smart beam.

2. MODELLING OF THE BEAM – ANALYTICAL APPROACH

In this section the mathematical model of the cantilever beam with piezo-actuator and the piezo-harvester shown in Fig.1 is analytically formulated.
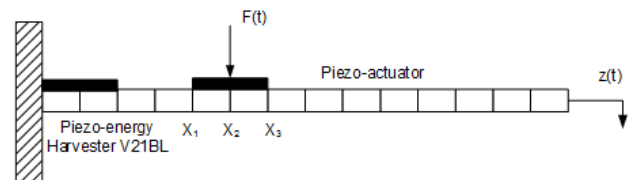

Fig. 1. The cantilever steel beam with the piezo-actuator and the piezo-harvester

The model of the beam for the first four lowest natural frequencies is determined for given actuator locations. In result of such assumed assumptions the equation of forced vibrations of the beam can be written as:

$$\frac{\partial^4 y(x,t)}{dx^4} + a_z{}^2 \frac{\partial^2 y(x,t)}{dt^2} =$$
$$\frac{1}{E_b I_b} F_A \big(-\delta(x - x_1) + 2\delta(x - x_2) - \delta(x - x_3) \big) \qquad (1)$$

where: $a_z = \sqrt{\frac{\rho_b A_b}{E_b I_b}}$, δ – Dirac function.

Eq.(1) has been rewritten after modal transformation to the following form:

$$\frac{\partial^4 y(x,t)}{dx^4} + a_z{}^2 \frac{\partial^2 y(x,t)}{dt^2} = \sum_{n=1}^{\infty} F_{An} U_n(x) \qquad (2)$$

where: $F_{An} = F_A(-U_n(x_1) + 2U_n(x_2) - U_n(x_3))$ – modal transversal force of the piezo-actuator.

Transformations presented in Eq.(2) lead to determine of the mode shapes of the beam. However before to do need consider the boundary conditions of the piezoelectric beam expressed in following form:
Fixed end:

$$y(x,t) = 0 \text{ and } \frac{\partial y(x,t)}{\partial x}\bigg|_{x=0} = 0 \qquad (3)$$

Free end: $\quad M(x,t) = \frac{\partial^2 y(x,t)}{\partial x^2}\bigg|_{x=l} = 0 \quad$ and $\quad F(x,t) = \frac{\partial^3 y(x,t)}{\partial x^3}\bigg|_{x=l} = 0$

As results of boundary conditions the displacement $y(x,t)$ is splitted into variable described in space – $U(x)$ and variable dependent in time – $T(t)$. Such approach leads to determining of the modes shapes $U_n(x)$ that it expressed in the following form (Kelly, 2007):

$$U_n(x) = (\text{sh} k_n l + \sin k_n l)(\text{ch} k_n x - \cos k_n x) +$$
$$- (\text{ch} k_n l + \cos k_n l)(\text{sh} k_n x - \sin k_n x) \qquad (4)$$

where: $k_n l = \frac{2n-1}{2}\pi$ for $n = 1,2,3$.

The mechatronic system shown in Fig.1 is transformed to equivalent model that it is shown in Fig. 2 The obtained model is described by mass, spring, damper and the piezo structure energy storage system.
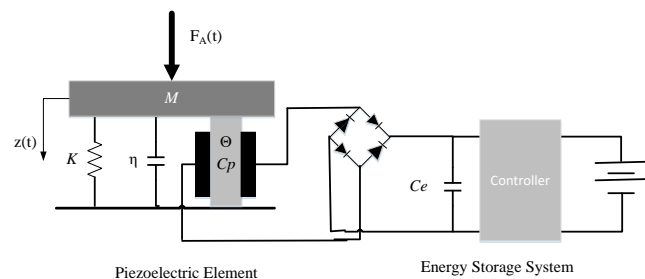

Fig. 2. The euqivalent model for a piezoelectric vibration energy harvesting system

As it can be seen in Fig.2 the model consists a vibrating piezoelectric element which generates an AC voltage which next is stabilize to DC voltage. Especially it is important in case of wireless sensors that they require such supply. The obtained in this way model is electromechanical system which it is expressed as:

$$\begin{cases} M\ddot{z}(t) + \eta\dot{z}(t) + Kz(t) + \Gamma V_p(t) \\ I(t) = \Gamma\dot{z}(t) - C_p\dot{V}_p(t) \end{cases} \qquad (5)$$

where: M – effective mass of the system, η – coefficient of damper, K – effective stiffness of the system, Γ – electromechanical coupling factor, $V_p(t)$ – the output voltage of equivalent system.

Moreover, above calculations lead to determine of the electromechanical behaviour of the beam. In this order need to define Generalized Electromechanical Coupling Factor known in the literature as GEMC factor Γ that it shows relationship between mechanical and electrical parameters of the piezo-energy harvester element. This factor is expressed in the following form (Koszewnik et al., 2015):

$$\Gamma^2 = k_{31}{}^2 k_p C_0 \qquad (6)$$

where: k_{31} – coupling coefficient for length extensional, k_p – stiffness of the piezoelectric material, C_0 – output capacitance.

Taking into account form of the GEMC factor described with Eq.(6) and the equation of maximum power output derived from harvester expressed as:

$$P_{OUT\_MAX} = \frac{F_A{}^2}{8d}\bigg|_{\substack{\omega=\omega_n \\ d=d_e=d_m}} \qquad (7)$$

where: P_{OUT_MAX} – the maximum value of the power output, ω_n – the natural frequency of the beam, $m\, d_e, d_m m$ – the electrical and mechanical damping.

Quasi-static electro-mechanical behavior of the beam can be described in a following form:

$$\begin{bmatrix} F_A \\ Q \end{bmatrix} = \begin{bmatrix} k_b & \Gamma \\ \Gamma & -C_0 \end{bmatrix} \begin{bmatrix} \Delta x \\ U \end{bmatrix} \qquad (8)$$

where: F_A – the force applied to the structure, Q – the charge on the piezo, k_b – the stiffness of the beam, Δx – elongation, U – output voltage.

In case of assumed perfect link between the piezoelectric layer and the beam ($\Delta x = z$) is possible transformation of Eq.(8) to form:

$$\begin{bmatrix} F_A \\ Q \end{bmatrix} = \begin{bmatrix} k_b & \Gamma \\ \Gamma & -C_0 \end{bmatrix} \begin{bmatrix} z \\ U \end{bmatrix} \qquad (9)$$

where: z – the displacement of free end of the beam.

Finally, the force F_A applied to the beam structure can be expressed as sum of mechanical part of the beam caused by mass velocity and electrical part caused by mounted piezoelectric elements expressed in the following form:

$$F_A = k_b z + \Gamma U \qquad (10)$$

3. MODELLING OF THE BEAM – NUMERICAL APPROACH

The cantilever beam with two rectangular piezoelectric stripes (an actuator and a harvester) glued onto its surface is shown in Fig.1. The steel beam has the dimension of 25x400x1.5mm, while the actuator QP20N and the piezo-harvester V21B are single piezoelectric stripes of 25x50x0.76 mm and 16.6x36.6x0.5, respectively. The parameters of the cantilever beam are collected in Table.1. The model of the piezo-actuator is considered as a "static coupled model" (Gosiewski and Koszewnik, 2007) with

the difference that the piezo-stripe is divided into two equal segments. As a result the bending moment generated by the piezo-actuator is represented by a couple of opposite site forces concentrated at the segment's edge as it is shown in Fig.1 .

Tab. 1. Parameters of a cantilever beam

Parameter	Value
Length l	0.4 m
Width b	0.025 m
Thickness t	0.0015 m
Youngs modules E_b	210 GPa
Density ρ_b	7800 kg/m³

4. MODAL ANALYSIS OF THE BEAM

Modal analysis of the piezoelectric beam is divided into two steps. In the first step of simulations the natural frequencies and mode shapes of the beam are determined. In this order FEM model of the beam shown in Fig.1 is used and next investigated with help of Ansys software. In results of these analysis the first four lowest natural frequencies and mode shapes are achieved. The obtained results are shown in Fig. 3 and Tab. 2.

Fig. 3. The first four lowest mode shapes of the cantilever beam.
The red colour denotes maximum displacement of the beam, but the blue line denotes minimum displacement

Tab. 2. First four natural frequencies of the piezoelectric beam

	1st mode	2nd mode	3rd mode	4th mode
Natural frequency of the beam [Hz]	7.13	48.34	141.9	288.2

Next, the investigations is focused to determine such location of the piezo-actuator where this piezo generates maximal control forces. In this case the piezo is shifted onto surface on the beam from fixed end to free end of the beam with step equal 1/2 length of the piezo. For each location of the piezo-actuator the modal control forces are calculated and shown in Fig. 4.
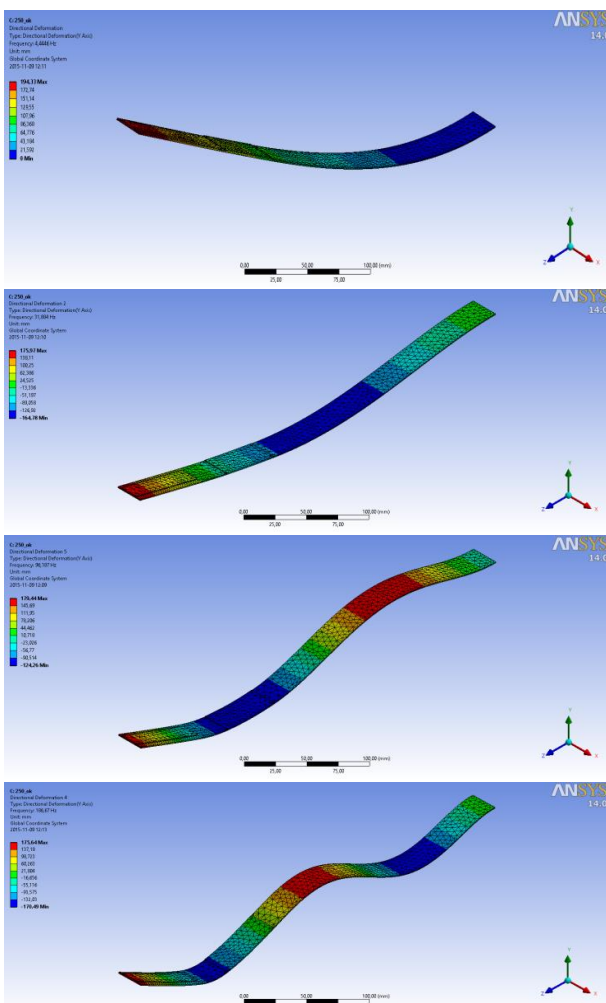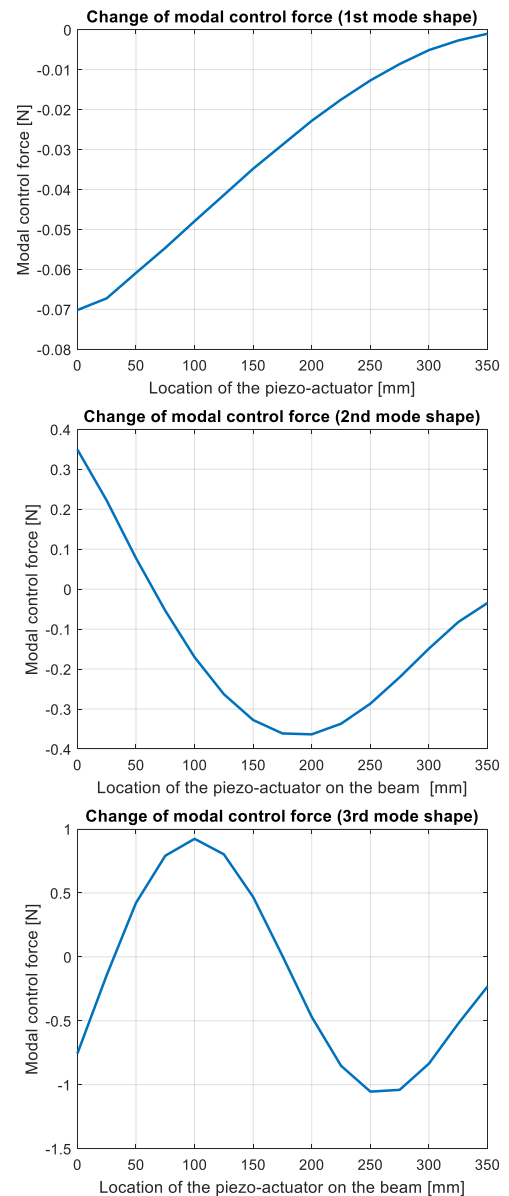

Fig. 4. Influence of the location of the piezo-actuator
on modal control force for the first three lowest mode shapes

Taking into account the obtained results shown in Fig.4 it can be noticed that the maximal modal control forces are generated by the piezo-actuator works with the third mode shape but minimal control force when it works with the first mode shapes. Then,

based on the obtained results can assume that consider piezo will excite beam to vibration in maximal way in vicinity of extremum of the modal control forces. So, in order to achieve maximum voltage from the piezo-harvester located on free end of the beam the piezo-actuator should be located on the beam in distance of 225 mm from the fixed end. Further experimental investigations carried out at the stand lab are shown in Fig. 5 and allow to verify this actuator location on the beam.

5. EXPERIMENTAL INVESTIGATIONS

The active cantilever beam has been experimentally investigated. For this purpose the laboratory stand consists of a steel beam with piezo-actuator QP20N, piezo harvester V21BL with energy harvester power condition system EHE004 is used. In order to drive the piezo-actuator the bipolar amplifier Piezo-mechanik SVRbip/150 is used. On the other hand in order to measure the vibration of the beam the laser sensor LQG1O65PUQ is used.
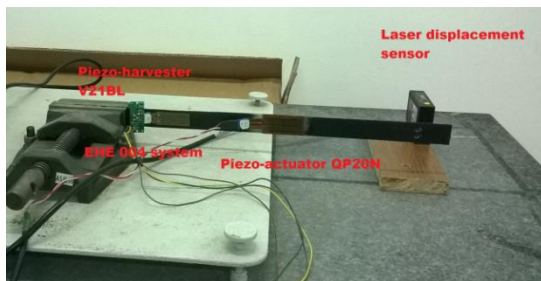
Fig. 5. Photo of the stand lab with the piezoelectric beam

The experimental investigations also were carried out in two steps. In the first step the beam was investigated in the frequency domain in order to validate the obtained results in a computer simulation. For this purpose a chirp signal as a signal excitation in following form $u(t) = 5sin(\omega t)$ in selected frequency range from 5 Hz to 450 Hz is generated from Digital Signal Analyzer (DSA). Then, the amplified periodic signal $u(t)$ is applied to the piezo-stripe actuator and in the same time the vibration of the beam is measured by the laser sensor. As a result of these investigations the frequency response of the beam is obtained which is shown in Fig. 6. The connection scheme of the laboratory stand during frequency response measurement is shown in Fig. 7.

Taking into account the obtained experimental Bode plot of the piezoelectric beam and Tab. 2 it can be noticed that only first two lowest natural frequencies are close to frequencies with simulations. Therefore, in order to proper excite of the beam to vibration is used analyser DSA which allows to generate sinusoidal signal $u(t)$ with natural frequency equal f_1=7.07[Hz], f_2=46.4 [Hz] or f_3=141.9 [Hz]. In results of these excitations the part of mechanical energy is converted to electric energy by used piezo-harvester V21B located on free-end of the beam and next converted with AC to DC by an energy harvester power condition (EHPC) system type of EHE004 which is also located on the beam. The scheme of this converter is shown in Fig. 8.

In results of this conversion voltage with AC to DC was possible its measured and recorded. As we can see in Figs. 9-11 the measurements of voltage in the capacitor are carried out for the three lowest natural frequencies of the beam.
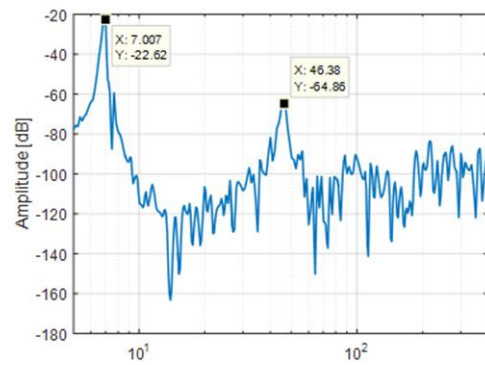

Fig. 6. Experimental Bode plot of the displacement's cantilever beam with the piezo-actuator QP10N and the piezo-harvester V21B
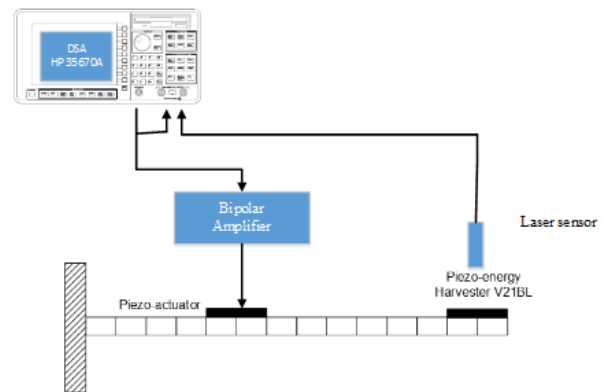

Fig. 7. Schematic diagram of the stand lab to determine modal parameters of the beam
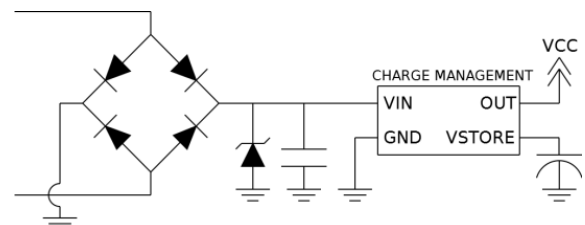

Fig. 8. The energy harvester power condition system type of EHE004. The VIN denotes input voltage, the GND denotes ground, the VSTORE denotes voltage stored in an embedded capacitor C=200 μF, and the OUT - output voltage (VCC)
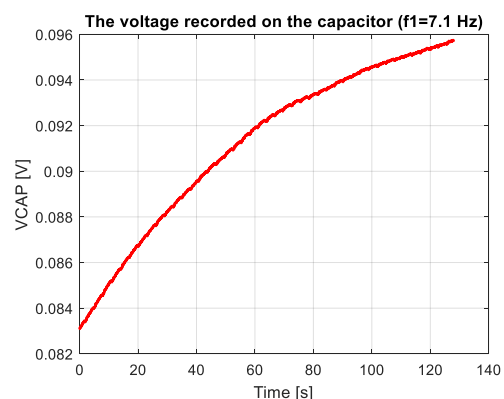

Fig. 9. The voltage stored on the capacitor for the first natural frequency of the beam (f_1=7.07 Hz)
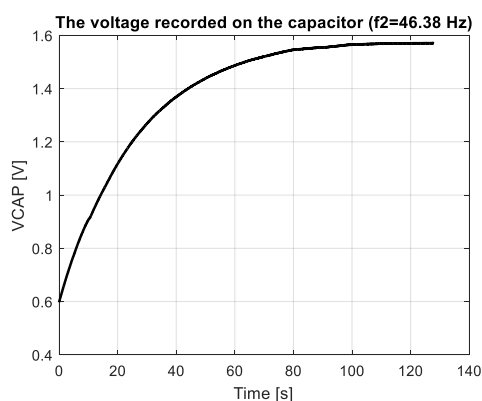
Fig. 10. The voltage stored on the capacitor for the second natural frequency of the beam (f_2=46.4 Hz)
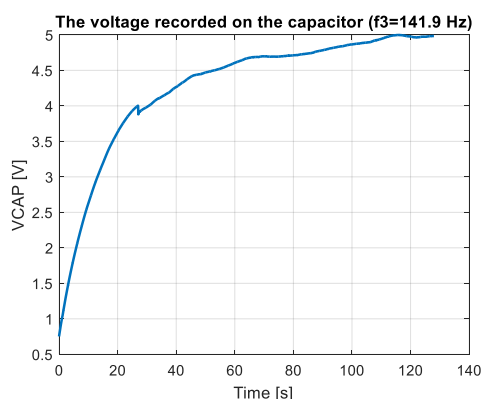

Fig. 11. The voltage stored on the capacitor for third natural frequency of the beam (f_3=141.9 Hz)

Taking into account recorded voltage it can be noticed that excitation to vibration of the beam with the first natural frequency is unsatisfying, because the measured voltage from piezo harvester very slowly increase to a value of approximately 7 mV. Similar behaviour can be seen when the beam is excited to vibration with second natural frequency. Then, the measured voltage on the capacitor achieved only 0.7 V after long time of oscillation. Finally, the best results are obtained during vibration of the beam with third natural frequency. In this case the recorded voltage from EH element achieved value equals 1.2 V. This level of voltage may supply for example a red LED type diode.

6. SUMMARY AND CONCLUSION

The paper shows modelling and testing of the cantilever beam with glued onto its surface two piezoelectric elements work as actuator and harvester. The process of harvesting energy from vibration of the beam was carried out in three steps. In the first step consider piezoelectric beam is analytically analyzed in order to show its electro-mechanical behavior. Next, based on the simulation results the modal parameters of the beam are calculated by using of Ansys software. The obtained results allowed to determining optimal location of the piezo-actuator where the piezo generates maximal modal control forces.

The last step of investigations has been related with experimental testing of the beam on the stand lab. In result of proper excitation of the beam to vibration with using Dynamical Signal Analyzer was possible measure and record the voltage derived

from the harvester and verified results obtained in simulations. The results with Figs. 9-11 shown cases achieve of maximal and minimal voltage derived from the capacitor mounted on the EHPC system. Summary obtained results we can notice that exist strongly coupling between mechanical part of the system expressed in form of modal control forces and electrical part - voltage generated by the piezo-harvester. Approach described in the paper leads to design of vibration control system with using fuzzy-logic controller which ensures obtain the highest indicator of harvesting energy from excited to vibration the beam in selected frequency range. Results of this investigations will describe in further paper.

REFERENCES

1. **Anton S.R.**, **Sodano H.A.** (2007), A review of power harvesting using piezoelectric materials, *Smart Materials and Structures*, 16, 1-21.
2. **Arnold D**. (2007), *Review of microscale magnetic power generation*, IEEE Transactions on Magnetics, 43, 3940-3951.
3. **Bai Y., Havranek P., Tofel P., Button T.W.** (2015) Nonlinear piezoelectric devices for broadband air-flow energy harvesting, *The European Physical Journal Special Topics*, 224, 2675-2685.
4. **Borowiec M.** (2015), Energy harvesting of cantilever beam system with linear and nonlinear piezoelectric model, *The European Physical Journal Special Topics*, 224, 2771-2785.
5. **Chen S.N., Wang G.J., Chien M.C.** (2006), Analytical modeling of piezoelectric vibration-induced micro power generator, *Mechatronics*, 16, 387-397.
6. **Friswell M.I., Ali S.F., Adhikari S., Lees A.W., Bilgen O., Litak G.** (2012), Nonlinear piezoelectric vibration energy harvesting from a vertical cantilever beam with tip mass, *Journal of Intelligent Material Systems and Structures,* 23, 1505-1521.
7. **Gosiewski Z., Koszewnik A**. (2007), Modeling of beam as control plane for vibration control system, *Solid State Phenomena*, 144, 59-64.
8. **Kelly S**.G. (2007), *Advanced Vibration Analysis*, CRC Press.
9. **Koszewnik A., Grześ P., Walendziuk W.** (2015*),* Mechanical and electrical impedance matching in a piezoelectric beam for energy harvesting, *The European Physical Journal Special Topics*, 224, 2719-2731.
10. **Priya S., Inman D.J.** (2009), *Energy harvesting technologies*, Springer Verlag, New York.
11. **Roundy S., Wright P.K., Rabaey J.** (2002), Micro-electrostatic vibration-to-electricity converters, *Proceedings of the ASME 2002 International Mechanical Engineering Congress and Exposition.*
12. **Sodano H., Inman D., Park G.** (2005), Generation and storage of electricity from power harvesting devices, *Journal of Intelligent Material Systems and Structures*, 16, 67-75.
13. **Shu Y.C., Lien I.C.** (2006), Analysis of power output for piezoelectric energy harvesting systems, *Smart Materials and Structures,* 15, 1499-1512.
14. **Tan D., Leng Y.G., Gao Y.J.** (2015) Magnetic force of piezoelectric cantilever energy harvesters with external magnetic field, The *European Physical Journal Special Topics*, 224, 2839-2853.
15. **Williams C.B., Yates R.B.** (1996), Analysis of a micro-electric generator for microsystems, *Sensors and Actuators*, 52, 8-11.

STUDY OF SELECTED PROPERTIES OF THERMALLY SPRAYED COATINGS CONTAINING WC AND WB HARD PARTICLES

Janette BREZINOVÁ[*], Anna GUZANOVÁ[*], Dagmar DRAGANOVSKÁ[*], Pavlo O. MARUSCHAK[**], Mariana LANDOVÁ[*]

[*]Faculty of Mechanical Engineering, Department of Mechanical Technology and Materials,
Technical University of Košice, Mäsiarska 74, 040 01 Košice, Slovakia
[**]Faculty of Computer Technologies, Department of Automation of Technological Processes and Productions,
Ternopil Ivan Pul'uj National Technical University, Ruska str., 56, Ternopil, Ukraine

janette.brezinova@tuke.sk, anna.guzanova@tuke.sk, dagmar.draganovska@tuke.sk,
maruschak.tu.edu@gmail.com, mariana.landova@tuke.sk

Abstract: The paper presents results of research of the essential characteristics of two kinds of advanced coatings applied by HVOF technology. One studied coating: WB-WC-Co (60-30-10%) contains two types of hard particles (WC and WB), the second coating is eco-friendly alternative to the previously used WC-based coatings, called "green carbides" with the composition WC-FeCrAl (85-15%). In green carbides coating the heavy metals (Co, Ni, NiCr) forming the binding matrix in conventional wear-resistant coatings are replaced by more environmentally friendly matrix based on FeCrAl alloy. On the coatings was carried out: metallographic analysis, measurement of thickness, micro-hardness, adhesion, resistance to thermal cyclic loading and adhesive wear resistance (pin-on-disk test). One thermal cycle consisted of heating the coatings to 600°C, dwell for 10 minutes, and subsequently cooling on the still air. The number of thermal cycles: 10. The base material was stainless steel AISI 316L, pretreatment prior to application of the coating: blasting with white corundum, application device JP-5000.

Key words: Coating, HVOF Technology, Adhesion, Friction Coefficient, Thermal Loading

1. INTRODUCTION

The components of production machines in technical practice are stressed by various operating conditions (transmitted forces, pressures, temperature, environment, etc.). By the influence of these diverse effects, in the majority of machines and their components stresses occurs, which causes unwanted damage of the surface (wear, deformation, corrosion, cracks, fractures etc.). To avoid substantial damage of surfaces of machinery components, there have been developed various methods of forming protective layers, resistant to operating conditions. Thermal spraying technology also belongs to such methods. Coatings formed using thermal spraying technology for its high hardness and wear resistance even at higher operating temperatures are often applied in many fields of industry, especially in automotive, aerospace, energy, engineering, manufacturing and mining industry.

Recently, just cermet coatings containing hard WC particles in metallic matrix applied using HVOF (High Velocity Oxygen Fuel) technology was seen as a less dangerous and more environmentally friendly alternative to hard chrome plating (Bolelli, 2012). Because the WC-based powders contain heavy metals such as Co and Ni (Brezinova et al., 2015; Aw and Tan, 2006; Żórawski, 2013; Sahraoui et al., 2010; Saha et al., 2011; Wood, 2010; Hulka et al., 2011; Hong et al., 2013a, b; Santana et al., 2008; Berget et al., 2007; Mati et al., 2007; Zavareh et al., 2015; Kaur et al., 2009), there is very strict logistics of powders used for coatings formation in the HVOF process. Currently, effort of materials scientists is focused on developing new powders, in which

these elements in metallic matrix is eliminated and are replaced by other alloys. One of them is the powder WC-FeCrAl, called "green carbides".

The aim of the experiment was to evaluate the characteristics of the two types of coatings containing hard carbide particles in Co and also in Co-free matrix with respect to their tribological properties in atmosphere and in a corrosive environment (Brezinova et al., 2011, 2012, 2013).

2. MATERIALS AND METHODS

The base material for production of test samples was stainless steel AISI 316L. The test samples were of a cylindrical shape with a diameter of 25 mm and a length of 70 mm. The coatings were applied to the front area of the cylinder. Before powder spraying the base material was abrasive blast cleaned using white aluminum oxide with grain size of 0.56 mm, air pressure of 0.4 MPa, blasting angle of 90° and a blasting distance of 300 mm (Brezinova et al., 2015; Staia et al., 2000). The coating was applied by HVOF technology using TAFA JP-5000 spraying system under spraying parameters recommended by the powder manufacturer.
Powders used:
— WC-WB-Co (60/30/10), agglomerated and sintered, grain size +15/-45 μm, used for wear and corrosion protection in molten metal (for Zn bath rolls in Continuous Galvanizing Lines),
— WC-FeCrAl (85/15), agglomerated and sintered, grain size +15/-45 μm, wear resistant coating with Ni- and Co-free metallic binder, replacement for WC-Co or WC-Ni.

The quality and thickness of coatings were assessed on metallographic sections using light and electron microscopy. The microhardness of the coatings was evaluated also on the metallographic sections (HV 0.1, 15 s)

The coatings were evaluated as-sprayed and after thermal cycles. One thermal cycle consisted of heating to 600 °C, dwell time of 10 min in furnace, followed by natural air cooling at room temperature. The number of cycles: 5 and 10.

Adhesion of coatings was determined by pull-off test (using 2K adhesive Loctite 9497) and wear resistance of coatings by pin-on-disc test (load 1.5 N, velocity 0.02 m.s^{-1}, duration of test 60 min, environment: atmosphere and immersion in 1 M NaCl solution, a static counterpart SiC ball).

3. RESULTS AND DISCUSSION

The thickness of the coatings was evaluated on several metallographic cross-sections. The cross-section of the coatings displayed by means of light microscopy (LM) is shown in Fig. 1. There the thickness of the coatings can be seen.
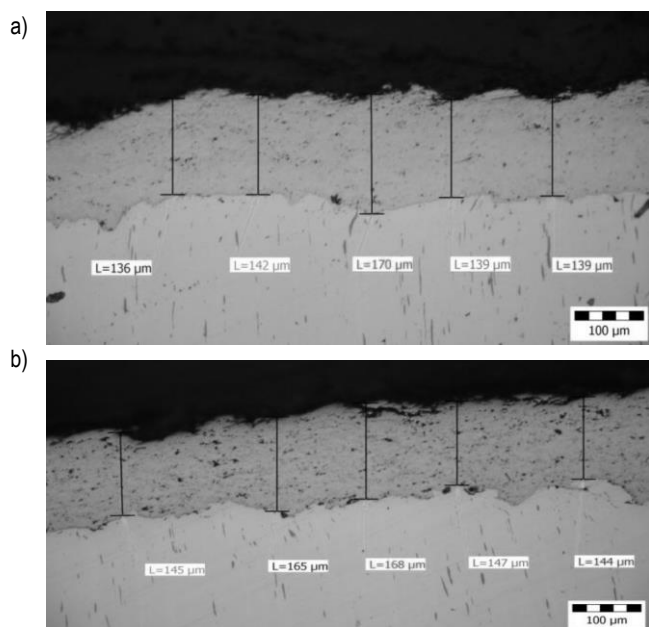

Fig. 1. Metallography section of the coatings: a) WC-WB-Co,
b) WC-FeCrAl, LM

There is is a visible interface between the substrate and the coating in Fig. 1. The interface is broken, corresponding to profile of surface after grit blasting. The coating good fills all valleys in the surface, in the interface are not present any defects. The coatings are well anchored in surface irregularities. Average coatings thickness varies from 145 to 174 μm.

More detailed analyses of the structure of coatings were performed using SEM. The microstructure of the coating at magnification 5000× is showed in Fig. 2.

The coating WB-WC-Co consists of two types of hard particles (WC and WB) in soft binding Co matrix which ensures the coherence of carbides. The coating WC-FeCrAl contains hard particles of WC in a matrix based on FeCrAl alloy. Results of EDX analysis of chemical composition of coatings as-sprayed and also after thermal cycles are shown in Fig. 3.
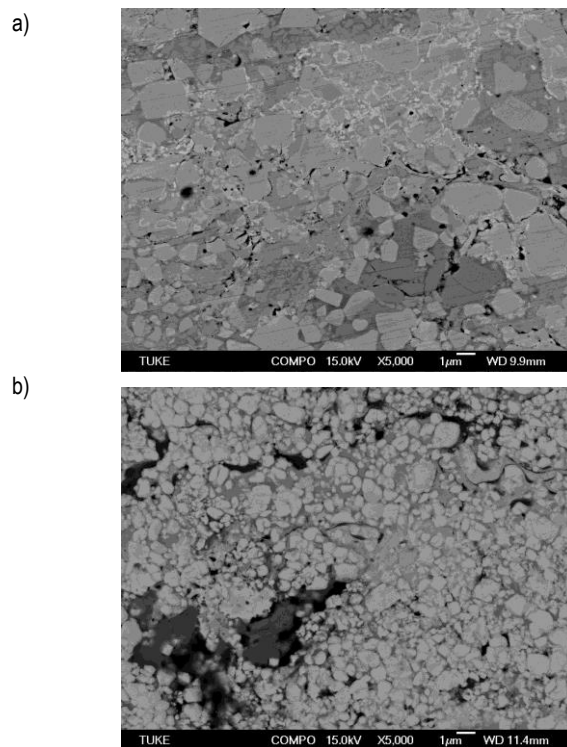

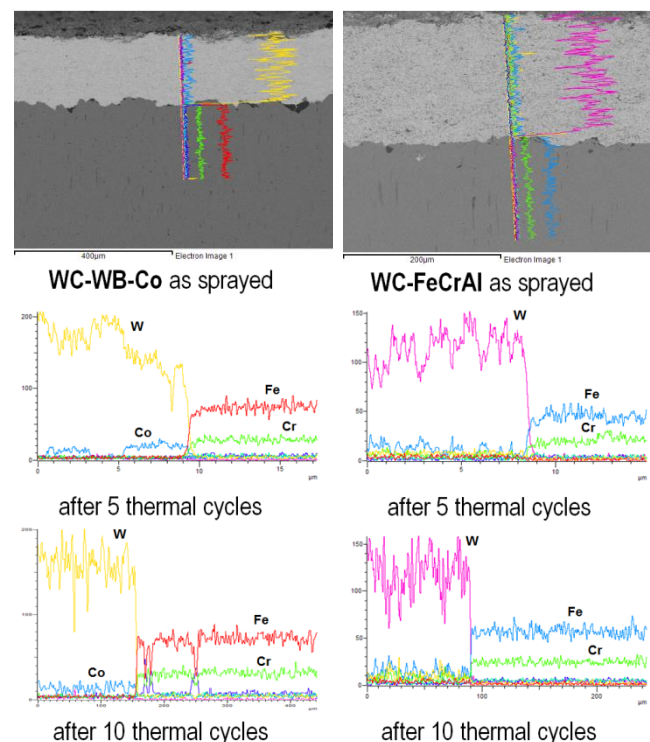**Fig. 2.** SEM image of the coatings: a) WC-WB-Co, b) WC-FeCrA

Fig. 3. EDX line scan composition profiles

Results showed that there are no changes in chemical composition of the coatings caused by thermal cyclic load.

The hardness of the coating WC-WB-Co was found between 1200 and 1300 HV 0.1 and hardness of coating WC-FeCrAl between 1000 and 1100 HV 0.1. Adhesion of both coatings as sprayed, or after thermal cyclic loading exceeded the cohesive strength of the adhesive used (>50 MPa). The results of determination of thickness, hardness, and adhesion of coatings are summarized in Tab. 1.

Janette Brezinová, Anna Guzanová, Dagmar Draganovská, Pavlo O. Maruschak, Mariana Landová
Study of Selected Properties of Thermally Sprayed Coatings Containing WC and WB Hard Particles

DOI 10.1515/ama-2016-0046

Tab.1. Results of the tests

WC-WB-Co			
Number of thermal cycles	0 (as sprayed)	5	10
Thickness / µm	145	151	160
Hardness HV0.1	1303	1325	1229
Adhesion / MPa	>56	>51	>50
WC-FeCrAl			
Thickness / µm	165	157	174
Hardness HV0.1	1075	1050	1069
Adhesion / MPa	>50	>56	>54

Wear resistance of coatings as-sprayed and after the thermal cycles was evaluated by pin-on-disk test under dry friction conditions in the atmosphere and also immersed in the NaCl solution. The course of the friction coefficient during pin-on-disc test states Fig. 4.
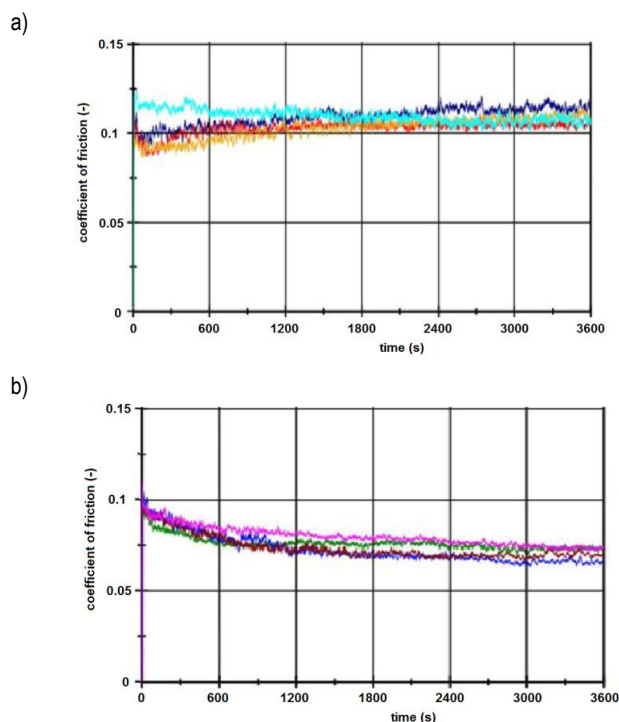
a)

b)

Fig. 4. Friction coefficient of the coatings after 5 and 10 thermal cycles in the atmosphere a) and in NaCl solution b)

Friction coefficient of the coatings in the atmosphere after the initial start-up became stabilized at a value of 0.1, and immersed in NaCl solution was stabilized below 0.1. During adhesive friction test in corrosive solution, the coefficient of friction stabilized at a lower value than in atmosphere.

The appearance of the coatings surface in wear track and out of wear track is shown in Fig. 5.

Weight loss of coatings after pin-on-disk test was minimal so could not be determined although the resolution of the balance was 10 to the negative 4th power [g], as confirmed also appearance of wear track. Surface of coatings in wear track and out of wear the track is almost identical, they are visible no signs of particles removed from coating material. Conversely, on the static counterpart was found visible loss of material, Fig. 6.

Material loss of each static counterpart is the same, judging by size of wear area - there are no differences between friction pairs as sprayed and after thermal cycling, as well as no differences between tests in the atmosphere and NaCl solution.
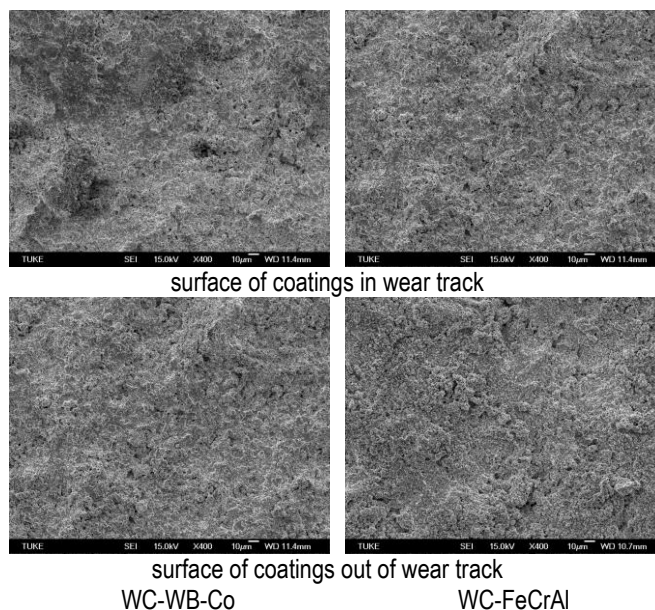

surface of coatings in wear track

surface of coatings out of wear track

WC-WB-Co   WC-FeCrAl

Fig. 5. Surface of the coatings in wear track and out of wear track

after 5 thermal cycles

after 10 thermal cycles
after contact with **WC-WB-Co**

after 5 thermal cycles

after 10 thermal cycles
atmosphere   NaCl
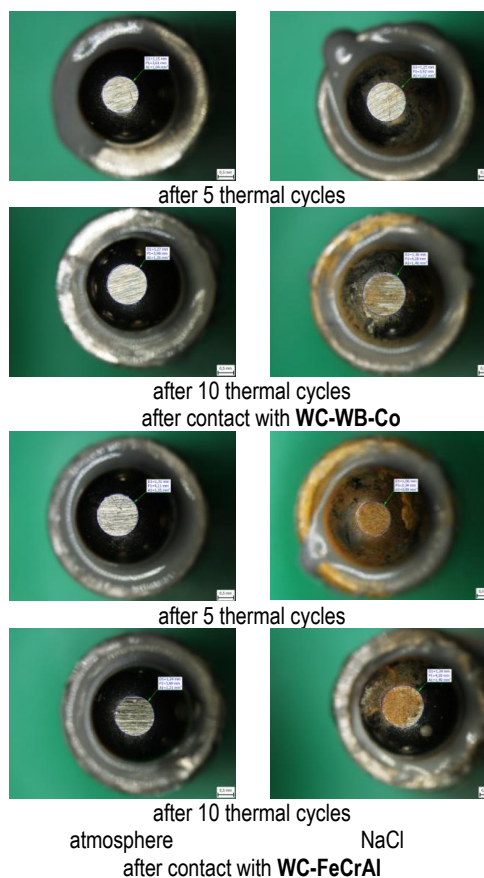after contact with **WC-FeCrAl**

Fig. 6. Appearance of static balls

On the surface of static balls used in NaCl solution corrosion products are present.

4. RESULTS

Both coatings exhibited comparable properties as for thickness (140-170 µm), hardness (1300 and 1050 HV0.1), adhesion (> 50 MPa), and also in terms of adhesive wear resistance (non-measurable weight loss, low friction coefficient: 0.1 in the atmosphere and also in NaCl solution). It can be concluded that "green carbides" coating is environmentally more friendly replacement for coatings containing Co and Ni without reducing the performance of the coating.

REFERENCES

1. **Aw P.K., Tan B.H.** (2006), Study of microstructure, phase and microhardness distribution of HVOF sprayed multi-modal structured and conventional WC–17Co coatings, *Journal of Materials Processing Technology*, 174(1-3), 305–311.
2. **Berget J., Rogne T., Bardal E.** (2007), Erosion–corrosion properties of different WC–Co–Cr coatings deposited by the HVOF process—influence of metallic matrix composition and spray powder size distribution, *Surface and Coatings Technology*, 201(18), 7619–7625.
3. **Bolelli G., Börner T., Bozza F., Cannillo V., Cirillo G., Lusvarghi L.** (2012), Cermet coatings with Fe-based matrix as alternative to WC–CoCr: Mechanical and tribological behaviours, S*urface and Coatings Technology*, 206(19-20), 4079–4094.
4. **Brezinová J., Guzanová A.** (2012), Possibilities of utilization high velocity oxygen fuel (HVOF) coatings in conditions of thermal cyclic loading, *Metalurgija*, 51(2), 211-215.
5. **Brezinová J., Guzanová A., Draganovská D.** (2015a), *Abrasive blast cleaning and its application*, 1st. Ed., Pfaffikon: Trans Tech Publications.
6. **Brezinová J., Guzanová A., Draganovská D., Bronček J.** (2015b), Quality evaluation of HVOF coatings on the basis of WC-Co in tribocorrosive conditions, *Materials Science Forum*, 811, 63-66.
7. **Brezinová J., Guzanová A., Draganovská D., Egri M.** (2013), Assessment tribological properties of coatings applied by HVOF technology, *Acta Mechanica et Automatica*, 7(3), 135-139.
8. **Brezinová J., Guzanová A., Egri M.** (2012), Change in properties of HVOF coatings under conditions of thermal cyclic loading, *Chemické listy*, 106(S3), 383-386.
9. **Brezinová J., Guzanová A., Egri M., Malejčík J.** (2011), Evaluation of thermal sprayed coatings properties in terms of erosive wear, *Chemické listy: special issue*, 105(17), 775-776.
10. **Hong S., Wu Y., Wang Q., Ying G., Li G., Gao W., Wang B., Guo W.** (2013a), Microstructure and cavitation–silt erosion behavior of high-velocity oxygen–fuel (HVOF) sprayed Cr3C2–NiCr coating, *Surface and Coatings Technology*, 225, 85–91.
11. **Hong S., Wu Y., Zheng Y., Wang B., Gao W., Lin J.** (2013b), Microstructure and electrochemical properties of nanostructured WC–10Co–4Cr coating prepared by HVOF spraying, *Surface and Coatings Technology*, 235, 582–588.
12. **Hulka I., Uţu D., Şerban V.A.** (2011), Micro-scale sliding wear behavior of HVOF sprayed WC-Co(Cr), *Annals of Faculty Engineering Hunedoara – International Journal of Engineering*, 9(2), 61-64.
13. **Kaur M., Singh H., Prakash S.** (2009), High-Temperature Corrosion Studies of HVOF-Sprayed Cr3C2-NiCr Coating on SAE-347H boiler steel, *Journal of Thermal Spray Technology*, 18(4), 619-632.
14. **Maiti A.K., Mukhopadhyay N., Raman R.** (2007), Effect of adding WC powder to the feedstock of WC–Co–Cr based HVOF coating and its impact on erosion and abrasion resistance, *Surface and Coatings Technology*, 201(18), 7781–7788.
15. **Saha G.C., Khan T.I., Zhang G.A.** (2011), Erosion–corrosion resistance of microcrystalline and near-nanocrystalline WC–17Co high velocity oxy-fuel thermal spray coatings, *Corrosion Science*, 53(6), 2106–2114.
16. **Sahraoui T., Guessasma S., Jeridane M. A., Hadji M.** (2010), HVOF sprayed WC–Co coatings: Microstructure, mechanical properties and friction moment prediction, *Materials and Design*, 31(3), 1431 – 1437.
17. **Santana Y.Y., La Barbera-Sosa J.G., Caro J., Puchi-Cabrera E.S., Staia M.H.** (2008), Mechanical properties and microstructure of WC–10Co–4Cr and WC–12Co thermal spray coatings deposited by HVOF, *Surface Engineering*, 24(5), 374-382.
18. **Staia M.H., Ramos E., Carrasquero A., Roman A., Lesage J., Chicot D., Mesmacque G.** (2000), Effect of substrate roughness induced by gritblasting upon adhesion of WC-17%Co thermal sprayed coatings, *Thin Solid Films*, 377-378, 657-664.
19. **Wood R.J.K.** (2010), Tribology of thermal sprayed WC–Co coatings, *International Journal of Refractory Metals and Hard Materials*, 28(1), 82–94.
20. **Zavareh M.A., Sarhan A.A.D.M., Razak B.B.A., Basirun W.J.** (2015), The tribological and electrochemical behavior of HVOF-sprayed Cr3C2–NiCr ceramic coating on carbon steel, *Ceramics International*, 41(4), 5387–5396.
21. **Žórawski W.** (2013), The microstructure and tribological properties of liquid-fuel HVOF sprayed nanostructured WC–12Co coatings, *Surface and Coatings Technology*, 220, 276-281.

A STUDY OF THE PRELOAD FORCE IN METAL-ELASTOMER TORSION SPRINGS

Wojciech SIKORA[*], Krzysztof MICHALCZYK[*], Tomasz MACHNIEWICZ[**]

[*]Faculty of Mechanical Engineering and Robotics, Department of Machine Design and Technology,
AGH University of Science and Technology, al. Mickiewicza 30, 30-059 Kraków, Poland
[**]Faculty of Mechanical Engineering and Robotics, Department of Strength and Fatigue of Materials and Structures,
AGH University of Science and Technology, al. Mickiewicza 30, 30-059 Kraków, Poland

wosikora@agh.edu.pl, kmichal@agh.edu.pl, machniew@agh.edu.pl

Abstract: Neidhart type suspension units composed of metal-elastomer torsion springs can be a good alternative to steel helical springs in applications such as vibration absorbers or vehicle suspension systems. Assembling this type of spring requires initial preload of the elastomeric working elements, which determines their operating properties. The results of experimental tests and numerical simulations concerning the preload of elastomeric working elements in Neidhart type suspension units are presented in the paper. The performed research made it possible to propose a new calculation model for determining the preload force value acting on the elastomeric cylindrical elements applied in this type of suspension unit. The results obtained using the proposed model exhibit good convergence with FEM simulation results within the range of the tested geometrical and material properties.

Key words: Hyperelastic Materials, Neidhart Spring, Metal-Elastomer Spring

1. INTRODUCTION

Metal-elastomer elastic joints exhibit, as opposed to metal springs, good damping properties, which is the reason behind their wide application in vibration reduction systems or rotating machinery suspension systems, among others. Generally, this type of joint consists of rectangular shaped elastomeric elements bonded to rigid plates (Gent et al., 2007). However, such a construction has significant limitations, because, in the case of compression loading, nonuniform stress distribution in elastomeric elements causes a risk of extensive heat generation (Banić et al., 2012), stress concentration and, as a result, damage of the element. These phenomena are the reasons why, in the design practice for vibration isolators, deformations of compression-loaded elastomeric elements are limited to about 10-15% of the elastomeric component thickness (Rivin, 2003). Significantly preferable stress distributions can be obtained when an elastomeric element has a cylindrical shape and is loaded radially by two rigid plates (Neidhart R., 1969). Rivin and Lee demonstrated, by means of experiment (1994) and by numerical calculations (1996), that elastic joints of such a construction can withstand deformations in the compression mode even as high as 40%, without the risk of the unfavorable phenomena described above. An example of the practical application of such a construction is the Lastosphere vibration isolator, produced for many years by the Lord Corporation.

It should be noted, however, that these structures were not able to compete with coil springs in terms of the maximum achievable deformation. Only the metal-elastomer torsion joint patented by Hermann Neidhart and its later modifications have made it possible to obtain deformations characteristic for helical springs, and damping properties characteristic for rubber-like materials.

The construction of a metal-elastomer torsion spring, called – from the name of its inventor – a Neidhart spring, was patented in 1955 (Neidhart H., 1955) and was a development of structures applied earlier in vehicle suspension systems. Over the years, the number of applications of Neidhart springs has increased and the field of their utilization also include the examples outside the automotive industry. Currently, among the numerous examples of this solution's applications, supports of vibrating machinery (vibrating screens, vibrating conveyors), belt and chain tensioners, vibration isolators, pressure rollers and so on can be mentioned (Fig.1).
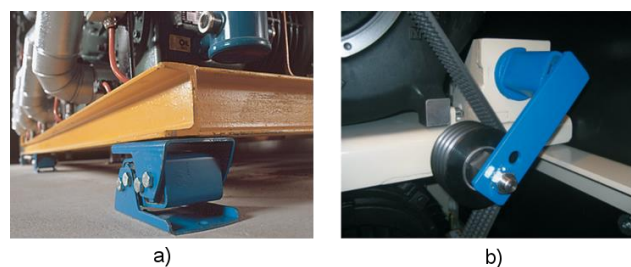

Fig.1. Examples of typical applications of Neidhart springs: a) vibration isolation; b) transmission belt tensioner (http://www.rosta.ch)

Although Neidhart springs have been used for more than six decades, no extensive analysis of this construction can be found in the literature (Wodziński, 2003). The current situation is not conducive to the popularization of this solution, due to the lack of information concerning the rules for designing such springs and the influence of geometrical and material parameters on their operating properties. The static and dynamic properties of metal-rubber torsion springs depend on their geometry and the composi-

tion of the rubber compound (Samaca Martinez et al., 2013; Hassan et al., 2012; Chokanandsombat and Sirisinha, 2013) used to manufacture working cylinders. By making modifications in these two fields, one can obtain such spring properties that are most suitable in certain applications. Therefore, the article shows the results of experimental tests conducted in order to define the characteristics of rubber compounds used to produce the working elements of the tested springs. In the second part of the article, the relation between dimensions of the spring elements and the lateral force required to exert initial deformation of rubber cylinders is developed. There are, to the knowledge of the authors, no such formulas available in the literature that would allow one to approximate the relation between the geometric parameters of Neidhart type springs and assembly preload force. Knowledge of this force may be utilized in the design process of springs with specified reaction torque characteristics.

The aim of the study is to analyze the influence of the geometrical and material parameters of metal-elastomer torsion springs on the value of the preload reaction force between the rigid metal elements of the spring and elastomeric working elements.

2. CONSTRUCTION OF NEIDHART SPRINGS

A typical Neidhart type spring consists of an outer square tube, inner square shaft and four cylindrical elastomeric elements that are mounted between the tube and shaft in such a way that the shaft is rotated with respect to the tube by 45°, as shown in Fig. 2. It can be seen in Fig. 2a that elastomeric cylinders are significantly compressed in a radial direction, which provides the initial preload of the spring.
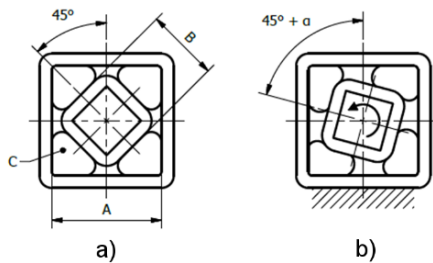

Fig.2. Construction of the metal-elastomer spring: a) unloaded spring; b) loaded spring; A – inner dimension of the square tube, B – outer dimension of the shaft, C – elastomeric working element

As shown in Fig. 2b, the spring transfers torsional loads, however, it can also withstand lateral loads. The angular movement of the shaft with respect to the tube should be limited to only about 30° due to the risk of unacceptably high deformation and strain of the elastomeric elements. The spring units shown in Fig. 2 can be mounted into sets as shown in Fig. 1a to transfer lateral movements.

3. HYPERELASTIC MATERIAL MODEL

Rubber, being an elastomer, is classified as a hyperelastic material. In the literature, one can find many models of such materials, of which the best known are the Neo-Hookean, Mooney-Rivlin, Arruda-Boyce and Ogden models (Bower, 2010; Boyce and Arruda, 2000; Kim et al., 2012). Besides the listed ones, due to significant differences in the properties of hyperelas-

tic materials, there are many other models that have been developed for specific groups of materials (Lu et al., 2010).

Elastomeric material models are usually presented as a function of the elastic strain energy density. This is a starting point to determine the stress in a given state of load. To determine the parameters of the elastomer material, the static test of axial tension, compression or shear of an appropriately shaped test sample should be performed on a material testing machine. The chosen material model parameters can be obtained by fitting the theoretical curve to the experimental one.

The Mooney-Rivlin model (Mooney, 1940; Rivlin, 1948; Baranowski et al., 2012) is utilized in this paper. In this model, the strain energy density function U can be expressed in the form (Bower, 2010):

$$U(\overline{I_1}, \overline{I_2}) = C_{10} \cdot (\overline{I_1} - 3) + C_{01} \cdot (\overline{I_2} - 3) \\ + D_1 \cdot (J - 1)^2 \tag{1}$$

where: C_{10}, C_{01}, D_1 – material constants in MPa.

$$\overline{I_1} = J^{-2/3} \cdot I_1$$
$$\overline{I_2} = J^{-4/3} \cdot I_2$$

where: I_1, I_2 – invariants of the left Cauchy-Green tensor **B**.

$$\mathbf{B} = \mathbf{F} \cdot \mathbf{F}^T = \begin{bmatrix} \lambda_1{}^2 & 0 & 0 \\ 0 & \lambda_2{}^2 & 0 \\ 0 & 0 & \lambda_3{}^2 \end{bmatrix}$$

$$I_1 = tr(\mathbf{B}) = \lambda_1{}^2 + \lambda_2{}^2 + \lambda_3{}^2$$

$$I_2 = \frac{1}{2}[(tr\,\mathbf{B})^2 - tr\,(\mathbf{B}^2)] = \lambda_1{}^2\lambda_2{}^2 + \lambda_2{}^2\lambda_3{}^2 + \lambda_3{}^2\lambda_1{}^2$$

$$\mathbf{F} = \begin{bmatrix} \lambda_1 & 0 & 0 \\ 0 & \lambda_2 & 0 \\ 0 & 0 & \lambda_3 \end{bmatrix}$$

$$J = det(\mathbf{F}) = \lambda_1 \cdot \lambda_2 \cdot \lambda_3$$

where: **F** – deformation gradient tensor, $\lambda_1, \lambda_2, \lambda_3$ – principal stretches.
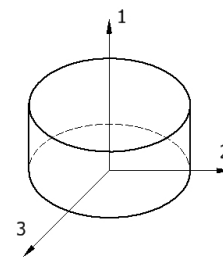

Fig. 3. Coordinate system for a cylindrical sample

Material testing of the rubber samples was based on an uniaxial compression test in direction 1 (Fig. 3). For such a case, it can be assumed that $\lambda_2 = \lambda_3$:

$$\lambda_2 = \lambda_3 = \sqrt{\frac{J}{\lambda_1}} = \sqrt{\frac{J}{\lambda}}$$

$$\lambda_1 = \lambda$$

To simplify the material model, a specimen was treated as being made from an incompressible material thus $J = 1$. This assumption is very close to reality in the case of rubber. True princi-

DE GRUYTER
OPEN

Wojciech Sikora, Krzysztof Michalczyk, Tomasz Machniewicz
A Study of the Preload Force in Metal-Elastomer Torsion Springs

DOI 10.1515/ama-2016-0047

pal stresses can be obtained from the formulas presented below (Bower, 2010):

$$\widetilde{\sigma_{ij}} = 2\left[\left(\frac{\partial U}{\partial I_1} + I_1\frac{\partial U}{\partial I_2}\right)B_{ij} - \left(I_1\frac{\partial U}{\partial I_1} + 2I_2\frac{\partial U}{\partial I_2}\right)\frac{\delta_{ij}}{3}\right.$$
$$\left. - \frac{\partial U}{\partial I_2}B_{ik}B_{kj}\right] + p\delta_{ij}$$

$$\widetilde{\sigma_{11}} = \frac{4}{3}\left[C_{10}\cdot\left(\lambda^2 - \frac{1}{\lambda}\right) + C_{01}\cdot\left(\lambda - \frac{1}{\lambda^2}\right)\right] + p$$

$$\widetilde{\sigma_{22}} = \widetilde{\sigma_{33}} = -\frac{2}{3}\left[C_{10}\cdot\left(\lambda^2 - \frac{1}{\lambda}\right) + C_{01}\cdot\left(\lambda - \frac{1}{\lambda^2}\right)\right] + p$$

$$p = \frac{\widetilde{\sigma_{11}} + \widetilde{\sigma_{22}} + \widetilde{\sigma_{33}}}{3}$$

Because the specimen sidewall is unconstrained therefore $\widetilde{\sigma_{22}} = \widetilde{\sigma_{33}} = 0$ and true stress in the direction of the compression axis is described by:

$$\widetilde{\sigma_{11}} = 2C_{10}\cdot\left(\lambda^2 - \frac{1}{\lambda}\right) + 2C_{01}\cdot\left(\lambda - \frac{1}{\lambda^2}\right) \tag{2}$$

After dividing both sides of (2) by λ, the engineering stress was obtained:

$$\sigma_{11} = 2C_{10}\cdot\left(\lambda - \frac{1}{\lambda^2}\right) + 2C_{01}\cdot\left(1 - \frac{1}{\lambda^3}\right) \tag{3}$$
$$\lambda = 1 + \varepsilon$$
$$\varepsilon = \frac{z - z_0}{z_0}$$

where (Fig. 4a): ε – strain, z_0 – initial sample height, z – sample height during test.

The relationship (3) for compressive stress on a central axis is necessary for determining the rubber material constants. Comparing equation (3) with the results obtained from a compression test would allow the values of C_{10} and C_{01} to be estimated.

4. ESTIMATION OF MATERIAL CONSTANTS

Experiments were carried out on an MTS 810 testing machine (Fig. 4c) and based on the ISO 7743 standard. Cylindrical samples were made of a chloroprene rubber CR with a diameter of 29 mm and length of 13 mm. Specimens were axially compressed under a strain control with the rate of 10 mm/min till the axial strain $\varepsilon \approx -0.3$ was reached. It corresponded with the absolute change in the height by $\Delta z \approx 4$ mm. Next the strain was relieved with the same rate. Contact surfaces between the sample and testing machine plates were coated with a lubricant. This allowed friction force to be reduced during a radial expansion of the material and prevented specimen deformation into a barrel shape during compression (Fig. 4b). The described loading cycle was repeated three times for each sample. In total, there were 15 samples. The relation between the stress and strain recorded during the single experiment is presented in Fig. 5. It shows an elastic hysteresis of the tested rubber. The compression curve changes during the experiment and stabilizes after the first loading cycle. The stress value at the maximum strain is reduced in the second cycle. The relaxation time of the compressed material is quite long, because stress increases in the second and third cycles can be observed for strains larger than $\varepsilon \approx 0,04$ which means that lasting deformations took place.
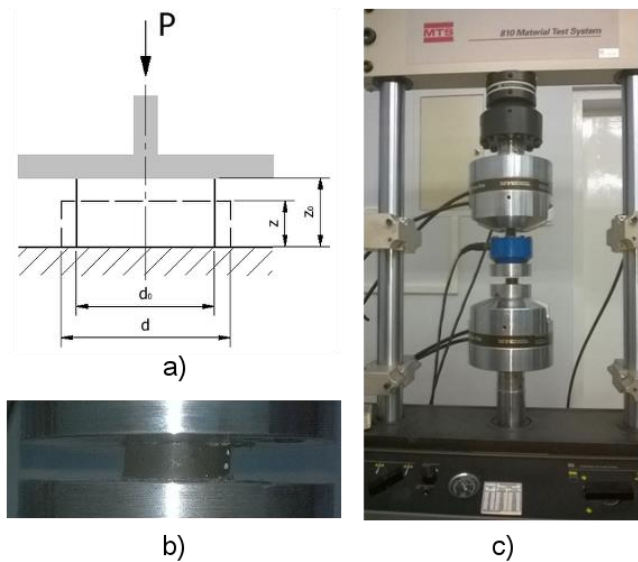

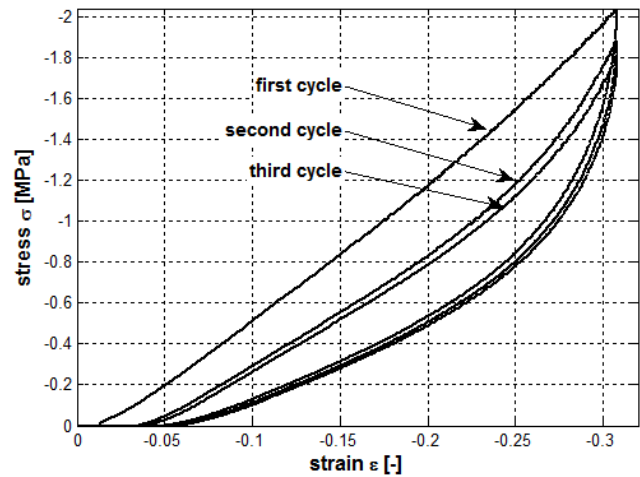Fig. 4. Experimental technique: a) specimen dimensions; b) specimen Ø29x13 during test, c) test stand

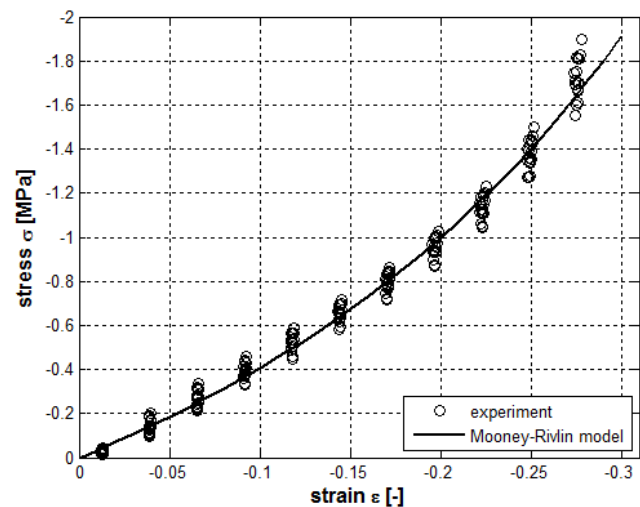Fig. 5. An example of an elastic histeresis for a tested rubber sample

Fig. 6. Comparison between Mooney-Rivlin model curve and experimental results for the compression test

Material constant estimations were based on the compression curve from the third loading cycle. The reason is that the last curve should be similar to a stabilised material compression response in the working spring. When the object of interest is the force needed for an initial deformation of the rubber cylinders directly during spring assembly, the curve from the first cycle should be used instead. The material constants C_{10} and C_{01} were determined using the least squares method by fitting function (3) to the experimental curves. For further analysis, the mean values of C_{10} and C_{01} from all 15 samples were used. Their values were equal to $C_{10}=0.2461$ and $C_{01}=0.3271$. In Fig. 6, a theoretical curve for the Mooney-Rivlin model was compared with the experimental results. Strain values visible in fig. 6 were shifted by $\varepsilon \approx 0.04$ compared to Fig. 5 due to the lasting deformation occurring in the third cycle.

5. SPRING ASSEMBLY PRELOAD FORCE

An elastic reaction force exerted by a single rubber cylinder in an unloaded Neidhart spring could be recreated by pushing a cylinder sample into the 90° V groove, as it is shown in Fig. 7. Considering only one rubber element instead of all four at the same time is possible because of the two symmetry planes that exist in the examined spring. Elastic deflection of the sample is described by the variable $\Delta h = h_0 - h$. For the compressed cylindrical sample of the dimensions Ø10x42 Δh is equal to ca. 3 mm, which corresponds to the deflection in typical Neidhart rubber springs.
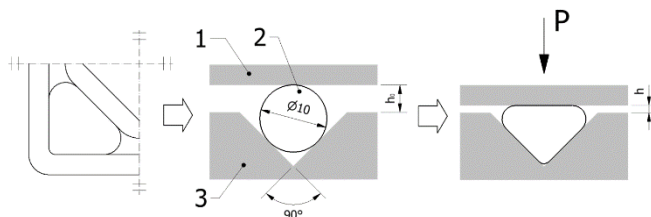

Fig. 7. Alternative setting for a quarter of Neidhart rubber spring:
1 – pressure plate, 2 – rubber cylinder, 3 – plate with groove

Fig. 8. Sample Ø10x42 on testing stand

The experiment was prepared and carried out to simulate the situation above. A cylindrical sample of the dimensions Ø10x42, placed horizontally in the V groove cut in the steel plate (Fig. 8), was compressed along its axis. The test was repeated for four samples on the same testing machine, like in the previous experiment. During the test, compression force and deflection Δh were recorded. Each sample underwent three identical loading cycles where Δh reached a maximum value of 3 mm. For further analysis, only the compression curve $P(\Delta h)$ from the last cycle, after stabilization of the sample response, was used.

6. FEM SIMULATIONS

Based on the previous experiment, the exact system was rec-

reated in the ANSYS 16 version FEM simulation program. The simulation model (Fig. 9) consists of two rigid bodies (grooved plate and pressure plate) and a deformable body (cylindrical rubber element). Material constants for the CR rubber necessary to carry out the simulation were assumed according to the mean values C_{10} and C_{01} presented in the earlier section. The existence of two symmetry planes in the model – longitudinal and transverse – allows only a quarter of the whole system to be recreated. In the place of the removed fragment, the symmetry boundary conditions have to be placed on specific surfaces. Thanks to this simplification, the computing resources and time needed for performing the simulation were reduced. The model of the single rubber cylinder visible in Fig. 9 was divided into 17,000 finite elements of the type SOLID285. On the section surfaces of each of the three parts, the symmetry condition was assigned. The grooved plate was fixed in place and loading was exerted by a pressure plate with displacement applied vertically. The force necessary for deformation of the sample by the given value ($\Delta h=3$ mm) was recorded as a reaction force on the pressure plate during the simulation.

A comparison of the simulation and experimental results is presented in Fig. 10. Similar progress of the compressive force as a function of Δh for FEM and experimental values allows one to assume that the prepared simulation reflects the actual physical process to a satisfactory degree. Consequently, it is justified to continue analysis for different geometrical dimensions of cylindrical samples, based further only on FEM simulations.
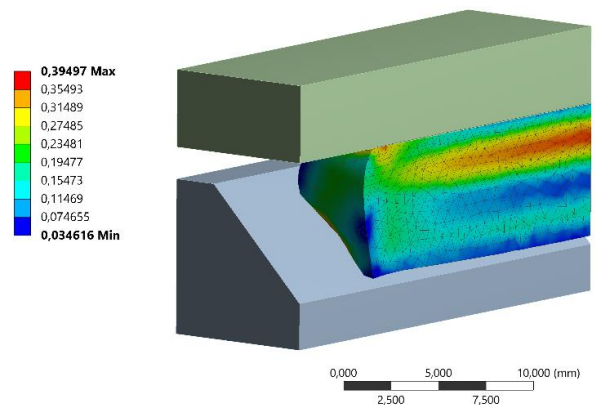

Fig. 9. FEM simulation of cylindrical sample compression. Results shown as maximum principal elastic strain of material
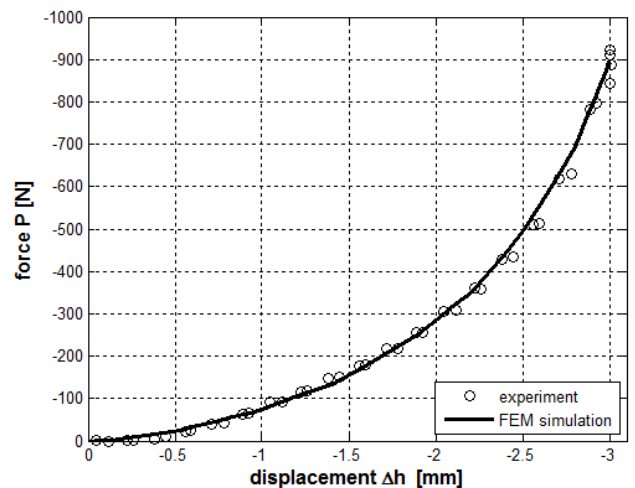

Fig. 10. Comparison of experimental results with the FEM simulation of pressing cylindrical rubber sample into groove

DE GRUYTER
OPEN

Wojciech Sikora, Krzysztof Michalczyk, Tomasz Machniewicz
A Study of the Preload Force in Metal-Elastomer Torsion Springs

DOI 10.1515/ama-2016-0047

The maximum amplitudes of the load for elastomeric parts are important in terms of their fatigue durability (Luo and Mortel, 2009). The maximum principal elastic strain of the sample is shown in Fig. 9. It can be used as a measure of the material equivalent load in complex loading situations (Mars and Fatemi, 2002). Analysing the distribution of the mentioned strain shows that the most loaded area is the sample interior near the contact with the pressure plate. Moreover, because of the material expansion along the groove, the face of the sample begins to bulge, which leads to the collapse of the face edge during contact between the sample and both plates. Increases in material load because of this are more significant for contact with the pressure plate.

7. RELATION BETWEEN RUBBER CYLINDER DIMENSIONS AND ELASTIC REACTION FORCE

The next step was an attempt to devise a functional relation between the force P resulting from an initial deformation of rubber cylinders in a Neidhart spring and their dimensions – diameter d and length L. For this purpose, FEM simulations were carried out for a limited range of cylinder dimensions. It was assumed that the diameters would fit in the range from 10 to 30 mm and length from 40 to 80 mm. Since the sample diameters are different compared to the ones that were tested earlier, it was necessary to define the value of Δh for other cases of diameter. It has been assumed that an elastic deflection Δh, being the result of an initial deformation of rubber cylinders, will be equal to 30% of the diameter size d:
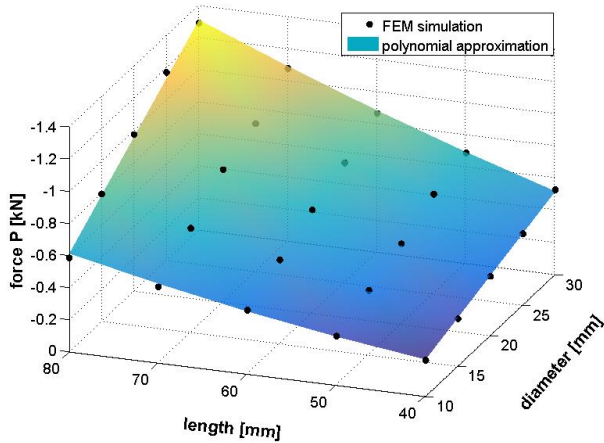
$$\Delta h = 0.3d$$

Fig. 11. FEM simulation results for compressive force P as a function of rubber cylinder diameter d and length L, and approximation of those results by the polynomial function

The proposed value corresponds to the initial deflection value in typical Neidhart springs. In total, 25 simulations were carried out for 5 values of diameter d and 5 values of length L from the range that was mentioned earlier. FEM simulation results are presented in the form of a 3D scatter plot in Fig. 11. It shows the values of the compressive force P for the initial deflection Δh=0.3d for given values of rubber cylinder dimensions.

Further, the obtained FEM results were approximated. The relation describing the compressive force P as a function of two variables P(d, L) was introduced as a polynomial function due to its versatility and ease of use in practical applications:

$$P(d,L) = \sum_{i+j=0}^{i+j=N} p_{ij}\, d^i\, L^j \tag{4}$$

where: $N = 2$, $i = \{0,1\}$, $j = \{0, 1, 2\}$.

After expanding (4) for given values of N, i and j, the result is:

$$P(d,L) = p_{00} + p_{10}\, d + p_{01}\, L + p_{11}\, d\, L + p_{02}\, L^2 \tag{5}$$

Following the approximation of FEM results, the polynomial coefficients presented below were obtained:

$$p_{00} = -155.6\, N$$

$$p_{10} = 6.02\, \frac{N}{mm}$$

$$p_{01} = 4.8\, \frac{N}{mm}$$

$$p_{11} = -0.51\, \frac{N}{mm^2}$$

$$p_{02} = -0.077\, \frac{N}{mm^2}$$

The correlation coefficient for data received from the FEM simulation and equation (5) was R^2=0.9967 and root mean square error RMSE=0.018. Function (5) for the given input of the rubber cylinder diameter and length allows the value of compressive force to be estimated, which is also the elastic reaction force needed for an initial deformation of the rubber cylinders used in Neidhart springs. This is presented as a surface plot in Fig. 11. The developed relationship applies only to elastic elements made of chloroprene rubber CR, whose material constants were estimated in this paper.

8. CONCLUSIONS

The elements to which a Neidhart spring owes its elastic properties are rubber cylinders. To analyse spring construction and operation, knowledge about the characteristics of the material used for cylinders is necessary. The conducted tests of axial compression for cylindrical rubber samples allow the material constants of the Mooney-Rivlin model to be determined, which was utilised for further work. One of the features specific for a Neidhart spring is its preload. This is the effect of initial deformation of rubber elements during spring assembly. Preload depends mainly on the geometry of rubber parts and the type of material used for their manufacture. The result of the conducted experiments and numerical simulations was the development of a functional relation which, for a given diameter and length of rubber cylinder, allows its elastic force reaction in the assembled spring to be estimated. The presented methodology is universal, because it can also be applied for cylindrical elements made of a different rubber type than that specified in this paper.

REFERENCES

1. **Arruda E. M., Boyce M. C.** (2000), Constitutive models of rubber elasticity: a review, *Rubber Chemistry and Technology*, 73(3), 504-523.

2. **Banić M. S., et al**. (2012), Prediction of heat generation in rubber or rubber-metal springs, *Thermal Science*, 16, Suppl. 2, 527-539.

3. **Baranowski P., Bogusz P., Gotowicki P., Małachowski J.** (2012), Assessment of mechanical properties of off-road vehicle tire: coupons testing and FE model development, *Acta Mechnica et Automatica*, 6(2), 17-22.

4. **Bower A. F.** (2010), *Applied mechanics of solids*, CRC Press, Boca Raton.

5. **Chokanandsombat Y., Sirisinha C.** (2013), MgO and ZnO as reinforcing fillers in cured polychloroprene rubber, *Journal of Applied Polymer Science*, 128(4), 2533-2540.

6. **Gent A. N., Suh J. B., Kelly S. G.** (2007), Mechanics of rubber shear springs, *International Journal of Non-Linear Mechanics*, 42(4), 241 – 249.

7. **Hassan M. A., Abouel-Kasem A., Mahmoud A. El-Sharief, Yusof F.** (2012), Evaluation of the material constants of nitrile butadiene rubbers (NBRs) with different carbon black loading (CB): FE-simulation and experimental, *Polymer*, 53(17), 3807-3814.

8. **ISO 7743** (2011), *Rubber, vulcanized or thermoplastic – Determination of compression stress-strain properties*.

9. **Kim B., Lee S. B., Lee J., Cho S., Park H., Yeom S., Park S. H.** (2012), A comparison among Neo-Hookean model, Mooney-Rivlin model and Ogden model for chloroprene rubber, *International Journal of Precision Engineering and Manufacturing*, 13(5), 759-764.

10. **Lee B. S., Rivin E. I.** (1996), Finite element analysis of load-deflection and creep characteristics of compressed rubber components for vibration control devices, *ASME Journal of Mechanical Design*, 118, 328-336.

11. **Lu Y.T., Zhu H. X., Richmond S., Middleton J.** (2010), A visco-hyperelastic model for skeletal muscle tissue under high strain rates, *Journal of Biomechanics*, 43(13), 2629-2632.

12. **Luo R. K., Mortel W. J., Wu X. P.** (2009), Fatigue failure investigation on anti-vibration springs, *Engineering Failure Analysis*, 16(5), 1366-1378.

13. **Mars W. V., Fatemi A.** (2002), A literature survey on fatigue analysis approaches for rubber, *International Journal of Fatigue*, 24(9), 949-961.

14. **Mooney M.** (1940), A theory of large elastic deformation, *Journal of Applied Physics*, 11(9), 582-592.

15. **Neidhart H.** (1951), *Elastic joints*, US patent 2 712 742.

16. **Neidhart R.** (1969), Special spring unit, *Rubbers Handbook*, Morgan-Grampian, London.

17. **Paluch M.** (2006), *Fundamentals of the Theory of Elasticity and Plasticity*, Wydawnictwo Politechniki Krakowskiej, Kraków (in Polish).

18. **Rivin E. I.** (2003), *Passive vibration isolation*, ASME Press, New York.

19. **Rivin E. I., Lee B. S.** (1994), Experimental study of load-deflection and creep characteristics of compressed rubber components for vibration control devices, *ASME Journal of Mechanical Design*, 116, 539-549.

20. **Rivlin R. S.** (1948), Large elastic deformations of isotropic materials. IV. Further developments of the general theory, *Philosophical Transactions of the Royal Society of London. Series A, Mathematical and Physical Sciences*, 241(835), 379-397.

21. **Samaca Martinez J.R., Le Cam J.-B., Balandraud X., Toussaint E., Caillard J.** (2013), Filler effects on the thermomechanical response of stretched rubbers, *Polymer Testing*, 32(5), 835-841.

22. **Wodziński P.** (2003), Application of elastic rubber suspensions in vibrating screens and feeders (in Polish), *Inżynieria Mineralna*, 3, 109-114.

23. http://www.rosta.ch

Daniel Pieniak, Agata Walczak, Agata M. Niewczas
Comparative Study of Wear Resistance of the Composite with Microhybrid Structure and Nanocomposite

DOI 10.1515/ama-2016-0048

COMPARATIVE STUDY OF WEAR RESISTANCE
OF THE COMPOSITE WITH MICROHYBRID STRUCTURE AND NANOCOMPOSITE

Daniel PIENIAK*, Agata WALCZAK*, Agata M. NIEWCZAS**

*Department of Applied Mechanics, Main School of Fire Services, 52/54 J. Słowackiego St., 01-629 Warszawa, Poland
**Department of Conservative Dentistry with Endodontics, Medical University of Lublin, 7 Karmelicka St., 20-081 Lublin, Poland

dpieniak@sgsp.edu.pl, awalczak@sgsp.edu.pl, agata.niewczas@umlub.pl

Abstract: The aim of the study was to compare microhardness and wear resistance of ceramic-polymer composites with micro and nano-hybrid structure. For the studies commercial composites were used, containing filler particles of the same type but different sizes, nano-sized (Filtek Ultimate) and micro-sized (Filtek Z250) composites. Tribological testing was conducted using ball-on-disc micro-tribometer. Vickers testing method was applied for microhardness studies with the use of Futertech FM 700 device. It has been demonstrated that the wear of Filtek Ultimate is almost twice lower in comparison to wear of Filtek Z250 composite. It has been concluded that the use of filler nanoparticles significantly increased wear resistance of the material. Additionally, lack of correlation between material microhardness and wear resistance has been demonstrated.

Key words: Wear Resistance, Dental Composites, Microhardness

1. INTRODUCTION

In conservative dentistry ceramic-polymer composites are most commonly used. It applies not only to the front teeth, but also to the side teeth – molars and premolars. The ceramic-polymer composites have suitable physical – mechanical properties to oral cavity conditions (Canche-Escamilla et al., 2014). They maintain aesthetic appearance similar to the appearance of the natural tooth tissues for a long operating time. Due to clinical reasons they should also ensure long life of the fillings.

Dental composites consist of a matrix (organic phase-resin) and filler (inorganic phase). The mechanical and tribological properties of dental composites are determined by many parameters such as: size, shape, content and distribution of filler particles in resin matrix (Wang et al., 2015). Commonly used fillers are silica fillers, glass and quartz. However, constantly new materials are being developed, which among other things would increase abrasive wear resistance of the fillings (Hambire and Tripathi, 2013). Size of the particles of inorganic phase in the modern dental composites is above 0.04 μm for microfillers and above 0.005 μm for nanofillers (Schmalz, 2009). The fillers are applied in a form of agglomerates (clusters) or dispersed form. It is believed that the use of filler particles in nano-sized enhance physical and mechanical properties of ceramic-polymer composites (Wang et al., 2015). The quantity of filler in the matrix depends on the type of the composite. Hybrid composites have the highest ratio of inorganic to organic phase, for which the content of the filler ranges from 60 up to 70 percent of the composite volume (% volume) or from 70 up to 85 percent of the composite mass (% weight).

An initial stage of classification studies in case of development of the new dental composites are in vitro studies, conducted in the laboratory conditions using material specimens. In vitro studies

are carried out as preliminary studies. It decreases the time of in vivo studies and reduces the number of clinical trials (Ramalho and Antunes, 2005). One of the most important preclinical studies are studies of the mechanical properties of the surface, including hardness and abrasive wear resistance. It refers particularly to increase of wear resistance of the fillings, with reduction of the wear of opposing teeth (contact teeth). Surface damages may act as traps for particles during chewing process. They accumulate food waste and dental plaque. As a result of the described phenomena, stains may appear on the filling surface, deteriorating aesthetic appearance. Additionally, a biocompatibility of the fillings decreases (Palaniappan et al., 2013).

Wear of the composite filling in the clinical conditions is a result of the opposing teeth contact, food consumption, teeth brushing and illnesses e.g. bruxism. The wear is a sum of phenomenon occurring in the operating conditions, thus abrasive wear and adhesive effect between two mating surfaces, as well as fatigue of the surface layer of the material and corrosive effects (Mair et al., 1996). Especially important types of teeth wear are abrasion and attrition (Palaniappan et al., 2013). The abrasive wear occurs by means of the following three bodies, wearing friction surfaces of opposing teeth and foreign particles between them. In case of composite fillings the abrasive wear appears as abrasion of the soft polymer matrix exposing filler particles (Lambrecht et al., 2006). The attrition is the effect of wear caused by the direct contact of the opposing teeth surfaces, thus the result of interaction of two bodies. During mating of two rough surfaces the microroughness contact occurs. If both body surfaces are hard and brittle at the same time, thus as a result of microroughness contact they deform and fracture after exceeding a critical stress value. In case when the surface of one body has a higher hardness than the opposing surface, it can cause a fast wear by microcutting (Mair, 2000).

Improvement of resistance to wear must be associated with relevant parameters of resistance to movement (friction coefficient). As stated in the publication (Kleczkowska and Bieliński, 2007) too large values of frictions coefficient may lead to premature wear of filling, while too small – to less efficient in crushing food. From authors observation results that the value of composites frictions coefficient in a liquid or suspension environment is within a scope from 0.2 up to 0.45.

It is believed that the level of composite wear depends on the size and content of the filler particles in the structure of the composite and the filler adhesion to the resin matrix (Turssi et al., 2007). If the sizes of filler particles and space between them are smaller than distortions and deformations caused by the contact of two bodies, material behaves almost as a homogeneous one, and its wear is similar to resinous matrix wear. In case when filler particles and size of deformation are similar or filler particles are larger, the material behaves as a heterogeneous one, and the wear is lower than resinous base wear (Kleczkowska and Bieliński, 2007). The wear resistance of ceramic-polymer composites can be also explained through 'protection hypothesis'. The polymer is less wear resistance than filler particles so wear of composites depends from the resin spacing between the particles (Ferracane and Palin, 2013). High quantities of filler in the matrix and small size of particles have an impact on the improvement of tribological properties of composites surface under condition of good dispersion in the material.

2. MATERIAL AND STUDY METHOD

Two commercial ceramic-polymer composites based on methacrylate compounds Filtek Z250 and Filtek Ultimate were studied. Studied composites contain filler particles of the same type but different sizes (Fig. 1, Fig. 2). Detailed data concerning materials are presented in Tab. 1.
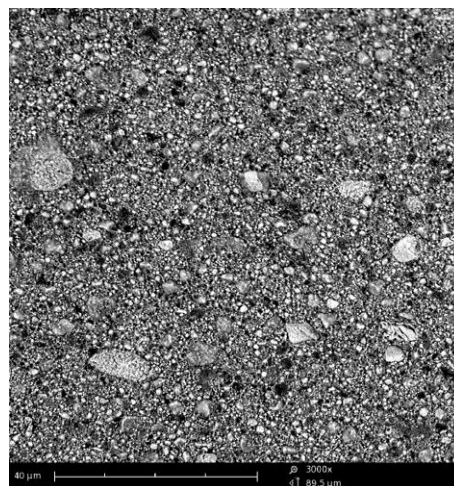
Tab. 1. List of the studied materials (Thomaidis et al., 2013)

Material	Manufacture	Type	Type and size of filler particles	Filler particles content (vol.%)
Filtek Z250	3M ESPE	Micro-hybrid	SiO2/ZrO2 0.01-3.5 μm	60
Filtek Ultimate	3M ESPE	Nanocomposite	SiO2 20 nm, ZrO2 4-11 nm, 0.6-20 μm clusters	63.3

Specimens for microhardness studies were made in a disc shape according to ISO 4049 standard. Samples were cured with light emitting diode (LED) curing light for 40 seconds.

The microhardness study was conducted by Vickers method using Futertech FM 700 device with the load of 50 g, while indenter's penetration time was set to 20 seconds. Measuring coordinates were set in order to possibly include the whole specimen surface, they were identical for all specimens. The study was carried out on 20 samples on the light exposed (LC) and non-exposed surface (NLC).
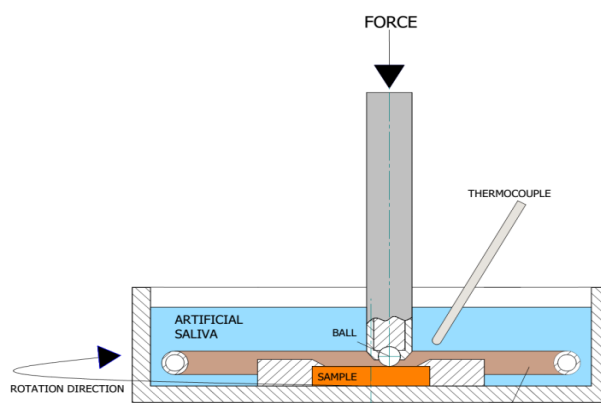

Fig. 1. SEM microstructure of Filtek Z250 composite; zoom 3000x
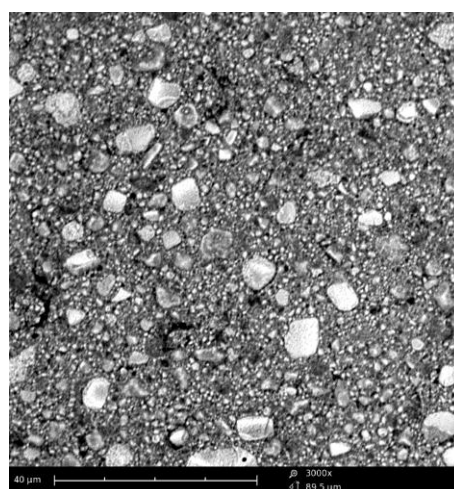
Fig. 2. SEM microstructure of Filtek Ultimate composite; zoom 3000x

Fig. 3. Schematic diagram of wear test apparatus

Wear resistance study was conducted by means of microtribometer (CSM Instruments SA Switzerland) with the ball-on-disc method. Spherical counter specimens were applied with a diameter of 6 mm, made of trioxide aluminum (Al2O3). During the whole period of examination the specimens were immersed in artificial saliva in order to simulate conditions in the oral cavity. A load during the testing was fixed to 5 N. Testing speed was 60 rpm and a sliding distance was 100 m. The studies of wear geometry were performed by means of surface profiler - Veeco Dektak 150. Wear resistance study was conducted on 8 samples on the light ex-

DE GRUYTER OPEN

Daniel Pieniak, Agata Walczak, Agata M. Niewczas
Comparative Study of Wear Resistance of the Composite with Microhybrid Structure and Nanocomposite

DOI 10.1515/ama-2016-0048

posed surface (LC). Fig. 3 shows a schematic configuration of the test machine.

3. STUDY RESULTS AND DISCUSSIONS

Results of microhardness studies of composites are presented in Tab. 2. Both exposed (LC) and non-exposed (NLC) surfaces were taken into consideration. Descriptive statistics of the study results include the following: average value, minimum and maximum value, results dispersion and standard deviation.

Tab. 2. Microhardness measurement results

Material	Surface	Average	Min	Max	Dispersion	St. Dev.
		[HV]				
Filtek Z250	LC	72.78	59.53	83.05	23.52	3.790
Filtek Ultimate	LC	72.99	63.98	80.19	16.21	3.927
Filtek Z250	NLC	75.24	65.66	82.37	16.71	3.490
Filtek Ultimate	NLC	71.56	64.89	78.10	13.21	2.743

LC – exposed side
NLC – non-exposed side

It has been observed that microhardness of Z250 composite and Ultimate composite was similar. No significant differences in average values between LC and NLC have been demonstrated. It may be explained by the same composites manufacturer.

The graphical interpretation of friction coefficient vs. distance has been illustrated in Fig. 4. The curves of friction coefficient vs. distance of studied materials were similar.
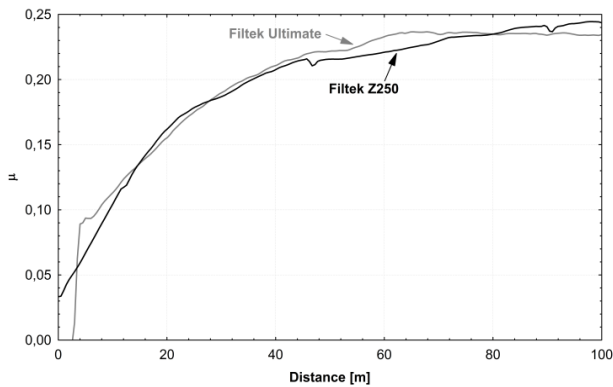

Fig. 4. The curve illustrating changes of friction coefficient vs. distance at the load of 5N

Wear study results are presented in Tab. 3. Descriptive statistics as in case of microhardness have been marked out, and average wear coefficient K. Additionally, the typical wear profiles of composites Filtek Z250 and Filtek Ultimate are shown in Fig. 5.

The wear resistance of Filtek Ultimate composite proved to be significantly higher than the wear resistance of Filtek Z250 composite. The maximum wear value of Filtek Ultimate was 363×10^5 μm^3 and it was lower than the average wear value of Z250 composite. The wear results can be explained by the size of filler particles. Some authors claim that composites containing smaller filler particles showed greater wear resistance compared with composites with larger filler particles (Souza et al., 2016). Other provides studies indicated that filler content influences wear resistance (Wang et al., 2003). Although the similar wear mechanisms, it is difficult to compare results obtained with various methods (Heintze at el., 2005).

Tab. 3. Results of dental composites wear

Material	Average	Min	Max	Dispersion	St. Dev.	Average wear coeff. K
	$10^5 \mu m^3$					$[m^3 F^{-1} m^{-1}]$
Filtek Z250	412	245	596	351	90	8.23×10^{-14}
Filtek Ultimate	227	124	363	239	76	4.54×10^{-14}

Based on the wear studies, the wear coefficient K, including loading and sliding distance was determined. The coefficient for Filtek Z250 was 8.23×10^{-14} $[m^3 F^{-1} m^{-1}]$ and for Ultimate it was 4.54×10^{-14} $[m^3 F^{-1} m^{-1}]$.
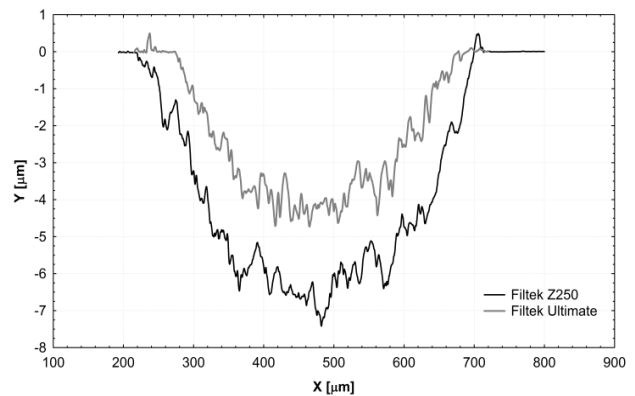

Fig. 5. Typical wear profiles

Figs. 6 and 7 show microscopic images of the wear track of composites Z250 and Ultimate. In figure 6 parallel furrows can be seen. In Fig. 7 visible microcracks propagation directions at the edges of furrows can be noticed. Branching of these microcracks and their re-connection results in separation of individual material particles in the form of scale. This way separated particle is detached from the composite surface.
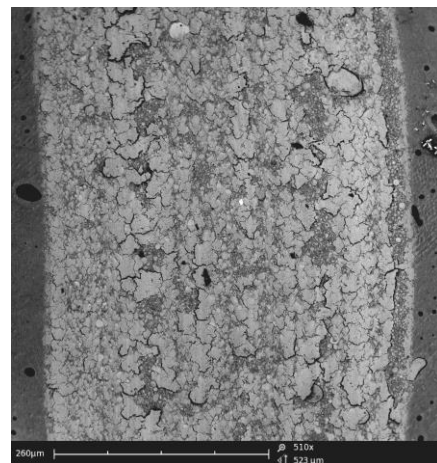

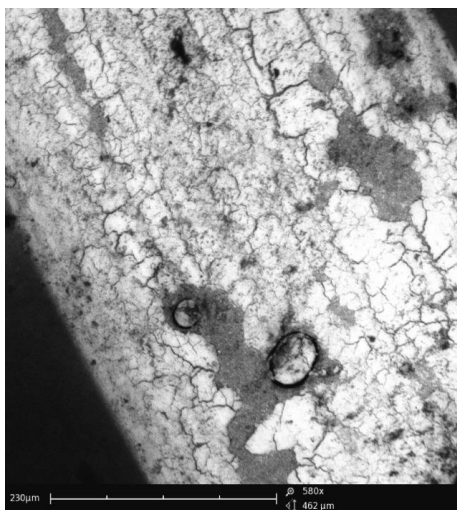**Fig. 6.** Wear track of Filtek Z250 composite; zoom 510x

Fig. 7. Wear track of Filtek Ultimate composite; zoom 580x

4. CONCLUSION

In the presented studies similar values of microhardness for both composites have been obtained. It is known from the literature that there is a correlation between composite microhardness and polymerization shrinkage value. Microhardness study can be also used for the assessment of the local photopolymerization gradient, inhomogeneity of composite properties in the area of polymerization lamp light impact.

In the conducted studies a significantly higher adhesive wear of Filtek Z250 composite comparing to Filtek Ultimate has been demonstrated. The difference in wear could be a result of different composite structure. Nanoparticles content in the structure of the surface layer of Ultimate composite strengthens and unifies its structure. SEM images showed only insignificant local material gaps, while in case of Filtek Z250 material wear traces had linear shape.

It can be concluded from the literature, that the wear of composites depends mainly on the content of the filler in the matrix and size of the filler particles (Finaly et al., 2013; Turssi et al., 2007; Wang et al., 2013). In the conducted studies despite of similar filler content in Z250 and Ultimate composites, the latter one was characterized by higher wear resistance due to smaller size of filler particles (Tab. 1). The dispersion of filler in Ultimate composite was better; material was more homogeneous, with smaller space between the particles, which resulted in lower wear, most probably due to better load transfer between matrix and the filler.

REFERENCES

1. **Canche-Escamilla G., Duarte-Aranda S., Toledano M.** (2014), Synthesis and characterization of hybrid silica/PMMA nanoparticles and their use as filler in dental composites, *Materials Science and Engineering C: Materials for Biological Applications*, 42, 161-167.
2. **Ferracane J.L., Palin W.M.** (2013), Effects of particulate filler systems on the properties and performance of dental polymer composites, in Vallittu P. editor, *Non-Metallic Biomaterials for Tooth Repair and Replacement*, Woodhead Publishing, Cambridge.
3. **Finlay N., Hahnel S., Dowling A.H., Fleming G.J.P.** (2013), The in vitro wear behavior of experimental resin-based composites derived from a commercial formulation, *Dental Matererials*, 29, 365–374.
4. **Hambire U.V., Tripathi V.K.** (2013), Optimization of compressive strength in Zirconia nanoclusters of the Bis-GMA and TEGDMA based dental composites, *Procedia Engineering*, 51, 494–500.
5. **Heintze S.D., Zappini G., Rousson V.** (2005), Wear of ten dental restorative materials in five wear simulators—Results of a round robin test, *Dental Materials*, 21, 304-317.
6. **Kleczewska J., Bieliński D.M**. (2007), Friction and wear of resin-based dental materials, *Archives of Civil and Mechanical Engineering*, 4, 87-96.
7. **Lambrecht P., Debels E., Van Landuyt K., Peumans M., Van Meerbeek B.** (2006), How to simulate wear? Overview of existing methods, *Dental Materials*, 22, 693–701.
8. **Mair L.H.** (2000), Wear in the mouth: the tribological dimension, in Addy M., et al., editors, *Tooth wear and sensitivity. Clinical advances in restorative dentistry*, Martin Dunitz Ltd., London.
9. **Mair L.H., Stolarski T.A., Vowles R.W. Lloyd C.H.** (1996), Wear: mechanisms, manifestations and measurement. Report of a workshop, *Journal of Dentistry*, 24, 141-148.
10. **Palaniappan S., Celis J.P., Meerbeek B., Peumans M., Lambrechts P.** (2013), Correlating in vitro scratch test with in vivo contact free occlusal area wear of contemporary dental composites, *Dental Materials*, 29, 259–268.
11. **Palaniappan S., Peumans M., van Meerbeek B., Lambrechts P.** (2013), Wear prediction in dental composites *in Yan Y. editor, Bio-Tribocorrosion in Biomaterials and Medical Implants*, Woodhead Publishing, Cambridge.
12. **Ramalho A., Antunes P.V.** (2005), Reciprocating wear test of dental composites: effect on the antagonist. *Wear*, 259, 1005–1011.
13. **Schmalz G.** (2009), Resin-Based Composites in Schmalz G. and Arenholt-Bindslev D. editors, Biocompatibility of Dental Materials, Springer, Berlin Heidelberg.
14. **Souza J.C.M., Bentes A.C., Reis K., Gavinha S., Buciumeanu M., Henriques B., Silva F., Gomes J.R.** (2016), Abrasive and sliding wear of resin composites for dental restorations*, Tribology International* 102, 154-160.
15. **Thomaidis S., Kakaboura A., Mueller W.D., Zinelis S.** (2013), Mechanical properties of contemporary composite resins and their interrelations, *Dental Materials*, 29, 132-141.
16. **Turssi C.P. Ferracane J.L., Vogel K.** (2005), Filler features and their effects on wear and degree of conversion of particulate dental resin composites, *Biomaterials*, 26, 4932-4937.
17. **Turssi C.P., Faraoni-Romano J.J., Menezes M., Serra M.C.** (2007), Comparative study of the wear behavior of composites for posterior restorations, *Journal of Materials Science: Materials in Medicine*, 18, 143-147.
18. **Wang L., D'Alpino P.H., Lopes L., Pereira J.** (2003), Mechanical properties of dental restorative materials: relative contribution of laboratory tests, *Journal of Applied Oral Science*, 11, 162–7.
19. **Wang R., Bao S., Liu F., Jiang X., Zhang Q., Sun B., Zhu M.** (2013), Wear behavior of light-cured resin composites with bimodal silica nanostructures as fillers, *Materials Science and Engineering C: Materials for Biological Applications*, 33, 4759–4766.
20. **Wang R., Zhang M., Liu F., Bao S., Wu T., Jiang X., Zhang Q., Zhu M.** (2015), Investigation on the physical-mechanical properties of dental resin composites reinforced with novel bimodal silica nanostructures, *Materials Science and Engineering C: Materials for Biological Applications*, 50, 266-273.

MECHATRONIC DEVICE FOR LOCOMOTOR TRAINING

Sławomir DUDA[*], Damian GĄSIOREK[*], Grzegorz GEMBALCZYK[*], Sławomir KCIUK[*], Arkadiusz MĘŻYK[*]

*Faculty of Mechanical Engineering, Department of Theoretical and Applied Mechanics, Silesian University of Technology,
ul. Akademicka 2A, 44-100 Gliwice, Poland

Slawomir.Duda@polsl.pl, 522400@gmail.com, Grzegorz.Gembalczyk@polsl.pl, Slawomir.Kciuk@polsl.pl, Arkadiusz.Mezyk@polsl.pl

Abstract: This paper presents a novel mechatronic device to support a gait reeducation process. The conceptual works were done by the interdisciplinary design team. This collaboration allowed to perform a device that would connect the current findings in the fields of biomechanics and mechatronics. In the first part of the article shown a construction of the device which is based on the structure of an overhead travelling crane. The rest of the article contains the issues related to machine control system. In the prototype, the control of drive system is conducted by means of two RT-DAC4/PCI real time cards connected with a signal conditioning interface. Authors present the developed control algorithms and optimization process of the controller settings values. The summary contains a comparison of some numerical simulation results and experimental data from the sensors mounted on the device. The measurement data were obtained during the gait of a healthy person.

Key words: Mechatronic Device, Gait Reeducation, Rehabilitation, Real-Time Systems, Control Systems

1. INTRODUCTION

In the contemporary world, the number of traffic accidents and civilization-related diseases leading to the loss of motor abilities is constantly growing (Botticello et al., 2014). Numerous diseases and injuries may permanently affect this ability while hindering ordinary functioning of a person and often preventing one from performing daily activities that seem trivial to those in possession of full motor skills. Such a situation makes the patient dependent on the support of other persons and hinders autonomous performance of physiological activities or social functions. In case of occurrence of walking disorders, rehabilitation of the patient becomes a necessity. It is aimed at the recovery – as far as possible – of the lost motor abilities. This is related to retraining the patient's ability to walk in new circumstances (Bae and Tomizuka, 2012; Behrman and Harkema, 2000; Boyd and Little, 2005; Hesse and Werner, 2009; Mailah et al., 2009).

To meet the need to ensure fast and reliable rehabilitation leading to full recovery of abilities in patients with a walking dysfunction, various classes of instruments and devices are designed and manufactured. These include both the simplest ones and ones that are highly intricate and utilize state-of-the-art advancements. Currently, among all devices of this type, stabilometric and balance platforms equipped with handrails or a patient suspension system protecting the patient against fall are most commonly used in rehabilitation centres. Examples of such platforms are the Biodex and Tecno Body stabilometric and balance platforms (Sawers and Ting, 2014; Cao et al., 2014; Hussain et al., 2013; Sherafat et al., 2013).

The platform itself, however, does not make learning to walk possible. For that purpose, treadmills may be used, on which the patient – protected with a special harness system similar to the one employed in the platforms – may learn to move. The Gait Trainer by the Biodex company with an UWS OFFSET unloading system may serve as an example of such devices. Using this system, the patient supports himself using handrails or is suspended in a harness, while simultaneously moving on the treadmill (Mulroy et al., 2010; Walker, et al., 2010). In the recent years, devices additionally forcing the movement of lower limbs came into use as well. Examples of such devices are the Lokomat by Hocoma or AutoAmbulator by the HealthSouth company (Lunenburger et al., 2004). Such devices are also often used in rehabilitation and waking of persons in coma. The immobilization of pelvis, however, is an obstacle for conscious patients learning to walk. Studies have proved that the immobilisation of the pelvis while walking significantly changes its pattern (Akdogan and Adli, 2011; Hidler and Wall, 2005).

Additionally, the movement of the lower limb in these devices is limited only to the sagittal plane, without ensuring proper movements in the frontal or transverse planes. It is also not without significance that the movement on the treadmill is not the same as moving in space. Treadmill training introduces habits different from those assumed to be correct in walking. All this may lead to the strengthening of improper movements, which may cause arthritis or lead to future traumatic injuries. Devices such as the Gait Trainer by Rifton or Kaye Products constitute an attempt to depart from methods based on movement on a treadmill. The above are walking frames with wheels and a harness system for the patient. The possibility of the patient's movement in horizontal paths is a great advantage of this type of devices. As far as rehabilitation is concerned, however, there are some disadvantages: the immobilization of the pelvis, the use of seats for unloading and the impossibility to conduct such exercises as climbing the stairs (Marchal-Crespo and Reinkensmeyer, 2009).

Without a doubt, the most technologically advanced device

that was recently introduced to the market is the ZeroG device patented in the United States (patent No. US 7,883,450 B2). ZeroG is a mechatronic system for the assistance of human movement with unloading, which allows for the movement of the subject along a given path. Depending on the current position of a human, resulting from the phase of walk, the system's drives provide a reaction, thus ensuring the necessary unloading value (Hidler et al., 2011).

Striving to meet the need for a modern, domestic rehabilitation device for persons with a walking impairment, the employees of the Department of Theoretical and Applied Mechanics of the Silesian University of Technology have undertaken to build a demonstrative device for the re-education of walk which allows for autonomous movement of the patient in unloading conditions within the framework of the NR03-0040-10 research and development programme. The completed project is innovative, as the conducted domestic and worldwide market analysis has demonstrated that no such device has been used in the rehabilitation of persons having problems with locomotion (Duda et al., 2011). A device that would connect the current findings in the fields of biomechanics and mechatronics. The application of the device in rehabilitation of persons with locomotion disorders, with underlying conditions of both traumatic and neurological nature, provides an improvement of the working conditions of the staff conducting the rehabilitation. Also the patient's safety is improved, as they will be able to perform walking-related exercises while being protected against fall and to perform the exercises in pre-set unloading conditions. An additional advantage over similar devices available in the market is the possibility to learn to climb the stairs and to cross obstacles that may be encountered in everyday life.

2. CHARACTERISTICS OF THE DEVICE

The following basic systems may be distinguished in the developed device (Duda et al., 2011):
— support frame made of aluminium profiles;
— mechanical elements of the drive systems;
— motors with controllers and a control cabinet;
— computer with real-time boards installed;
— sensors measuring the dynamic states of the device with power feed.

The structure of the device is based on the structure of an overhead travelling crane. As a result of installing three drives, the movement of the sling of the person in rehabilitation is possible in all axes of the Cartesian coordinate system. Fig. 1 presents the arrangement of the individual axes.
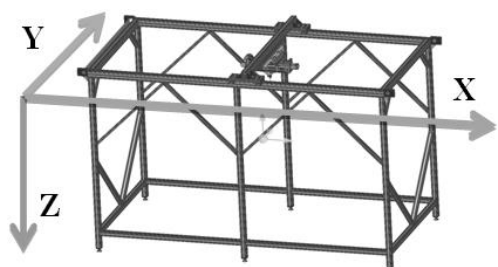

Fig. 1. Directions and senses of the axes of the global coordinate system corresponding to the movements of individual drives

The basic mechanical part of the device is constituted by drive systems responsible for the transfer of the movement from the motor to the working units. The proposed drive system has been presented in a structural form (Fig. 2).

The performance of all assumed objectives requires the control system to operate with different parameters, depending on the mode of operation. This is why it was decided to divide the tasks and performance of various operation modes into separate tasks. By means of special expansion boards, the Matlab/Simulink suite allows for real-time control and measurement data acquisition using real-time simulation methods. Real time operation is characterized by the maintenance of certain time regimes, due to which the solver's step of integration is kept with the real time (Campa et al., 2004; Faust et al., 2015).
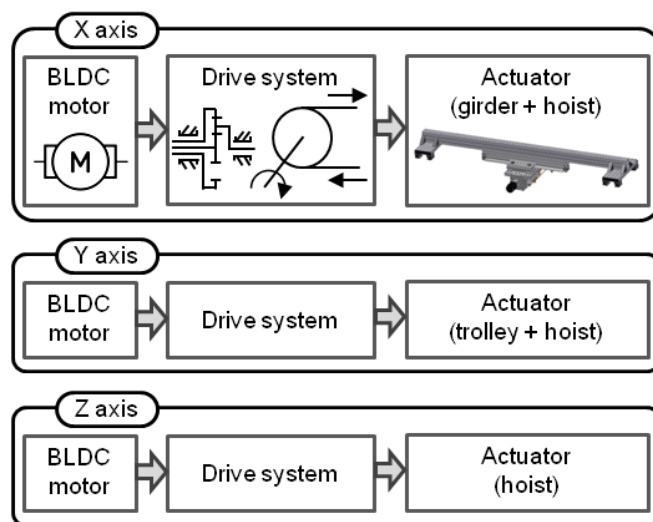

Fig. 2. Structural scheme of the drive system in mechatronic device for locomotor training
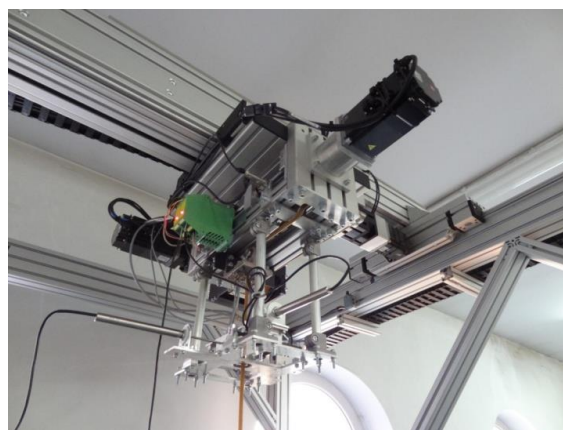

Fig. 3. The mechanism of dynamic unloading of patient with a rope displacement angle and force measurement system

The real-time systems connected to external devices are characterized by the fact that the calculations necessary for the supervision and control of the operations conducted by the controlled device are in parallel to the operation of the device. Moreover, the calculations give consideration to the current state of the device (Kaliński and Buchholz, 2015).

The transmission of control and measurement signals between the walking re-education device and the computer with the control system is conducted by means of two RT-DAC4/PCI real

time boards connected with a signal conditioning interface. A control unit equipped with servo inverters of each of the motors is an additional element necessary for the correct operation of the device. As in each of the drives speed control is used, the servo inverter works as a regulator controlling the torque of the motor so as to ensure the required rotational speed (defined by the control signal). Each of the control signals is sent from real time boards to

the control unit which works out the settings for the drive motors.

Analogue signals from the remaining sensors installed in the device are sent directly to the board conditioning the analogue signals. These sensors include the constructed devices for rope force measurement and the measurement of the sling rope deflection angle (Fig. 3) (Gembalczyk and Duda, 2012). The data transmission diagram has been presented in Figs. 4 and 5.
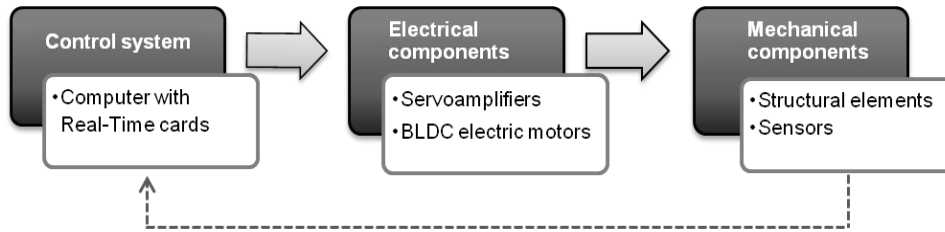
Fig. 4. Diagram of subassembly connections of the mechatronic device used in the process of walking reeducation
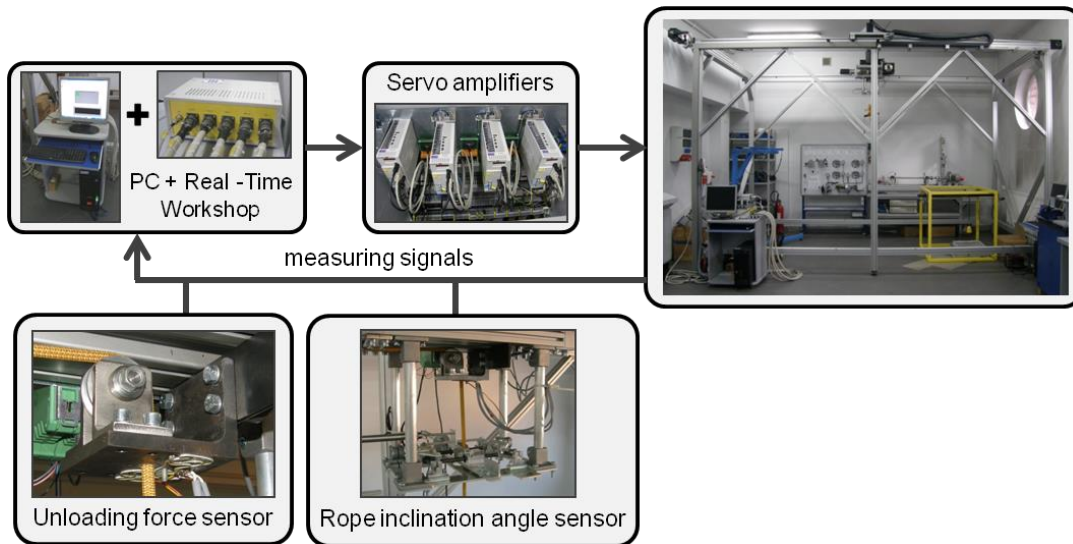

Fig. 5. Diagram of the control and measurement signal transmission

The control of the device is conducted by means of the MATLAB/Simulink suite. Two tabs are visualized in the main window of the application. Each of the tabs is responsible for the processing of different measurement, control and servomotor control signals. Due to the real-time library included in the MATLAB/Simulink software suite, the user of the programme may freely operate these signals (Duda et al., 2014).

3. DRIVE CONTROL ALGORITHM

The algorithm controlling the device's drives, encompassing the X, Y and Z axes, has been divided into three independent systems due to the expected performance method and the requirements of movement of the subassemblies. The control is performed in a closed control system using PD regulators by generating proper voltages which are supplied to BLDC motors.

A follow-up control system has been implemented for the X and Y axes. In this case, the algorithm of operation performs a certain wave of the controlled value, while the wave is not known. The purpose of this system is to control the object in such a way so as the changes of the regulated value would directly

follow the changes of the pre-set value. In this case, the system aims at the minimization of the rope deflection angle. It is also possible to set a trajectory for the movement of the rope suspension point in the XY axis of the device (Duda et al., 2015).

For the Z axis – the dynamic compensator of rope length, an algorithm aimed at keeping a constant force value in the rope has been implemented. This is necessary to achieve a constant unloading value required in some of the rehabilitation and walking re-education processes.

The correctness of the device operation, which is strictly related to the values of the regulators' settings, has been considered in the view of:
— ensuring the possibility of free movement – device directly following the patient,
— the possibility to set and maintain an assumed unloading level,
— ensuring the safety of the rehabilitated person – ensuring balance and preventing any possible falls.

In the proposed follow-up movement control system in the X and Y axes, the proper value of the rotational speed control signal of the drive motor is selected based on the misalignment signal. The misalignment signal equals the value of the crane rope de-

flection from the perpendicular (the pre-set rope deflection angle value equals zero). This angle is dependent on the coordinates of the crane trolley and the location of the patient. The value of rope inclination angle is measured by a dedicated sensor that was designed and made by the authors of the article. The idea behind the algorithm controlling the follow-up movement of the crane has been presented in Fig. 6.
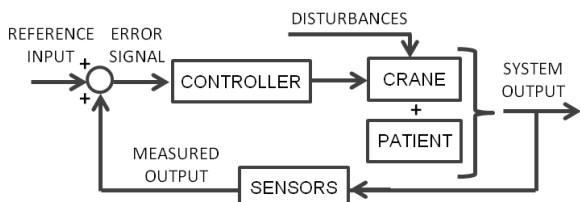

Fig. 6. Block diagram of the regulation system

To determine the values of the PD regulator settings, a numerical model of the tested device as a mechatronic system has been developed in the MATLAB/Simulink environment, giving consideration to complex couplings occurring between the individual elements of the system: the control unit – the drive – the human (Fig. 7). The numerical model allows also to calculate the rope deflection angle in XZ and YZ planes (α, β) and the value of unloading force (F_{unl}). The rotational speed control signals (CS_X, CS_Y, CS_Z) of drive systems for each axis of the device are an inputs in the developed numerical model.
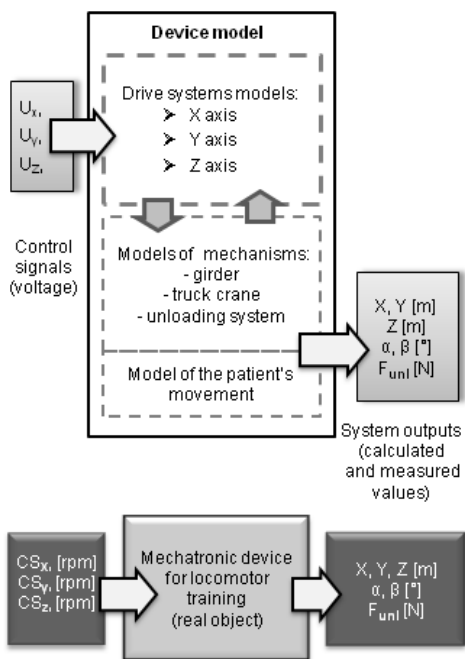

Fig. 7. Directions and senses of the axes of the global coordinate system corresponding to the movements of individual drives

The model of the patient's movement has been obtained from studies conducted with non-affected persons using a photogrammetric method (Cappozzo et al., 2005). In the initial selection of the setting values it has been noted that in case of excessive value of the P proportional element, the trolley of the crane overtakes the moving person. This leads to a situation in which the suspension system starts to perform a reciprocating motion along

the OX axis with increasing speed. This situation is presented in Figs. 8 and 9, exhibiting the movement of the suspension mechanism and the patient and the change in the value of the control signal of the rotational speed of the drive motor.
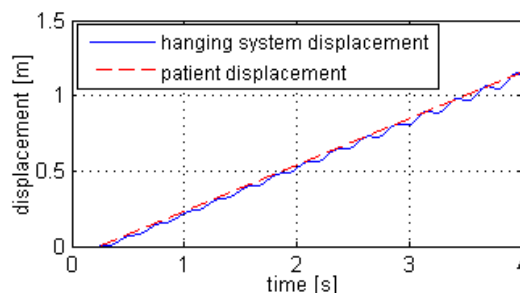

Fig. 8. Movement along x axis of the patient and the crane trolley as a function of time
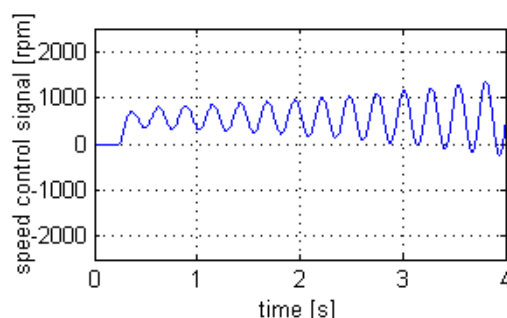

Fig. 9. Graph of the control signal of the rotational speed of the drive motor

The same phenomenon as in numerical simulations has been observed in the real object. An additional factor which affect on increasing such operation of the drive are the disturbances of signals from the measurement of the rope deflection angle, which constitute the feedback signal of the regulation system.

The conducted study has demonstrated that with excessive values of the PD regulator settings, the suspension system does not fluently perform the follow-up movement. Instead, high speed changes, especially notable during slow movement, occur during tracing. In the initial phase of the study, when the person moved with low speed (it is a follow-up movement, so the speed of the crane may be assumed to be approximately the patient's speed), the trolley would overtake the person and then conduct a reverse motion.

The presented situation causes both dangerous (potentially leading to a fall) and uncomfortable rehabilitation conditions. In selection of the optimal settings of the PD regulator, both the rope deflection angle and the changes of speed of the trolley of the suspension system during the movement of the patient were minimized (1) to ensure fluent operation at perpendicular orientation of the rope (in such position, the suspension system has the lowest impact on the natural movement of a person).

$$F(\varphi) \cdot a + F(\ddot{\varphi}) \cdot b \rightarrow min \qquad (1)$$

$$F(\ddot{\varphi}) = \int_{t=0}^{T} \left| \frac{d^2\varphi}{dt^2} \right| dt \qquad (2)$$

where: T – final time of simulation; $F(\varphi)$ – function of the rope deflection in gait plane as a function of time; $F(\ddot{\varphi})$ – function describing the angular speed changes of the crane's rope in the

DE GRUYTER
OPEN

Slawomir Duda, Damian Gasiorek, Grzegorz Gembalczyk, Slawomir Kciuk, Arkadiusz Mezyk   DOI 10.1515/ama-2016-0049
Mechatronic Device for Locomotor Training

direction of the patient's movement; a, b – parameters specifying the impact of the deflection angle function and the linear speed change function on the minimized objective function.– description. The a and b parameters have been selected so that both functions (rope deflection angle and winch speed changes) would have a comparable impact on the objective function. With a problem formulated this way and assuming the patient's movement with a constant speed, the process of optimization of the regulator's parameters was conducted using a gradient method.

The resulting values (P=300, D=10) have been implemented in the control system of the actual object. After the patient's movement registered in the tests was considered in the numerical model, the results of the simulation and experiment exhibited similar values. The functions presented in Figs. 10 constitute a comparison of the rope deflection angle in XZ plane during the simulation and in the experiment. Figure 11 present the x-axis movement of the patient and the trolley registered during the tests of the actual object.
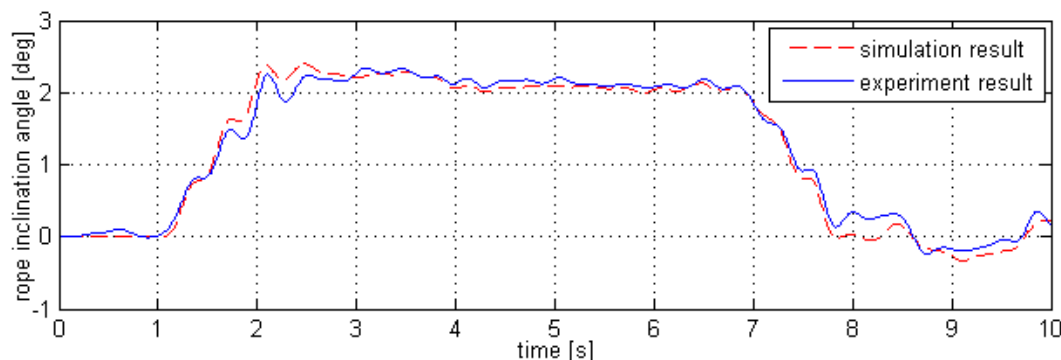

Fig. 10. Changes of the deflection angle of the rope of the crane sling in XZ plane as a function of time
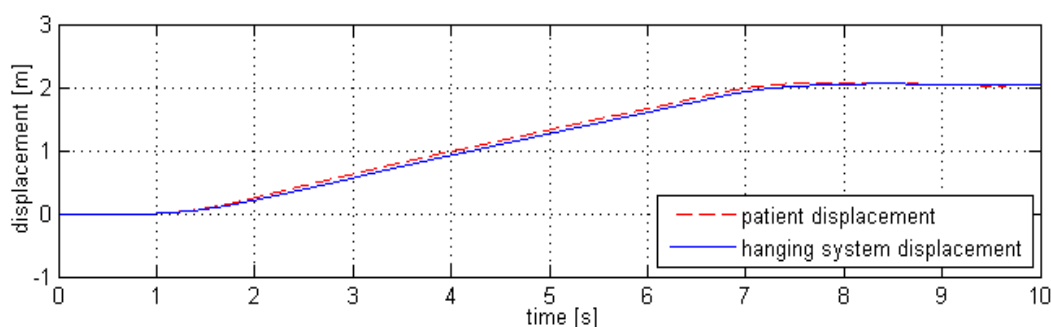

Fig. 11. Movement of the patient and the suspension system of the crane as a function of time
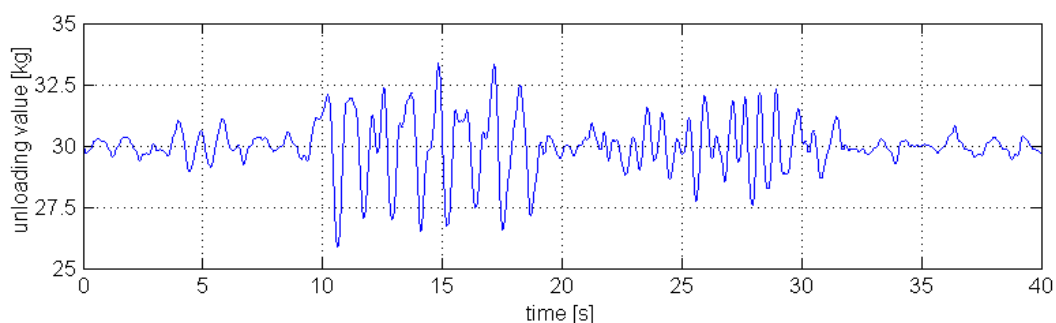

Fig. 12. Graph of the unloading force as a function of time

The parameters of the regulator responsible for the follow-up movement in the OY axis were selected in a similar manner. The obtained parameter values were after rounding: P = 1100, D = 20, respectively.

Based on the obtained results, it may be concluded that the used control algorithms of each of the axes function properly. It should be noted that in the device the Y axis is a supportive axis, responsible for ensuring that the suspension mechanism follows the lateral movements of the patient. The main direction along which the patient is supposed to move is the direction of the X-

axis.

When walking, the centre of inertia of a human moves along the perpendicular axis (the Z axis of the device), which results in the changes of the force value in the rope on which the patient is suspended. This is why the control of the drive in the Z axis is related to the maintenance of a constant, pre-set value of unloading force acting on the patient during the walk.

The selection of correct settings of the regulator has been conducted experimentally during a physical studies. This method of tuning the controller was caused by disturbances of the signal

from the force measurement sensor. Excessive values of the proportional element in the regulator caused significant changes in the values of the control signal of the motor, which resulted in the instable operation of the motor and uncomfortable conditions of rehabilitation. The optimal value of the P parameter selected in the algorithm amounted to 200. The graph of the unloading value during the test has been presented in Fig. 12.

4. CONCLUSIONS

The work presents the structure and real-time components cooperation in an innovative device used to support the rehabilitation process of persons affected by a walking impairment. The use of a computer as the management unit allows for the modification of algorithms and parameters of the control system, which may be motivated by the occurrence of new factors that were not considered earlier. Moreover, the continuous recording of the registered parameters obtained from the installed sensors was made possible, thus allowing for the assessment of rehabilitation progress.

The algorithms developed for the control of the device allow to conduct rehabilitation in two basic modes – as a protective follow-up system and in unloading conditions. Both modes were analyzed and tested, exhibiting the correctness of the proposed control algorithms.

The work presents a idea of computer tool for the testing of the dynamic behaviour of electric drives operating as a mechatronic device. The methodology of the conducted tests assumed the development of models for the individual systems and their further coupling in a loop to test whether the complete system works properly. The developed methodology allows for creating dynamics models for a wide range of rehabilitation devices which constitute mechatronic systems utilizing real-time control and their use in the design and the optimization of the structures of these devices and the synthesis of algorithms for controlling their movement.

REFERENCES

1. **Akdogan E., Adli M.A.** (2011), The design and control of a therapeutic exercise robot for lower limb rehabilitation: Physiotherabot, *Mechatronics*, 21(3), 509-522.
2. **Bae J., Tomizuka M.** (2012), A gait rehabilitation strategy inspired by an iterative learning algorithm, *Mechatronics*, 22(2), 213-221.
3. **Behrman A.L., Harkema S.J.** (2000), Locomotor training after human spinal cord injury: a series of case studies, *Physical Therapy*, 80(7), 688-700.
4. **Botticello A.L., Rohrbach T., Cobbold N.** (2014), Disability and the built environment: aninvestigation of community and neighborhood land uses and participation for physically impaired adults, *Annals of Epidemiology*, 24(7), 545-550.
5. **Boyd J.E., Little J.J.** (2005), Biometric gait recognition, *Advanced Studies in Biometrics*, Springer, 3161, 19-42.
6. **Campa R., Kelly R., Santibanez V.** (2004), Windows-based real-time control of direct-drive mechanisms: platform description and experiments, *Mechatronics*, 14(9), 1021-1036.
7. **Cao J., Xie S.Q., Das R., Zhu G.L.** (2014), Control strategies for effective robot assisted gait rehabilitation: The state of art and future prospects, *Medical engineering & Physics*, 36(12), 1555-1566.
8. **Cappozzo A., Della Croce U., Leardini A., Chiari L.** (2005), Human movement analysis using stereophotogrammetry Part 1: theoretical background, *Gait & Posture,* 21(2), 186–196.
9. **Duda S., Gembalczyk G., Kciuk S., Gasiorek D.** (2014), Mechatronic device to protect against falls during locomotor rehabilitation, *Proceedings of the 3rd Joint International Conference on Multibody System Dynamics*, Busan, 121-122.
10. **Duda S., Kawlewski K., Gembalczyk G.** (2015), Concept of the System for Control over Keeping up the Movement of a Crane, *Solid State Phenomena*, 220, 339-344.
11. **Duda S., Michnik R., Kciuk S., Jurkojć J., Kawlewski K., Machoczek T.** (2011), The conception of a mechatronic device for locomotor training, *Aktualne Problemy Biomechaniki*, 5, 29-36.
12. **Faust O., Yu W., Acharya U.R.** (2015), The role of real-time in biomedical science: A meta-analysis on computational complexity, delay and speedup, *Computers in Biology and Medicine*, 58, 73-84.
13. **Gembalczyk G., Duda S.** (2012), Design and validation of devices for measuring the force and the angle of inclination rope in crane, *Modelowanie inżynierskie*, 14(45), 32-38. [in Polish]
14. **Hesse S., Werner C.** (2009), Connecting research to the needs of patients and clinicians, *Brain Research Bulletin*, 78, 26-34.
15. **Hidler J., Brennan D., Black I., Nichols D., Brady K. Nef T.** (2011), ZeroG: Overground gait and balance training system, *Journal of Rehabilitation Research & Development*, 48(4), 287-298.
16. **Hidler J.M., Wall A.E.** (2005), Alteration in muscle activation patterns during robotic-assisted walking, *Clinical Biomechanics,* 20, 184-193.
17. **Hussain S., Xie S.Q., Jamwal P.K.** (2013), Control of a robotic orthosis for gait rehabilitation, *Robotics and Autonomous Systems*, 61(9), 911-919.
18. **Kaliński K.J., Buchholz C.** (2015), Mechatronic design of strongly nonlinear systems on a basis of three wheeled mobile platform, *Mechanical Systems and Signal Processing*, 52-53, 700-721.
19. **Lunenburger L., Colombo G., Riener R., Dietz V.** (2004), Biofeedback in gait training with the robotic orthosis Lokomat, *Engineering in Medicine and Biology Society*, 4888-4891.
20. **Mailah M., Jahanabadi H., Zain M.Z.M., Priyandoko G.** (2009), Modelling and control of a human-like arm incorporating muscle models, *Journal of Mechanical Engineering Science*, 223(7), 1569-1577.
21. **Marchal-Crespo L., Reinkensmeyer D.J.** (2009), Review of control strategies for robotic movement training after neurologic injury, *Journal of neuroengineering and rehabilitation*, 6, 20.
22. **Mulroy S.J., Klassen T., Gronley J.K., Eberly V.J., Brown D.A., Sullivan K.J.** (2010), Gait parameters associated with responsiveness to treadmill training with body-weight support after stroke: an exploratory study, *Physical Therapy,* 90(2), 209-223.
23. **Sawers A., Ting L.H.** (2014), Perspectives on human-human sensorimotor interactions for the design of rehabilitation robots, *Journal of neuroengineering and rehabilitation*, 11, 142.
24. **Sherafat S., Salavati M., Takamjani I.E., Akhbari B., Mohammadirad S., Mazaheri m., Negahban H.** (2013), Intrasession and intersession reliability of postural control in participants with and without nonspecific low back pain using the Biodex Balance System, *Journal of manipulative and physiological therapeutics*, 36(2), 111-118.
25. **Walker M.L., Ringleb S.I., Maihafer G.C., Walker R., Crouch J.R., Van Lunen B., Morrison S.** (2010), Virtual reality–enhanced partial body weight–supported treadmill training poststroke: feasibility and effectiveness in 6 subjects. *Archives of physical medicine and rehabilitation*, 91(1), 115-122.

CHARACTERISTICS OF PNEUMATIC TUNERS OF TORSIONAL OSCILLATION AS A RESULT OF PATENT ACTIVITY

Jaroslav HOMIŠIN*

*Faculty of Mechanical Engineering, Department of design, Automotive and Transport Engineering, Technical University of Košice, Letná 9, 040 01 Košice, Slovakia

jaroslav.homisin@tuke.sk

Abstract: Mechanical systems with combustion engines, compressors, pumps and fans, can be characterized as torsional oscillating mechanical systems (TOMS). It is therefore necessary to control their dangerous torsional vibrations. It was confirmed that dangerous torsional vibration can be reduced to acceptable level by an appropriate adjustment, respectively by tuning the TOMS. According to several authors, the most appropriate way of system tuning is application of suitable flexible element, which is flexible shaft coupling. It turned out that one of the types of shaft couplings, which are particularly suited to meeting this objective are pneumatic flexible shaft couplings, to act as so-called pneumatic tuners of torsional oscillations. The issue of research and development of pneumatic tuners of torsional oscillations, among other things is, long-term in the focus of the author. The existence of tuners creates the opportunity to develop new ways of tuning torsional oscillating mechanical systems. The author of the scientific article will focus on the characteristics of developed pneumatic tuners of torsional oscillation in terms of their design, construction, function, significance advantages and conditions imposed on pneumatic tuners based on the results of his patent activity. Simultaneously provides information about the characteristic properties of pneumatic tuners of torsional oscillations in the general design.

Key words: Pneumatic Tuner of Torsional Oscillation, Torsional Oscillating Mechanical System, Characteristics of Pneumatic Tuners

1. INTRODUCTION

In mechanical systems with reciprocating machines as driving or driven devices dangerous torsional vibration occurs. It means that Mechanical systems with combustion engines, compressors, pumps and fans, can be characterized as torsional oscillating mechanical systems (TOMS).

TOMS can be considered, from dynamic point of view, as systems working most frequently in supercritical range with relatively quick transient process by startup and braking. In terms of regulation they can be categorized as a controlled system with incomplete information. Incomplete information is reflected particularly in the area of unexpected (random) of failure effects. The most common effects of random disturbances in TOMS include the effects piston machines themselves. On this basis, it can be stated that especially piston machines introduce into these systems increased torsional vibration causing their excessive dynamic load.

Therefore, it is necessary to control their dangerous torsional vibration. It was confirmed that dangerous torsional vibration can be changed on the acceptable level by an appropriate adjustment, respectively tuning the TOMS. Under tuning the mechanical system should be understood an appropriate adjustments of dynamic properties of some of its members to the dynamics of the system. This means that to achieve the aims to reduce unacceptable torsional vibration, it is necessary that any TOMS has to be previously tuned.

According to several authors, the most preferred method of system tuning is the application of a suitable elastic element, which is considered a flexible shaft coupling (Ankarali et al., 2012; Bolek et al., 1967; Gao et al., 2010; Grega et al., 2015; Homišin, 1996; Homišin, 2008; Yubao, 2013; Lacko, 1971; Poľakov, 1979; Singiresu, 1996; Timošenko, 1960; Wilson, 1968).

With this issue any manufacturer of flexible shaft couplings is seriously concerned. The world's leading manufacturers of flexible couplings are currently trying to solve this problem by using flexible shaft couplings with particularly low torsional rigidity (Bingzhao et al., 2010; Böhmer, 1983; Curà et al., 2013; Gao et al., 2010; Homišin, 1986; Homišin, 2002; Homišin, 2016; James et al., 2014; Lunke et al., 1983; Zoul, 1988; Zoul, 1989).

It was shown that one of the types of shaft couplings, which are particularly suited to achieve this are the pneumatic flexible shaft couplings, which acts as a so-called pneumatic tuners of torsional oscillations.

The issue of research and development of pneumatic flexible shaft couplings is, among other things, long in the focus of the author. In the scientific research field the author focuses on proper design of new types of shaft couplings, and pneumatic flexible shaft couplings (newly developed types of flexible shaft couplings are resulting from the claims of more than seventy granted patents of the author (Homišin, 1986a, 1986b, 1995a, 1995b, 1996b, 1998, 2002a, 2016), investigation of the basic properties of developed pneumatic couplings (the author dealt with the research of pneumatic flexible shaft coupling in scientific papers (Homišin, 1996a; Grega et al., 2015).

Particularly he aims at facilitating the application of the given couplings in various types of torsional oscillating mechanical systems with the objective of optimal tuning, thus optimizing them

in terms of achieving minimum levels of dangerous torsional oscillation, or its removal. The existence of pneumatic couplings, thus pneumatic tuners of torsional oscillations, creates the possibility of implementing new ways of torsional oscillating mechanical systems tuning. The aim of the scientific article is the focus on the characteristics of the pneumatic tuners of torsional oscillation developed by the author in terms of their structure, function, importance and advantages based on his patent activity, as well as presenting their characteristic properties in general terms.

2. BRIEF CHARACTERISTICS FUNCTION AND IMPORTANCE OF FLEXIBLE SHAFT COUPLINGS

Based on the general characteristics of flexible shaft couplings applies that in addition to compensating axial, radial and angular shaft misalignment serve as a very effective means of tuning of any TOMS in terms of torsional vibration size. Appropriate tuning of TOMS is ensured by an appropriate adaptation of the dynamic properties of flexible coupling to the dynamics of mechanical systems, based on a detailed dynamic analysis. It follows that a properly selected flexible shaft coupling is used to limit the formation of resonances in the operating speed range (OSR) and thus to control dangerous torsional vibrations. Usually moves the natural angular frequency of torsional oscillation Ω_O, and thus the critical speed $n_k \to n_k^*$ from individual load torque harmonic components (particularly from the major harmonic component), in the lower rotation frequency area (Fig. 1). As a result, by the rapid start-up, respectively braking no unacceptable torsional vibrations occur and are damped by the coupling.
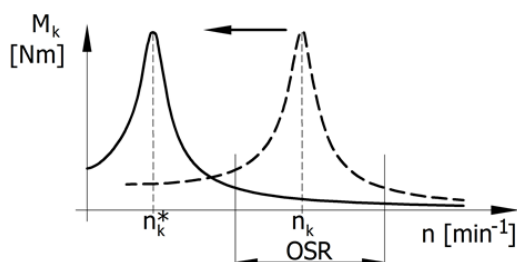

Fig. 1. Demonstration of the effect of flexible couplings on the dynamics of the system

With regard to their basic characteristics, i.e. dynamic torsional stiffness k and the damping coefficient b, it should be noted that they are affected by material (metal, rubber, plastics), shape, number, size and design modifications to their flexible elements. Thus, they depend on various factors, each in its own way influences the characteristics of flexible couplings. Based on their impact the above factors can be divided into two groups – stable and unstable factors. The shape, number, size and various structural modifications of the elastic members can be categorized as stable factors. Material of elastic elements to a group of unstable factors, as they change its original characteristics as a result of fatigue and aging.

The above influences acting on the basic characteristics of shaft couplings show that each flexible coupling member, whether it is metallic or non-metallic, is exposed to fatigue or aging in the case of acting external forces. As a result, there is a change of coupling load characteristics $M_k = f(\varphi)$ (with respect to initial characteristics), and thus to change of its basic characteristic properties. It should also be noted that any currently

used linear or non-linear coupling has only one characteristic. The result of this fact, it is only one course of natural speed frequency in the Campbell diagram. Change of the characteristics of the flexible coupling due to an appropriate adaptation of the dynamic properties to the dynamics of TOMS means using a different elastic element or using another flexible coupling. Taking into account this fact, as well as the instability of dynamic properties of flexible couplings caused by aging and fatigue, the elastic elements cause detuning of a previously tuned TOMS. In this case, the tuning member, i.e. flexible shaft coupling, has no possibility of eliminating or reducing dangerous increasing torsional vibration (Zoul, 1982).

Taking into account the above considerations in order of tuning or continuous tuning (Attention should be paid to the option of tuning torsional oscillating mechanical systems with pneumatic tuners out of service and continuous tuning of the system during operation at steady-state in the following article entitled: "New ways of tuning torsional oscillating mechanical systems".) of TOMS with intention of reducing dangerous torsional oscillations, we proposed to use pneumatic flexible shaft couplings developed by us i.e. pneumatic tuners of torsional oscillations in our understanding.

3. CONDITIONS REQUIRED FROM PNEUMATIC TUNERS OF TORSIONAL OSCILLATION FOR THEIR APPLICATION IN MECHANICAL SYSTEMS

Pneumatic tuners must in any TOMS meet the following requirements:
— Compensation of axial, radial and angular misalignments caused by manufacturing irregularities.

By the load torque transfer the compensation of axial, radial and angular misalignments and also the angular twist of driven to driving part of pneumatic tuner, is ensured by its flexible compression space).
— Ensuring the stable dynamic properties and stable load torque transfer during lifetime of mechanical system.

By twisting the pneumatic tuner the compression of gaseous medium proportional to load is achieved, thus implementing flexible load torque transfer in TOMS. Stable flexible transfer is ensured by the use of gaseous medium (in this case air) as flexible material in the tuner, which has a dominant influence on pneumatic tuner basic characteristics, and throughout its lifetime it is not subject to aging or fatigue (Krejčíř, 1986). Consequently, the pneumatic tuner does not lose its initial characteristics, indicating its stability for the lifetime of TOMS. Pneumatic tuners of torsional oscillations have not one, but a range of load characteristics and also the range of characteristic properties within the range of gaseous medium pressure p in the compression space. Characteristic properties of these tuners are affected by change of gaseous medium pressure p – specifically by tangential, differential and axial tuners – and also by constant twist angle φ_k selection with corresponding gaseous medium pressure p change – specifically by pneumatic tuner of torsional oscillation with auto-regulation).
— Ability of appropriate tuning of torsional oscillating mechanical systems, thus adapting the dynamic properties to the dynamic properties of the system.

Based on change of gaseous medium pressure p in the compression space of pneumatic tuner we are changing, i.e. tuning the torsional stiffness k, which has a decisive influence

on the natural frequency of the system Ω_O, where I_{red} is the reduced mass moment of inertia of the system:

$$\Omega_O = \sqrt{k/I_{red}}. \tag{1}$$

Based on above it follows the principle of appropriate tuning of TOMS by pneumatic tuners of torsional oscillation, which essential nature is to adapt the natural angular frequency of the system Ω_O to the exciting angular frequency ω during operation of the given system so, that in the operating range of the system resonance ($\Omega_O = \omega$) and dangerous torsional vibration does not occur).

3.1. Tangential pneumatic tuners of torsional oscillation

Tangential pneumatic tuners of torsional oscillation (Figs. 2 – 7) consist of driving (1) and driven part (2), between them is located the compression space. The compression space is formed by pneumatic-flexible elements tangentially spaced around the circumference (3). Pneumatic-flexible element is characterized by the rubber-cord single or double bellows filled with gaseous medium. When transferring the load torque there are two pneumatic-flexible elements simultaneously compressed and two expanded, ensuring design of two-way coupling (Figs. 2, 4, 5 and 7). If the compression space is formed by three pneumatic-flexible elements (3), a design of one-way pneumatic coupling is created (Figs. 2 and 5). Through valve (4) the filling of compression space with gaseous medium is realized. The design of pneumatic coupling allows the interconnection of individual pneumatic-flexible elements with changeable throttle nozzles (5) and hoses (6). This created three basic alternatives of interconnection (A, B, C) of pneumatic coupling:

— pneumatic tuner of torsional oscillation, without interconnection of pneumatic flexible elements, with type designation: 4–1/XXX–T–A (Fig. 2) (where the meaning of labeling is following: 4 – number of elements, 1 – single bellows pneumatic-flexible elements with outer diameter – XXX mm, T – with tangential distribution, and A – without interconnection), and 3–1/XXX–T–A (Fig. 3),
— pneumatic tuner of torsional oscillation with mutual interconnection of pneumatic-flexible elements, type designation: 4–1/XXX–T–B (Fig.4),
— pneumatic tuner of torsional oscillation with full mutual interconnection of pneumatic-flexible elements, type designation: 4–1/XXX–T–C (Fig. 5) and 3–1/XXX–T– C (Fig. 6).
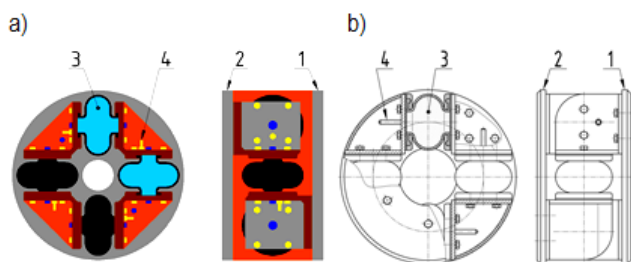

Fig. 2. Tangential pneumatic tuner without pneumatic-flexible elements interconnection: a) graphic representation, b) design representation
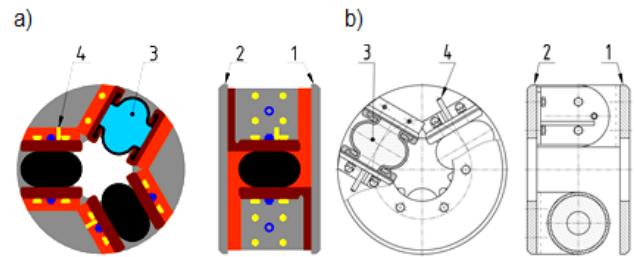

Fig. 3. Tangential pneumatic tuner without pneumatic-flexible elements interconnection: a) graphic representation, b) design representation
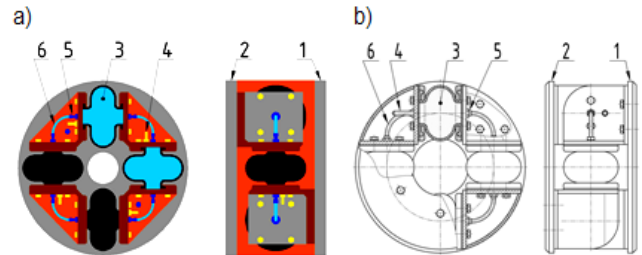

Fig. 4. Tangential pneumatic tuner with mutual interconnection of pneumatic-flexible elements: a) graphic representation, b) design representation
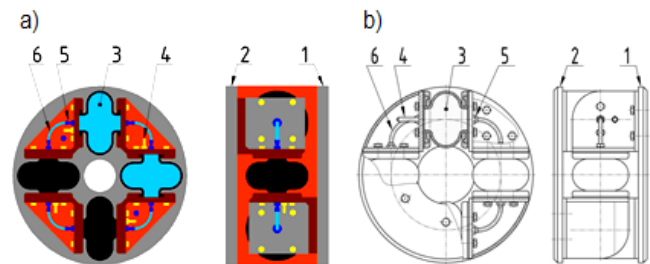

Fig. 5. Tangential pneumatic tuner with full mutual interconnection of pneumatic-flexible elements: a) graphic representation, b) design representation
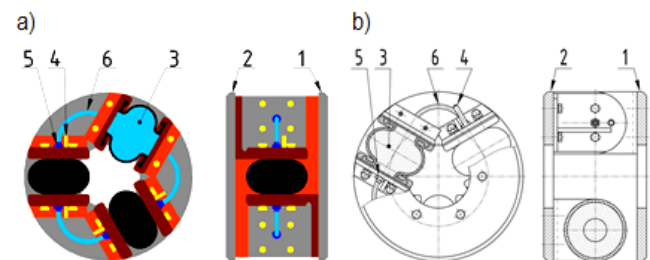

Fig. 6. Tangential pneumatic tuner with full mutual interconnection of pneumatic-flexible elements: a) graphic representation, b) design representation
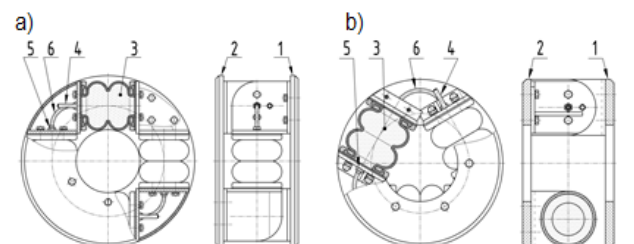

Fig. 7. Tangential pneumatic tuner with full mutual interconnection of pneumatic elements: a) type 4–2/XXX–T–C, b) type 3–2/XXX–T–C

In Fig. 7 pneumatic tuners of torsional oscillation with full mutual interconnection of double-bellows pneumatic-flexible elements type 4–2/XXX–T–C and type 3–2/XXX–T–C are presented.

3.2. Differential pneumatic tuners of torsional oscillation

Differential pneumatic tuners of torsional oscillation type 3–1/XXX–D–C (3 – three, 1 – single-bellows pneumatic flexible elements with outer diameter – XXX mm, with differential elements – D with interconnection – C) (Fig. 8 a, b) or 3–2/XXX–D–C (3 – three, 2 – double-bellows pneumatic flexible elements with outer diameter – XXX mm, with differential elements – D a with interconnection – C) (Fig. 9 a, b) consists of the driving part (1) and the driven part (2), between them is a compression space filled with a gaseous medium (in our case air). Compression space consists of three circumferentially spaced and interconnected differential elements. Each differential element consists of compressed (3) and expanded pneumatic-flexible element (4). Interconnection of differential elements is provided by interconnecting hose (5). Through the valve (6), the filling of compression space of coupling, thereby changing the gaseous media pressure is ensured.
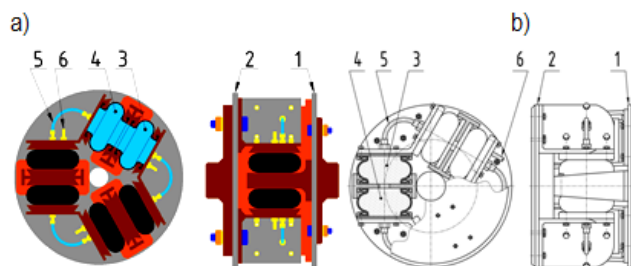

Fig. 8. Differential pneumatic tuner with full mutual interconnection of pneumatic-flexible elements type 3–1/XXX –D–C: a) graphic representation, b) design representation
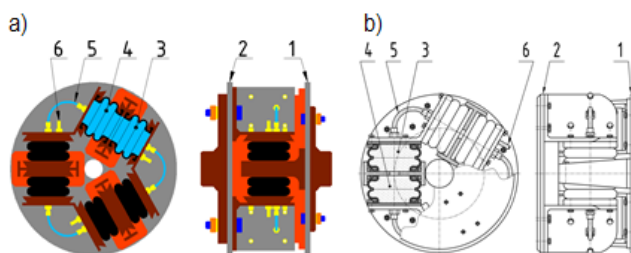

Fig. 9. Differential pneumatic tuner with full mutual interconnection of pneumatic-flexible elements type 3–2/XXX –D–C: a) graphic representation, b) design representation

3.3. Pneumatic tuners of torsional oscillation with autoregulation

Differential pneumatic tuners of torsional oscillation with auto-regulation (Fig. 10), which basic principle results from patent claims of granted patents (Homišin, 1995; 1996), have a common design basis. The main difference consists in regulator (6) which enables to keep constant angle of twist φ_k. The basic principle of the PToTO is the self-regulation ability of the angular twisting, caused due to actual change of loading torque, into the given

constant angular value φ_k. This ensures the self-regulation of the gaseous medium pressure p in the compression space of tuner, thus adapting it to the current value of the load torque. This self-regulation of gaseous medium pressure in the compression space in the tuner has an immediate influence onto the characteristic of pneumatic tuner (Figs. 14 and 15) and, of course, onto the torsional stiffness k (Figs. 11 a, b), in this way it can be changed the natural frequency of the system Ω_O.
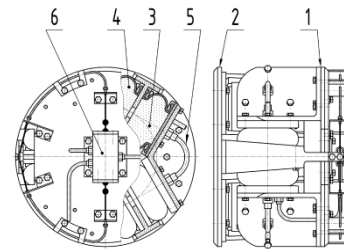

Fig. 10. Pneumatic tuner of torsional oscillation with autoregulation
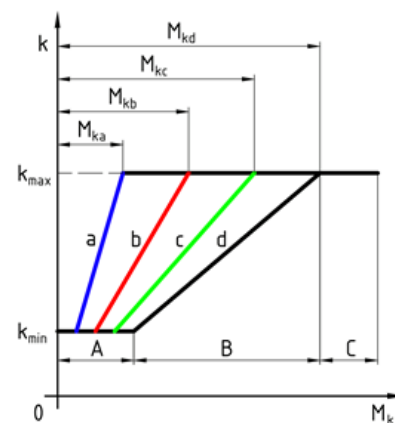

Fig. 11. Courses of torsional stiffness k of pneumatic tuner of torsional oscillation with autoregulation depending on load torque M_k
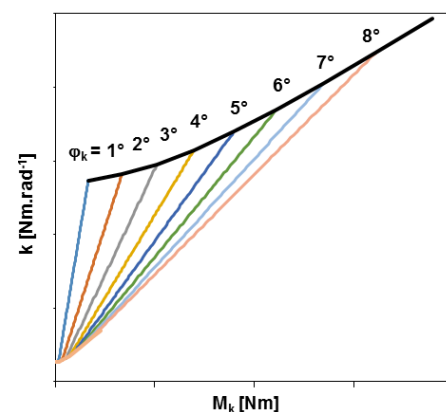

Fig. 12. Courses of torsional stiffness k of pneumatic tuner of torsional oscillation with autoregulation, type 3–1/XXX –D–C depending, on load torque M_k

In Fig. 11 and 12 is schematically presented a behaviour of torsional stiffness k of a PToTO in dependence on loading torque M_k. To each of the calculated constant angles of twist φ_{ka}, φ_{kb}, φ_{kc} and φ_{kd} belongs one behaviour of torsional stiffness a, b, c, d. The above-mentioned behaviours are limited with minimum and maximum values of torsional stiffness k_{min} and k_{max} according to the pressures of gaseous medium from interval

pmin and pmax in compression space of the PToTO. There are also presented behaviours illustrated by a fractional line, which consists of three areas: pre-regulation – A, regulation – B and over-regulation – C area. From this illustration it is evident that change of φ_{ki} influences interval of pre-regulation and regulation area, but it influences mainly the value of pneumatic tuner torsional stiffness during operational regime of the system. There are also influenced values of loading torque M_{ka}, M_{kb}, M_{kc} and M_{kd}, with regard to the maximum value k_{max} of torsional stiffness. The pneumatic tuner with an increasing value of constant angle of twist, during a certain loading torque, has a declining torsional stiffness. In the case of the PToTO with the maximum angle of twist value φ_{kmax}, from the relatively hard pneumatic coupling (behaviour a) becomes a high flexible pneumatic coupling (behaviour d), which is able to operate with considerably higher value of loading torque M_k at maximum value of torsional stiffness.

3.4. Axial pneumatic tuners of torsional oscillation

The essence of axial pneumatic tuners design is the fact that between the drive hub (1) and driven hub (3) is located a floating body (2) solidly coupled with compression space of tuner formed by an elastic hollow body (4) and filled by gaseous medium (Fig. 13) (Homišin, 1986).
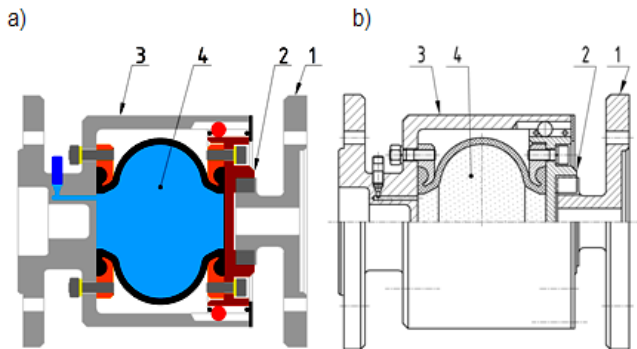

Fig. 13. Axial pneumatic tuner of torsional oscillation:
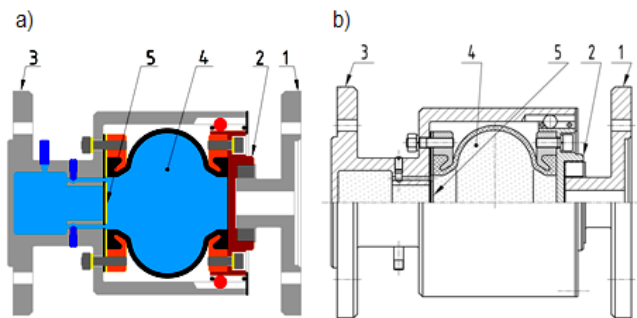a) graphic representation, b) design representation

Fig. 14. Axial pneumatic tuner of torsional oscillation with damping:
a) graphic representation, b) design representation

In Fig. 14 an axial tuner of torsional oscillation with damping is displayed (Homišin, 1986). From the nature of design of the pneumatic tuner follows that between the driving hub (1) and driven hub (3) is formed a compression space. Compression space filled with gaseous medium is divided by a membrane with throttle openings (5) divided into deformable and stationary part.

Deformable part of compression space if formed by a rubber element (4) membrane (5) separated from stationary part of compression space formed by chamber in part (3).

If the compression space of pneumatic tuner (Figs. 13 and 14) is filled by gaseous media with initial pressure p_1, it holds the floating body (2) in basic position, as we can see on the figure. By increasing of load torque in direction of thread teeth helix pitch of meshing parts (1) and (2) the axial shift of floating body (2) occurs, creating a compression of the gaseous medium in the coupling compression space. In the case of oscillating load torque transmission pulsation of carrier fluid occurs in the tuner compression space. Consequently, in proportion to the vibration torque the gaseous medium flows via throttle openings in membrane (5). The flow of gaseous medium is accompanied by throttling at a flow, which is characterized by throttling work in proportion to damping performance that is constant for pneumatic flexible shaft couplings with damping throughout its lifetime.

4. PRESENTATION OF BASIC CHARACTERISTICS OF PNEUMATIC TUNERS OF TORSIONAL OSCILLATION

Within the realized experiments, static and dynamic measurements of pneumatic tuners of torsional oscillation were performed.

Fig. 15. Characteristics of pneumatic tuners of torsional oscillations in the pressure range p = 100 ÷700kPa type 4–1/XXX–T–C, eventually 4–2/XXX–T–C or 3–1/XXX–D–C, eventually 3–2/XXX–D–C

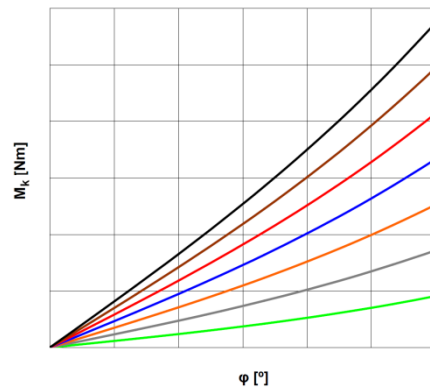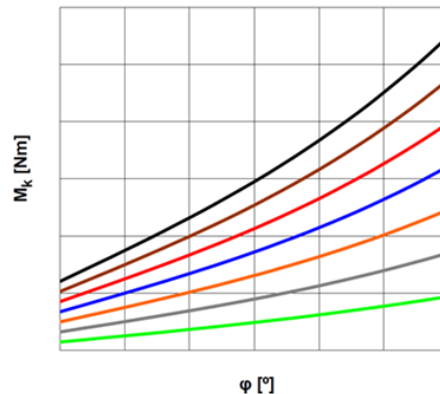**Fig. 16.** Characteristics of pneumatic tuners of torsional oscillations in the pressure range p = 100 ÷700kPa type 3–1/XXX–T–C, eventually 3–2/XXX–T–C

To illustrate the basic characteristics of pneumatic tuners of torsional oscillation only some of the measurement results are mentioned.

Obtained results of static and dynamic measurements showed that changing the pressure of the gaseous medium, pneumatic tuner is capable of working with always a different characteristic (Figs. 15 and 16), thus it is always able to work with other characteristic properties (torsional stiffness and damping coefficient).

Based on Figs. 15 and 16 it is possible to say that the characteristics of the pneumatic tuners are slightly nonlinear. Their course can be expressed by the equation (2) for Fig. 15 and equation (3) for Fig. 16:

$$M_S = a_1\varphi + a_3\varphi^3, \tag{2}$$
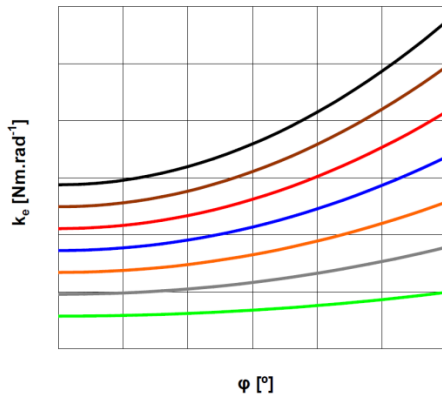
$$M_S = a_0 + a_1\varphi + a_3\varphi^3, \tag{3}$$

Fig. 17. Courses of equivalent torsional stiffness k_e in pressure range $p = 100 \div 700$kPa depending on twist angle φ of pneumatic tuner for the presented types of tuners
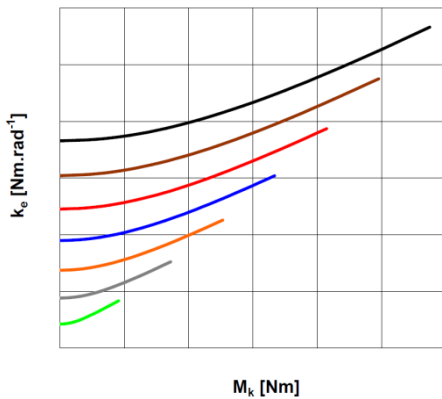

Fig. 18. Courses of equivalent torsional stiffness k_e in pressure range $p = 100 \div 700$kPa depending of trasmitted load torque M_k of pneumatic tuner for the presented types of tuners

From the characteristics of the air tuners we determine the courses of equivalent torsional stiffness of tuners k_e with equivalent linearization method, according to (4) shown in Fig. 17:

$$k_e = a_1 + \frac{3}{4}a_3\varphi^2. \tag{4}$$

Fig. 18 represents the range of equivalent torsional stiffness k_e depending on the transmitted load torque M_k of pneumatic tuners and also it gives us information on whether the tuner is suitable for work in a particular mechanical system.

By changing the pressure of the gaseous medium in the

pneumatic tuners we largely influence on the size of their nonlinearity $\varepsilon = a_3/a_0$. Based on calculation it can be concluded that with the increase of pressure 100 kPa to 700 kPa nonlinearity coefficient decreases within the range $\varepsilon = 15 \div 1,2$ (Fig. 19). The above results lead to the conclusion that in the range of the pressure of the gaseous medium p = 200 ÷ 700 kPa pneumatic tuner can be characterized as linear (That claim is documented among research report (Pešík et al., 1997; Zoul, 1982), in which the authors state that in the case of $\varepsilon < 10$ flexible coupling is considered linear).
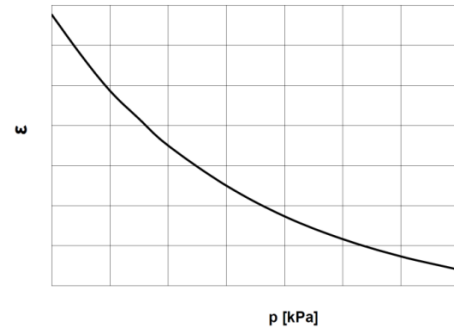

Fig. 19. Nonlinearity coefficient ε courses depending on gaseous medium pressure p in pneumatic tuners
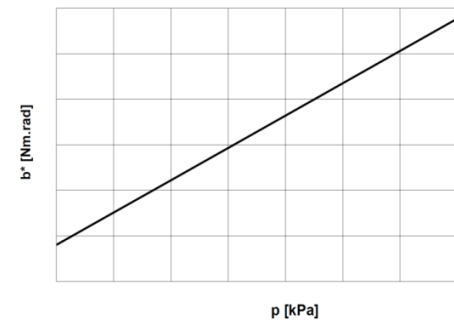

Fig. 20. Course of damping coefficient b^* depending on gaseous medium pressure p in pneumatic tuners

Further processing of measured values records determined equivalent damping coefficient b_e of pneumatic tuners by individual pressures (with determining of equivalent coefficient of damping values be and damping coefficient b^* values based on dynamic measurement by free oscillations the author deals in his candidate dissertation thesis (Homišin, 1989).). The results of our measurements confirmed the fact that the value of damping coefficient pneumatic tuners depends less likely on the preload, amplitude, and temperature, but to a greater extent on the frequency of oscillation ω. Taking this into account impact of the frequency on damping coefficient can be expressed by the relationship (4), while the coefficient of damping b^* (Fig. 20) is for a given preload amplitude and temperature approximately constant, i.e.:

$$b_e = b^*/\omega \tag{5}$$

The main and essential part of the presented pneumatic tuners is their compression chamber, which is formed by compressed and expanded pneumatic-flexible elements (rubber-cord bellows), filled with gaseous medium. In this case, the characteristics of the pneumatic tuners will depend both on the impact of the rubber cord bellows and also the influence of gaseous medium – as its filling.

From the above problem, the question arises, which has a dominant influence on the fundamental characteristics pneumatic tuners - gaseous medium or a rubber-cord container?

In examining the magnitude of two components on the change of the characteristics of the pneumatic tuners it is considered in the article, that the increase in magnitude of the gas medium is in the range of Q_V = 66.22% ÷ 89.83% (course – a), while the declining trend influence of rubber cord container has a range Q_G = 33.78% ÷ 10.17% (course – b) depending on gaseous medium pressure p in pneumatic tuner (Fig. 21).
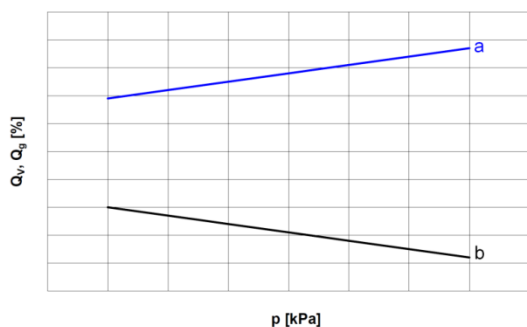

Fig. 21. Influence of gaseous medium Q_V and rubber-cord container Q_G depending on gaseous medium pressure p

On the basis of these values it can be stated that the effect of the gaseous medium at the beginning, i.e. by p = 100 kPa, is compared to the rubber-cord almost double, while on the end i.e. p = 700 kPa shall take up to nine times the value.

From these results we can conclude that on the change of the basic characteristics of pneumatic tuners has a dominant influence definitely the gaseous medium.

5. CONCLUSIONS

Taking into account the above considerations in order to tuning respectively continuous tuning of TOMS and with the intention of restricting dangerous torsional oscillations, we propose to use pneumatic tuners of torsional oscillations developed by us. These pneumatic tuners have not one, but by a range of characteristics and also the range of the characteristics within the range of the pressure of the gaseous medium in the compression space. Characteristics of the tuners are influenced both by changing the pressure of the gaseous medium – specifically in tangential, differential and axial pneumatic tuners – and secondly, the couplings constant angle of twist while changing the pressure of the gaseous medium in them – namely in pneumatic tuners with autoregulation.

Based on the results of experimental verification, it was found that by changing the pressure of the gaseous medium in the compression space of the pneumatic tuner changes, i.e. tunes the dynamic torsional stiffness, which has a decisive influence on the natural frequency of the system. The essence of principle of tuning TOMS by pneumatic tuners is to adapt natural angular frequency of the mechanical system to the angular frequency of the excitation that in the range of the operation mode of the system to the resonance condition, and subsequently dangerous torsional vibration is avoided.

Pressure changes of the gaseous medium in the compression space of the pneumatic tuner can be done beyond or during oper-

ation of mechanical systems.

This resulted in two ways of tuning torsional oscillating mechanical systems suggested by us:
— Tuning of torsional oscillating mechanical systems out of operation,
— Tuning of torsional oscillating mechanical systems during operation in steady state.

REFERENCES

1. **Ankarali A., Mecitoğlu Z., Diken H.** (2012), Response spectrum of a coupled flexible shaft-flexible beam system for cycloidal input motion, *Mechanism and Machine Theory*, 47, 89–102.
2. **Baworski A., Garbala K., Czech P., Witaszek K.** (2015), Estimation of the Ability to Use a Mass of Air from a Moving Vehicle in Wind Turbine Propulsion, *Scientific Journal of Silesian University of Technology, Series Transport,* 88, 5-17.
3. **Binglin L., Huajiang O., Wanyou L., Zhijun S. , Gang W.** (2016), An indirect torsional vibration receptance measurement method for shaft structures, *Journal of Sound and Vibration*, 372, 11–30.
4. **Bingzhao G., Hong C., Haiyan Z., and Kazushi S.** (2010), A Reduced-Order Nonlinear Clutch Pressure Observer for Automatic Transmission, *IEEE Transactions on Control Systems Technology*. 18(2), 446 – 453.
5. **Böhmer J.** (1983), Use of Vulkan Flexible Couplings with linear and progressive torsional load characteristic, *MTZ*, 44/5 (in German),
6. **Bolek A., Krejčí V.** (1967), *Shaft Couplings*. Praha, SNTL (in Czech).
7. **Bulut G.** (2014) Dynamic stability analysis of torsional vibrations of a shaft system connected by a Hookeʹs joint through a continuous system model, *Journal of Sound and Vibration*, 333(16), 3691–3701.
8. **Curà F., Mura A.** (2013), Experimental procedure for the evaluation of tooth stiffness in spline coupling including angular misalignment, *Mechanical Systems and Signal Processing*, 40, 545–555.
9. **Czech P.** (2012), Diagnosis of industrial gearboxes condition by vibration and time-frequency, scale-frequency, frequency-frequency analysis, *Metalurgija,* 51(4), 521–524
10. **Czech P.** (2013), Intelligent approach to valve clearance diagnostic in cars, *Activities of Transport Telematics,* 395, 384–391.
11. **Czech P., Szyma B., Juzek M., Kałuża R.** (2016), Braking process of sports motorbike, *Acta Mechanica Slovaca,* 20(2), 22–31.
12. **El-Sayed A. T., Bauomy H. S.** (2015), Passive and active controlers for suppressing the torsional vibration of multiple-degree-of-freedom system, *Journal of Vibration and Control*, 21(13), 2616–2632.
13. **Folęga P., Wojnar G., Czech P.** (2014), Influence of housing ribbing modification on frequencies and shapes of vibrations, *Scientific Journal of Silesian University of Technology. Series Transport,* 82, 81-86 (in Polish).
14. **Gao W., Hao Z.** (2010), Active control and simulation test study on torsional vibration of large turbo-generator rotor shaft, *Mechanism and Machine Theory*, 45, 1326 – 1336.
15. **Genta G., Festini A., Delepine X.** (2008), From Oil to magnetic fields: active and passive vibration control, *Acta Mechanica et Automatica,* 2(2), 11-20.
16. **Grega R., Homišin J., Puškár M., Kuľka J., Petróci J., Konečný B., Kršák B.** (2015), The chances for reduction of vibrations in mechanical system with low-emission ships combustion engines, *International Journal of Maritime Engineering*, 157(A4), 235-240.
17. **Homišin J.** (1986a), *Pneumatic flexible shaft coupling with damping*, Patent No. 252034, (in Slovak).
18. **Homišin J.** (1986b), *Pneumatic flexible shaft coupling*, Patent No. 254180, (in Slovak).
19. **Homišin J.** (1995a), *Pneumatic Flexible shaft coupling with autoregulation ability*, Patent No. 278025, (in Slovak).

20. **Homišin J.** (1996a), Contribution to a static optimization of torsion-aly oscillating mechanical systems, *The shock and vibration digest*, USA, 28/6, 86.
21. **Homišin J.** (1996b), *Pneumatic coupling with auxiliary controller of constant twist angle*, Patent No. 278272. (in Slovak).
22. **Homišin J.** (2002a), *Axial pneumatic flexible shaft coupling*, IPO SK Banská Bystrica, Patent No 275867, (in Slovak).
23. **Homišin J.** (2002b), *New types of flexible shaft couplings, development – research – application*, Vienala, Košice.
24. **Homišin J.** (2008), *Tuning methods of torsional oscillating mechanical systems by pneumatic couplings*, ATH, Bielsko-Biała, (In Polish).
25. **Homišin J.** (2016), *Pneumatic flexible axial shaft coupling*, IPO SK Banská Bystrica, Patent No 288340, (in Slovak).
26. **Homišin, J.** (1995b), *Shafft coupling with pneumatic-flexible units*, IPO SK Banská Bystrica, Patent No 278024, (in Slovak).
27. **Homišin, J.** (1998), *Pneumatic shaft coupling with flexible-damping units*, IPO SK Banská Bystrica, Patent No 278750 (in Slovak).
28. **James D., Van de Ven , Cusack J.** (2014). Synthesis and baseline testing of a digital pulse-width-modulated clutch, *Mechanism and Machine Theory*, 78, 81–91.
29. **Konieczny L. et al.** (2015), Determination of the effect of tire stiffness on wheel accelerations by the forced vibration test method, *Journal of Vibroengineering,* 17(8), 4469-4477.
30. **Krejčíř O.** (1986), *Pneumatic vibroisolation – dissertation thesis*, Liberec (in Czech).
31. **Lacko P.** (1971), Flexible shaft coupling as absorber of torsional vibrations, *Strojírenství*, 9, 71-74 (in Slovak).
32. **Łazarz B., Wojnar G., Madej H., Czech P.** (2009), Evaluation of gear power losses from experimental test data and analytical methods, *Mechanika*, 80(6), 56-63.
33. **Łazarz B., Wojnar G., Czech P.** (2011), Early fault detection of toothed gear in exploitation conditions, *Maintenance and Reliability*, 49(1), 68-77.
34. **Lunke M., Beeftink G. B.** (1983), Use of highly flexible couplings in energy-saving marine propulsion systems, *Schiff und Hafen*, 4/35, (in German).
35. **Madej, H., Czech, P.** (2009), Diagnostics of clearance in the piston-cylinder assembly using Hoelder coefficient, *Diagnostyka*, 1(49), 73-78.
36. **Madej, H., Czech, P.** (2009), Industrial gearboxes diagnosis by used higher order spectrum, *Scientific Journal of Silesian University of Technology. Series Transport*, 65, 51-56.
37. **Pešík L., Němeček P.** (1997), *Identification of the dynamic system of a machine with an elastic base*, McNU 97, Chicago, USA.
38. **Polyakov V.S.** (1979), *Coupling guid,* Leningrad, Mashinostrojenie, (in Russian).
39. **Rosół M., Sapiński B.** (2014), Autonomous Control System for a Squeeze Mode MR vibration isolator in an automotive engine mount, *Acta Mechanica et Automatica*, 8(3), 121–124.
40. **Singiresu S. R.** (1996), *Engineering optimization theory and practice third edition*, New York, John Wiley & Sons, Inc.
41. **Spruogis B., Turla V.** (2006), A damper of torsional vibrations and an investigation of its efficiency, *Strojniški vestnik - Journal of Mechanical Engineering*, 52(4), 225–236.
42. **Timoshenko, S.** (1960), *Vibration problems in engineering*, Praha*, SNTL* (in Czech).
43. **Wilson W.K.** (1968), *Practical solution of torsional vibration problems, volume 4*, London, Chapman & Hall LTD.
44. **Wojnar G.** (2009), Analysis of usefulness of different vibration signals for toothed gears diagnostics, *Acta Mechanica et Automatica,* 3(2), 111–114 (in Polish).
45. **Yubao S., Jihong W., Dianlong Y. and Xisen W.** (2013), Analysis and enhancement of torsional vibration stopbands in a periodic shaft system, *Journal Of Physics D: Applied Physics*, 46, 7-13.
46. **Zoul V.** (1982), Some aspects of flexible coupling development for sets with diesel engines, *Strojírenství*, 32(6/7), (in Czech)
47. **Zoul V.** (1988), *Rato Highly Flexible Couplings*, ČKD Praha, 20 (in Czech).
48. **Zoul V.** (1989) *The use of flexible shaft couplings with low torsional stiffness for reducing dynamic torsional loads*, IS ČKD Praha, 24-25, (in Czech).

ABSTRACTS

Maciej Słowik, Tomasz Mrozek

Experimental Analysis of Navigational Precision For Dedicated GNSS Receivers

In the paper experimental investigations related with analysis of navigational precision of three chosen GNSS receivers are shown. Used receivers allow for measurement of navigational signals in following modes of operations: receiving signals from single-frequency GPS system, dual-frequency GPS/GLONASS system, and receiving signals from GPS constellation with use of differential measurements. In the last mode the base station and mobile receiver were configured for transmitting/receiving differential corrections by pair of industry-grade radio modems. The most important features and configuration of navigational receivers for conducted experiment are presented. Afterward the features of computer program designed especially for simultaneous acquisition, analysis of quality parameters and archiving of navigational signals are shown. The results of conducted investigations are also shown. For each of the receivers quantity and quality parameters such as maximum and minimum numbers of visible satellites and DOP (dilution of precision) parameters achieved during the experiment are given.

Agnieszka Mackiewicz, Grzegorz Sławiński, Tadeusz Niezgoda, Romuald Będziński

Numerical Analysis of the Risk of Neck Injuries Caused by IED Explosion under the Vehicle in Military Environments

As a result of an explosion under a military vehicle, the risk of threat to life and health of the crew increases. Examination of this event in terms of the security of soldiers comes down to a complex analysis of the mutual interaction of the body of a soldier, seating and structural elements of the vehicle. As a result, shock wave impacts can cause tremor resulting from the construction of the vehicle and acceleration of the passenger's body. This study attempts to analyze the impact of an explosion of an improvised explosive device (IED) under the military vehicle with the risk of cervical spine injuries of soldiers. The analysis was carried out using numerical methods in the LS-DYNA program and was carried out taking into account the variable displacement values and acceleration recorded during the\ explosion. The study used a model of the body of a soldier in the form of a Hybrid III 50th Male Dummy.

Aleksander Karolczuk

Ratcheting Simulation in a Titanium-Steel Bimetallic Plate Based on the Chaboche Hardening Model

The paper presents the results of fatigue loading simulation applied to bimetallic model using the Chaboche kinematic hardening rule. Three cases of simulations were performed: (i) without residual stresses; (ii) considering residual stresses and (iii) considering asymmetrical geometry of bimetal, i.e. cross area reducing under tension period of loading. Experimental results exhibit the ratcheting phenomenon in titanium-steel bimetallic specimens. The observed ratcheting phenomenon could be explained by the third case of simulation which is supported by detection of microcracks in the vicinity of welded area.

Emil Spišák, Janka Majerníková, Emília Duľová, Ľuboš Kaščák

Analysis of Plastic Deformation of Double Reduced Sheets

This paper discusses the causes and the effects of plastic deformation of double reduced sheets under uniaxial and biaxial loading. It focuses on the specific inhomogeneity and localization of plastic deformation, which is analysed in detail. The uniaxial and the hydraulic biaxial tensile tests were used for material testing and the results were compared and evaluated. The final part of the paper deals with the microstructure of material deformations.

Jan Jaworski, Tomasz Trzepieciński

Surface Layer Properties of Low-Alloy High-Speed Steel After Grinding

Investigations of the surface layer characteristics of selected kinds of low-alloy high-speed steel after grinding were carried out. They were carried out on the flat-surface grinder with a 95A24K grinding wheel without cooling. The influence of grinding parameters was defined especially for: the quantity of secondary austenite, surface roughness, microhardness and grinding efficiency with a large range of grinding parameters: grinding depth 0.005–0.035 mm, lengthwise feed 2–6 m/min, without a cross-feed on the whole width of the sample. It was found that improvement of grinding properties of low-alloy high-speed steels is possible by efficient selection of their chemical composition. The value of the grinding efficiency is conditioned by grinding forces, whose value has an impact on the grinding temperature. To ensure high quality of the tool surface layer (i.e. a smaller amount of secondary austenite, lack of wheel burn and micro-cracks) in the case of sharpening of tools made of low-alloy high-speed steel, the grinding temperature should be as low as possible.

Maria Kotełko, Artur Mołdawa

Impact Behaviour of Spot-Welded Thin-Walled Frusta

In the paper the dynamic response of thin-walled, spot-welded prismatic frusta subjected to axial impact load is investigated. The parametric study into the influence of several parameters on the energy absorption capability, expressed by some crashworthiness indicators is performed, using Finite Element simulations. FE model is validated by experimental results of quasi-static and dynamic (impact) tests. Results of initial study concerning influence of spot welds are presented. Some conclusions are derived from the parametric study into the influence of frustum angle and wall thickness upon the energy absorption capability.

Svyatoslav Litynskyy, Yuriy Muzychuk, Anatoliy Muzychuk

On the Numerical Solution of the Initial-Boundary Value Problem with Neumann Condition for the Wave Equation by the Use of the Laguerre Transform and Boundary Elements Method

The aim of this paper is the numerical analysis of the one of main part of car engine – piston sleeve. The first example is for piston sleeve made of metal matrix composite (MMC) A356R. The second improved material structure is layered. Both of them are comparison to the classical structure of piston sleeve made of Cr-Ni stainless steel. The layered material structure contains the anti-abrasion layer at the inner surface of piston sleeve, where the contact and friction is highest, FGM (functionally graded material) interface and the layer of virgin material on the outer surface made of A356R. The complex thermo-elastic model with Archard's condition as a wear law is proposed. The piston sleeve is modelling as a thin walled cylindrical axisymmetric shell. The coupled between the formulation of thermo-elasticity of cylindrical axisymmetric shell and the Archard's law with functionally changes of local hardness is proposed.

Andrzej Koszewnik, Krzysztof Wernio

Modelling and Testing of the Piezoelectric Beam as Energy Harvesting System

The paper describes modelling and testing of the piezoelectric beam as energy harvesting system. The cantilever beam with two piezo-elements glued onto its surface is considered in the paper. As result of carried out modal analysis of the beam the natural frequencies and modes shapes are determined. The obtained results in the way mentioned above allow to estimate such location of the piezo-actuator on the beam where the piezo generates maximal values of modal control forces. Experimental investigations carried out in the laboratory allow to verify results of natural frequencies obtained during simulation and also testing of the beam in order to obtain voltage from vibration with help of the piezo-harvester. The obtained values of voltage stored on the capacitor C_0 shown that the best results are achieved for the beam excited to vibration with third natural frequency, but the worst results for the beam oscillating with the first natural frequency.

Janette Brezinová, Anna Guzanová, Dagmar Draganovská, Pavlo O. Maruschak, Mariana Landová

Study of Selected Properties of Thermally Sprayed Coatings Containing WC and WB Hard Particles

The paper presents results of research of the essential characteristics of two kinds of advanced coatings applied by HVOF technology. One studied coating: WB-WC-Co (60-30-10%) contains two types of hard particles (WC and WB), the second coating is eco-friendly alternative to the previously used WC-based coatings, called "green carbides" with the composition WC-FeCrAl (85-15%). In green carbides coating the heavy metals (Co, Ni, NiCr) forming the binding matrix in conventional wear-resistant coatings are replaced by more environmentally friendly matrix based on FeCrAl alloy. On the coatings was carried out: metallographic analysis, measurement of thickness, micro-hardness, adhesion, resistance to thermal cyclic loading and adhesive wear resistance (pin-on-disk test). One thermal cycle consisted of heating the coatings to 600°C, dwell for 10 minutes, and subsequently cooling on the still air. The number of thermal cycles: 10. The base material was stainless steel AISI 316L, pretreatment prior to application of the coating: blasting with white corundum, application device JP-5000.

Wojciech Sikora, Krzysztof Michalczyk, Tomasz Machniewicz

A Study of the Preload Force in Metal-Elastomer Torsion Springs

Neidhart type suspension units composed of metal-elastomer torsion springs can be a good alternative to steel helical springs in applications such as vibration absorbers or vehicle suspension systems. Assembling this type of spring requires initial preload of the elastomeric working elements, which determines their operating properties.The results of experimental tests and numerical simulations concerning the preload of elastomeric working elements in Neidhart type suspension units are presented in the paper. The performed research made it possible to propose a new calculation model for determining the preload force value acting on the elastomeric cylindrical elements applied in this type of suspension unit. The results obtained using the proposed model exhibit good convergence with FEM simulation results within the range of the tested geometrical and material properties.

Daniel Pieniak, Agata Walczak, Agata M. Niewczas

Comparative Study of Wear Resistance of the Composite with Microhybrid Structure and Nanocomposite

The paper presents the results of investigations on the air gages dynamic characteristics in the measurement of the round profiles of motor cylinders. The principle of the measuring device is explained, and the analysis of the air gages dynamics is described. The results of dynamic calibration enabled to eliminate those configurations of air gages that may not meet the requirements of the measurement they were designed for. After the proper air gages were chosen, the entire system underwent the accuracy test and passed it successfully revealing the method accuracy better than 10% compared to the reference measurement.

Slawomir Duda, Damian Gasiorek, Grzegorz Gembalczyk, Slawomir Kciuk, Arkadiusz Mezyk
Mechatronic Device for Locomotor Training

This paper presents a novel mechatronic device to support a gait reeducation process. The conceptual works were done by the interdisciplinary design team. This collaboration allowed to perform a device that would connect the current findings in the fields of biomechanics and mechatronics. In the first part of the article shown a construction of the device which is based on the structure of an overhead travelling crane. The rest of the article contains the issues related to machine control system. In the prototype, the control of drive system is conducted by means of two RT-DAC4/PCI real time cards connected with a signal conditioning interface. Authors present the developed control algorithms and optimization process of the controller settings values. The summary contains a comparison of some numerical simulation results and experimental data from the sensors mounted on the device. The measurement data were obtained during the gait of a healthy person.

Jaroslav Homišin
Charakteristics of Pneumatic Tuners of Torsional Oscillation as a Result of Patent Activity

Mechanical systems with combustion engines, compressors, pumps and fans, can be characterized as torsional oscillating mechanical systems (TOMS). It is therefore necessary to control their dangerous torsional vibrations. It was confirmed that dangerous torsional vibration can be reduced to acceptable level by an appropriate adjustment, respectively by tuning the TOMS. According to several authors, the most appropriate way of system tuning is application of suitable flexible element, which is flexible shaft coupling. It turned out that one of the types of shaft couplings, which are particularly suited to meeting this objective are pneumatic flexible shaft couplings, to act as so-called pneumatic tuners of torsional oscillations. The issue of research and development of pneumatic tuners of torsional oscillations, among other things is, long-term in the focus of the author. The existence of tuners creates the opportunity to develop new ways of tuning torsional oscillating mechanical systems. The author of the scientific article will focus on the characteristics of developed pneumatic tuners of torsional oscillation in terms of their design, construction, function, significance advantages and conditions imposed on pneumatic tuners based on the results of his patent activity. Simultaneously provides information about the characteristic properties of pneumatic tuners of torsional oscillations in the general design.